Title
Optoelectronic Manipulation, Assembly, and Patterning of Nanoparticles

Author
Jamshidi, Arash

Publication Date
2009

Peer reviewed|Thesis/dissertation

Optoelectronic Manipulation, Assembly, and Patterning of Nanoparticles

by

Arash Jamshidi

A dissertation submitted in partial satisfaction of the

requirements for the degree of

Doctor of Philosophy

in

Engineering – Electrical Engineering and Computer Sciences

and the Designated Emphasis

in

Nanoscale Science & Engineering

in the

Graduate Division

of the

University of California, Berkeley

Committee in charge:

Professor Ming C. Wu, Chair
Professor Constance Chang-Hasnain
Professor Liwei Lin

Fall 2009

Optoelectronic Manipulation, Assembly, and Patterning of Nanoparticles

by Arash Jamshidi

Abstract

Optoelectronic Manipulation, Assembly, and Patterning of Nanoparticles

by

Arash Jamshidi

Doctor of Philosophy in Engineering – Electrical Engineering and Computer Sciences and the Designated Emphasis in Nanoscale Science & Engineering

University of California, Berkeley

Professor Ming C. Wu, Chair

The synthesis of nanostructures has advanced in the last decade to a point where a vast range of insulating, semiconducting, and metallic materials are available in a variety of forms and shapes such as wires, tubes, ribbons, sheets, and spheres. These nanostructures display exceptional physical properties that can be used to realize novel devices such as high-speed electronics, efficient photovoltaics and thermoelectrics, sensitive chemical and biological sensors, nano-light sources such as lasers and light-emitting diodes, and high-frequency resonators. However, a persistent challenge has been the development of a general strategy for manipulation and heterogeneous integration of individual nanostructures with arbitrary shapes and compositions. Development of such methods is essential in transforming nano-sciences into successful nano-technologies that can ultimately affect the society. Several techniques such as microcontact printing, microfluidics, Langmuir-Blodgett, mechanical nano-manipulators, optical tweezers, and fixed-electrode dielectrophoresis have been developed to address this challenge. However, these techniques either lack the capability to manipulate single nanostructures or are unable to do so in a dynamic and large-scale fashion.

Optoelectronic tweezers (OET) has emerged as a powerful tool for massively parallel manipulation of polymer-beads and living cells at micron length-scales via *optically-induced* dielectrophoresis. By combining the optical and electrical trapping capabilities, OET is able to manipulate particles with much lower optical intensities than optical tweezers and unlike fixed electrode dielectrophoresis, OET is capable of dynamic manipulation of *single* particles over large areas.

In this dissertation, we will first introduce OET as an optofluidic platform and characterize the various electrokinetic forces that can be generated in the OET device. Next, we will use these forces for manipulation, sorting, assembly, and patterning of various nanostructures such as semiconducting and metallic nanowires, carbon nanotubes, and metallic spherical nanocrystals. Though the initial demonstrations of OET were limited to manipulation of microscale objects,

here, we will explore the capabilities of OET for manipulation of nanoscale particles, establishing it as an important tool for post-synthesis organization and heterogeneous integration of nanostructures.

TABLE OF CONTENTS

LIST OF FIGURES

LIST OF TABLES

ACKNOWLEDGEMENT

I would like to thank my advisor, Professor Ming C. Wu, for his continual support and encouragement during the completion of my dissertation. I have learned from him so much personally and academically during the past few years and I am eternally grateful to him for giving me the opportunity to be part of the integrated photonics laboratory (IPL) team.

I would also like to thank Professor Constance J. Chang-Hasnain, Professor Liwei Lin, and Professor Albert P. Pisano for their kind review of this dissertation and Professor Peidong Yang, Professor Ali Javey, and Professor Luke P. Lee for their helpful collaborations.

I would like to thank my current and former labmates at integrated photonics laboratory for their helpful suggestions and discussions. Especially, I would like to thank Professor Pei-Yu Chiou, Professor Aaron T. Ohta, Hsan-Yin Hsu, Justin K. Valley, Dr. Steven L. Neale, Shao Ning Pei, Professor Kyoungsik Yu, Dr. Ming-Chun Tien, Amit Lakhani, and Tae-Joon Seok for their help and support. I would also like to thank my colleagues Dr. Peter J. Pauzauskie, Dr. P. James Schuck, Dr. Wilbur A. Lam, Professor Jiaxing Huang, Dr. Raül Diaz, and Dr. Erik Garnett for their collaboration and the UC Berkeley microfabrication laboratory (Microlab) staff for their help and support.

Finally, I would like to thank my parents and my brother for their everlasting help, support, and love.

Chapter 1 Introduction

1.1 Methods for Nanoparticle Manipulation and Patterning

The synthesis of nanostructures has advanced in the last decade to a point where a vast range of insulating, semiconducting, and metallic materials [1-5] are available for use in applications such as integrated, heterogeneous optoelectronic devices [6], nanoelectronics [7, 8], biological and chemical sensing [9-11], and thermoelectrics [12]. One approach for organization of materials with nano-scale dimensions is the so-called 'bottom-up' assembly of heterogeneous nano-scale building blocks [13]. Though it is possible to achieve a high level of orientation control [14, 15] through epitaxial growth of semiconductor materials [16], there are enormous challenges to achieving a high level of integration with heterogeneous material systems due to large differences in chemical and thermal stability. One way to circumvent the constraints of thermo-chemical incompatibility is to first synthesize various materials at favorable processing conditions, then employ a strategy for post-synthesis integration. However, a persistent challenge has been the development of a general strategy for the manipulation of individual nanostructures with arbitrary shapes and compositions. Several techniques have been employed over the last decade to address this challenge. These techniques use a variety of forces including optical, electrical, magnetic, mechanical, and fluidic effects to address the nanoparticles. Each of these methods has its own unique capabilities and limitations; here, we will briefly review some of these techniques.

Optical tweezers [17], first proposed by Ashkin in 1970 [18], is a powerful optical manipulation technique that has been used for trapping of cells and polystyrene beads [19], nanowires [20], carbon nanotubes [21], nanoparticles [22, 23], and characterization of bio-molecules [24]. In this method, the optical field of a highly focused laser light is used to trap the particles. In the case of particles with sizes much smaller than the wavelength of the trapping laser (the Rayleigh limit), the particles are treated as electrical dipoles that are interacting with the optical trap's electric field gradient. For particles much larger than the wavelength of the trapping laser, (the Mie limit), the particles change the momentum of the photons by refracting the laser light, therefore experiencing an equal and opposite force. The radiation force resulting

from the bombardment of the particles with photons opposes the trapping of particles in both cases. Therefore, to create a stable trap, the trapping light source needs to be tightly focused, using a lens with high numerical aperture (N.A.), to overcome the radiation pressure. As a result, optical tweezers' trapping capability is limited by the high optical power intensity required to create a stable trap. In addition, the high required N.A. for focusing the laser source limits the effective working area of optical tweezers to about 100 μm × 100 μm using a spatial light modulator, commonly referred to as holographic optical tweezers (HOT) [25].

Fixed-electrode dielectrophoresis (DEP) is another approach that has been widely used to manipulate micro-scale objects and has been employed recently to manipulate various suspended nanostructures [26-29]. In this technique, the interaction of a non-uniform electric field with suspended particles in the solution results in attraction or repulsion of particles from the area of highest electric field intensity gradient. The non-uniform field is typically created using lithographically fabricated electrodes. Therefore, even though fixed-electrode DEP is not limited by the manipulation area, the trapping patterns are fixed. As a result, this method does not allow for real-time and flexible manipulation and transport of trapped particles. Other electrokinetic effects such as electrophoresis [30, 31] and electroosmosis [32] have been used to address various nanoparticles. However, electrophoresis requires the particles to carry charges and doesn't act on uncharged particles and electroosmotic flows have fixed trapping patterns similar to the fixed-electrode DEP. Another electrokinetic method for trapping single molecules is the Anti-Brownian Electrokinetic (ABEL) technique [6] which cancels the Brownian motion of the particle by inducing electrophoretic and electroosmotic drifts. This method can provide extensive information about the particle dynamics but requires the molecules to be fluorescent.

Mechanical nano-manipulators have been used to position and shape one-dimensional nanostructures [6, 33, 34]. Even though integration of nano-manipulators with scanning electron microscopes can yield impressive position control, this technique is incapable of large-scale and parallel manipulation of particles. Moreover, mechanical techniques are inherently invasive and can potentially damage the manipulated nanostructures. This is especially important at the nanoscale since surface defects can greatly modify the nanopaticle properties such as electrical and thermal conductivity.

Magnetic forces have also been used to trap and align nanoparticles [35-37]. However, these methods can only address intrinsically magnetic materials or require tagging of particles with magnetic objects. Microfluidics [38, 39] have been used to control the orientation of a large number of nanostructures using hydrodynamic forces. However, these methods require complicated pump and flow control systems and are incapable of addressing single nanoparticles.

Self-assembly of nanostructures through patterning of organic markers [40] has been used for large-scale patterning of nanoparticles. Microcontact printing techniques have opened up the possibility to coat macroscopic areas with inorganic nanowires or carbon nanotubes [41-45]. Langmuir-Blodgett [46-48] patterning has also been used to align large numbers of nanowires dispersed in a fluid matrix to form highly organized structures. However, all these techniques lack the capability to manipulate and position individual nanostructures. Other powerful techniques such as dip-pen nanolithography [49-54] and nanofabrication [55, 56], have been used to pattern nanostructures. However, these techniques are incapable of creating real-time reconfigurable patterns without the use of complicated instrumentation or processing steps.

1.2 Optoelectronic Tweezers (OET)

Optoelectronic tweezers (OET) [57] is a powerful optical manipulation technique for manipulation, sorting, organization, and patterning of micro- and nanoparticles. Figure 1.1 shows the OET device structure. In this technique, two-dimensional patterns of low-intensity light are projected onto a plane of photoconductive material sandwiched between transparent parallel-plate electrodes. The light excites carriers in the photoconductive layer (hydrogenated amorphous silicon), reducing the local impedance to create an inhomogeneous electric field across the liquid layer. In the presence of the non-uniform electric field, a polarization is induced in particles between the parallel plates. The polarized particles are either attracted to or repelled from the field gradient (according to the DEP principle) produced by the projected light pattern, yielding a powerful optoelectronic method of particle manipulation based on dynamic, light-actuated virtual electrodes.

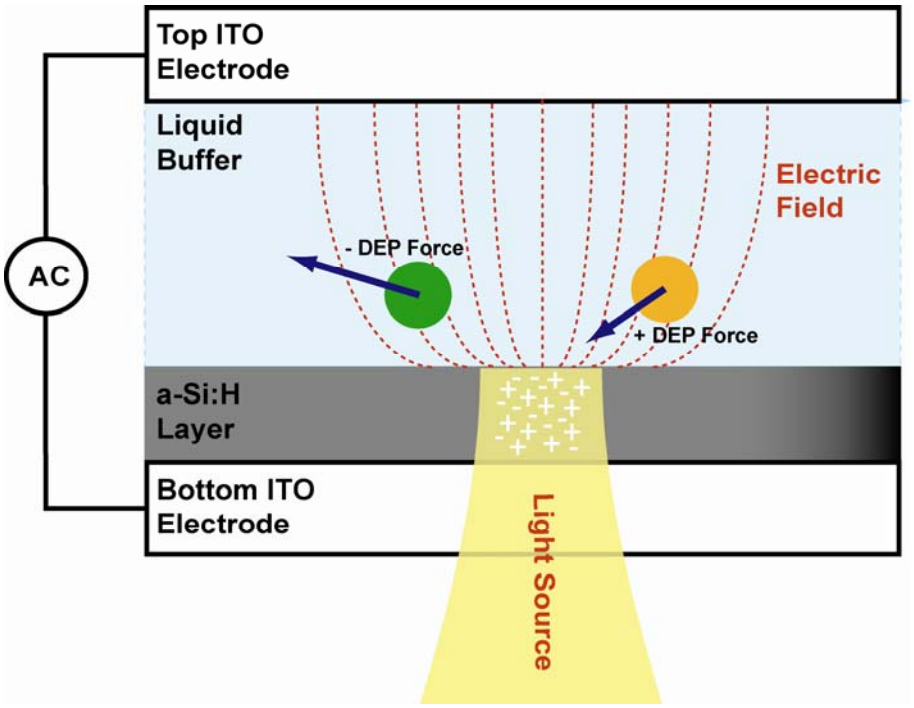

Figure 1.1 Optoelectronic tweezers (OET) device structure. The OET device consists of a top transparent ITO electrode and a bottom ITO electrode. There is a layer of photoconductive material (hydrogenated amorphous silicon) on top of the bottom electrode. An AC voltage is applied between the two electrodes. The liquid medium containing the particles of interest is sandwiched between the top and bottom layers. The interaction of the light source with the photoconductive layer reduces the impedance locally, transferring the voltage to the liquid layer in the area that the light is present. This non-uniform electric field traps the particles by light-induced dielectrophoresis principle.

In the OET technique, the optical power intensity required for trapping the particles is reduced considerably relative to optical tweezers since the optical field is not directly used to trap the particles; rather, the optical field is used to create virtual electrodes in the photoconductive layer. In addition, since the electrodes are defined optically, it is possible to

create real-time flexible trapping patterns using a spatial light modulator. Furthermore, due to the small optical power intensity required for trapping and relaxed optical focusing requirements, a large working area can be achieved. These capabilities of OET have previously been demonstrated through massively parallel manipulation of 15,000 particles over a large area, 1.3 mm×1.0 mm as shown in Figure 1.2 [57].

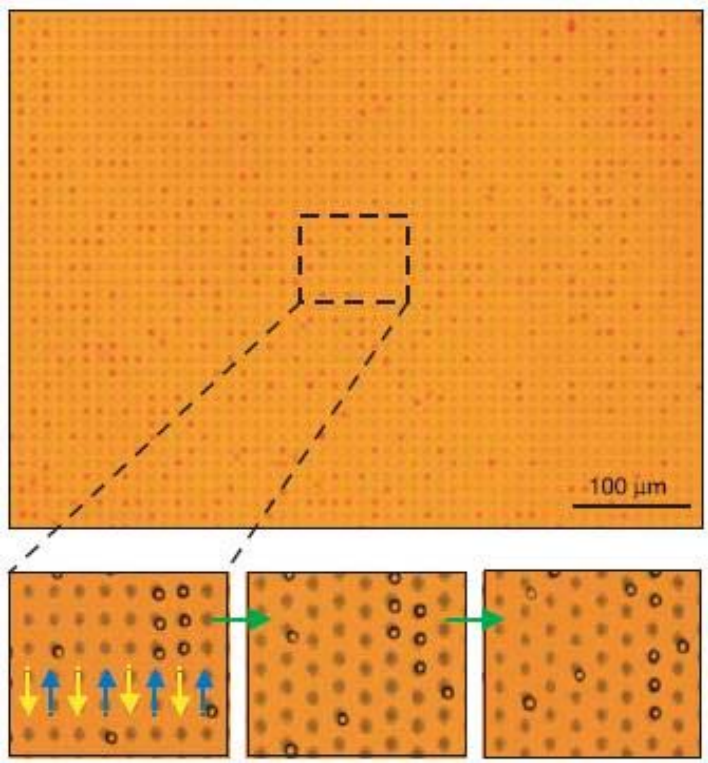

Figure 1.2 Massively parallel manipulation of single 4.5-µm-diameter polystyrene particles over 1.3 mm × 1.0 mm area using 15,000 traps created by a digital micromirror device. The inset shows the transport of particles in the direction depicted by the arrows. [57]

Since the DEP force is dependant on the properties of the particles in relation to the surrounding media, OET is also capable of distinguishing between particles with differing complex permittivities such as dead and live cells [57] and semiconducting and metallic materials [58]. This ability is particularly important in cell separation and sample purification.

Since the first demonstration of optoelectronic tweezers by our research group in 2003, OET has grown to become an important optofluidic manipulation tool and is pursued around the world by various research groups who are innovating new ideas to expand this field. Figure 1.3 shows the ten research groups who are currently active in the optoelectronic tweezers field.

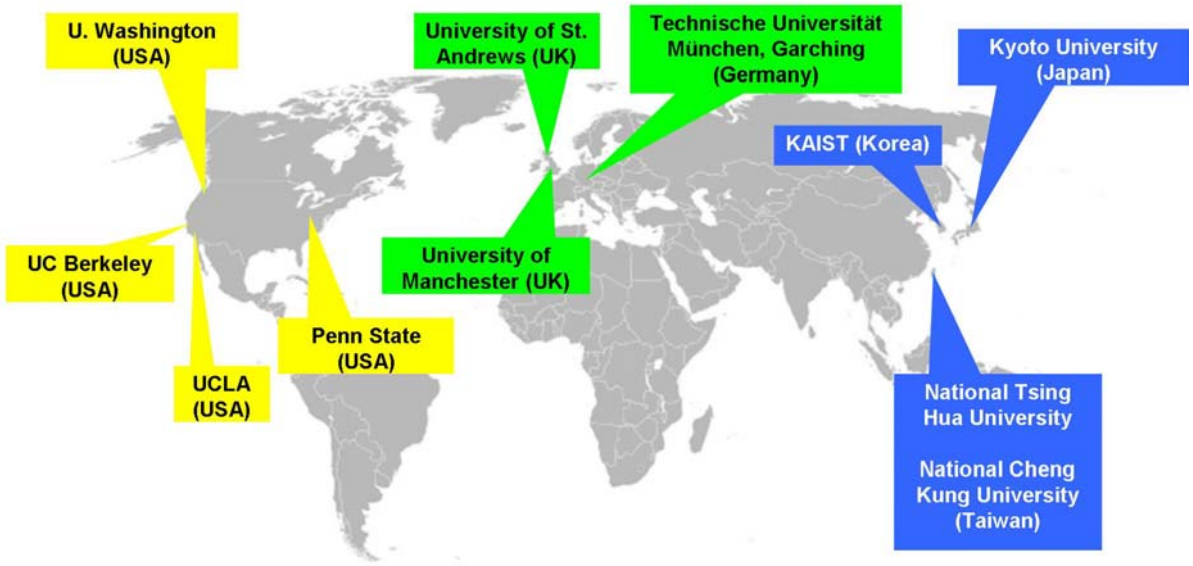

Figure 1.3 Optoelectronic tweezers around the world.

Figure 1.4 shows some of the major milestones achieved by various groups in the development of optoelectronic tweezers. To date, various photoconductive materials such as hydrogenated amorphous silicon [57], silicon phototransistor [59], CdS [60], metallic plasmonic nanoparticles [61, 62], and polymers [63] have been used to realize the optoelectronic tweezers devices. Dynamic actuation of OET has been accomplished with a variety of coherent and incoherent light sources such as scanning lasers [64], digital micromirror devices [57], and LCD flat panel displays [65, 66]. Moreover, various modes of operation such as dielectrophoresis (DEP) [57], light-actuated AC electroosmosis [67], and electrothermal heating [68] have been observed and characterized in the OET optofluidic platform. Manipulation of microparticles such as polystyrene beads [57, 65, 66, 69-72], red blood cells [66, 70], E. *coli* bacteria [64], white blood cells [57, 71], Jurkat cells [71], HeLa cells [71, 73], yeast cells [72], and Neuron cells [74] and nanoparticles such as semiconducting and metallic nanowires [58, 75-77], carbon nanotubes [78], metallic spherical nanoparticles [79], and DNA [80, 81] has been achieved with OET. Other functionalities such as dynamic single cell electroporation [82] and cell lysis [83], optically induced flow cytometry [84], and large-scale, dynamic patterning of nanoparticles [85] have been demonstrated using the OET platform.

In addition to the conventional OET device structure, other OET configurations have also been invented including: phototransistor OET (phOET) which makes use of a phototransistor structure as the photoconductive layer to achieve higher optical gains and manipulate cells in high conductivity cell culture media [59], lateral-field OET (LOET) and planar lateral-field OET (PLOET) [71, 75-77] which are capable of manipulating particles in a lateral fashion through the use of interdigitated photoconductive electrodes, floating electrode OET (FLOET) [86] which can manipulate aqueous droplets in oil, double sided OET [87] which reduces the nonspecific stiction of particles by using amorphous silicon as the top and bottom surfaces, and OET

integrated with electrowetting-on-dielectric [88] devices which enable manipulation of particles within droplets.

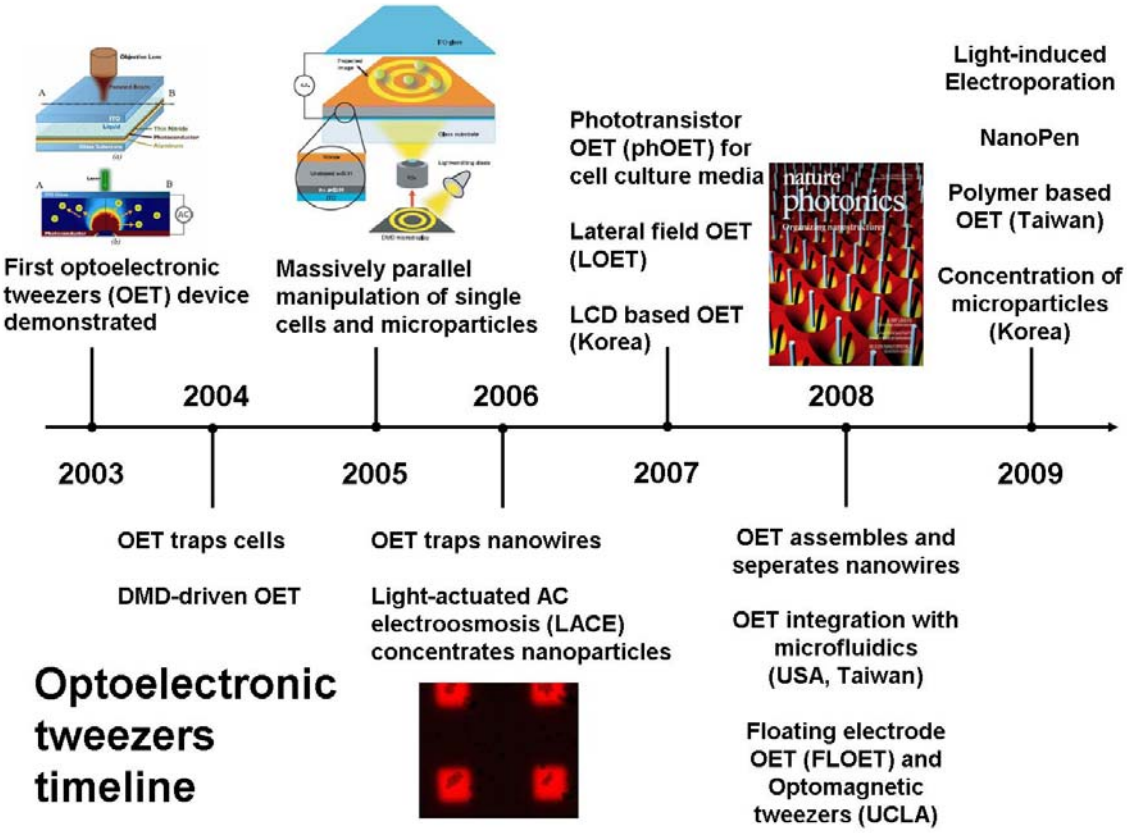

Figure 1.4 Timeline of major developments in optoelectronic tweezer technology.

Chapter 2 Optoelectronic Tweezers

2.1 Introduction

In addition to light-induced dielectrophoresis force which is the main operational principle of OET, there are other operational regimes in the OET device that can be generated by tuning various parameters such as voltage, frequency, and liquid conductivity [89]. These operational regimes create various electrokinetic forces that can be used to address micro- and nanoscale particles. Therefore, a comprehensive understanding of these operational regimes is essential in using OET as an integral part of an optofluidic system. In this chapter we will describe the OET device structure in detail and will explore and characterize the various electrokinetic forces observed in the OET device.

2.2 Optoelectronic Tweezers Device Description

Figure 2.1 shows the structure of the optoelectronic tweezers (OET) device. The OET device consists of a top 300-nm thick transparent indium-tin-oxide (ITO) coated glass electrode and a bottom ITO-coated glass substrate on top of which a 1-2 μm layer of photoconductive material (hydrogenated amorphous silicon, a-Si:H) is deposited. The liquid solution containing the particles of interest is sandwiched between the top and bottom surfaces using a 80-100 μm spacer and an AC voltage (5-20V peak-to-peak voltage at 1-100 kHz frequency) is applied between the top and bottom ITO electrodes. Figure 2.1 inset shows a scanning electron microscopy (SEM) cross-section of the OET device bottom electrode.

Once the OET device is assembled, it is placed under a microscope for observation and actuation. Various microscope observation modes such as bright-field, dark-field, fluorescent or differential interference contrast (DIC) microscopy can be used for particle visualization. Dark-field observation is particularly suitable for observation of nanoscale objects due to the strong light scattering by nanostructures. A charge-coupled device (CCD) camera is used to record the particle manipulation and provide image feedback. Coherent light sources such as low-power laser diodes or incoherent light sources such as light-emitting diodes (LEDs) can be used to actuate the OET device. Dynamic light patterns are generated using spatial light modulators such

as digital micromirror devices (Texas Instruments) or liquid-crystal based spatial light modulators (Hamamatsu). The light patterns are then focused onto the OET device surface either through the same microscope objective used for observation or an additional objective lens on the opposite side.

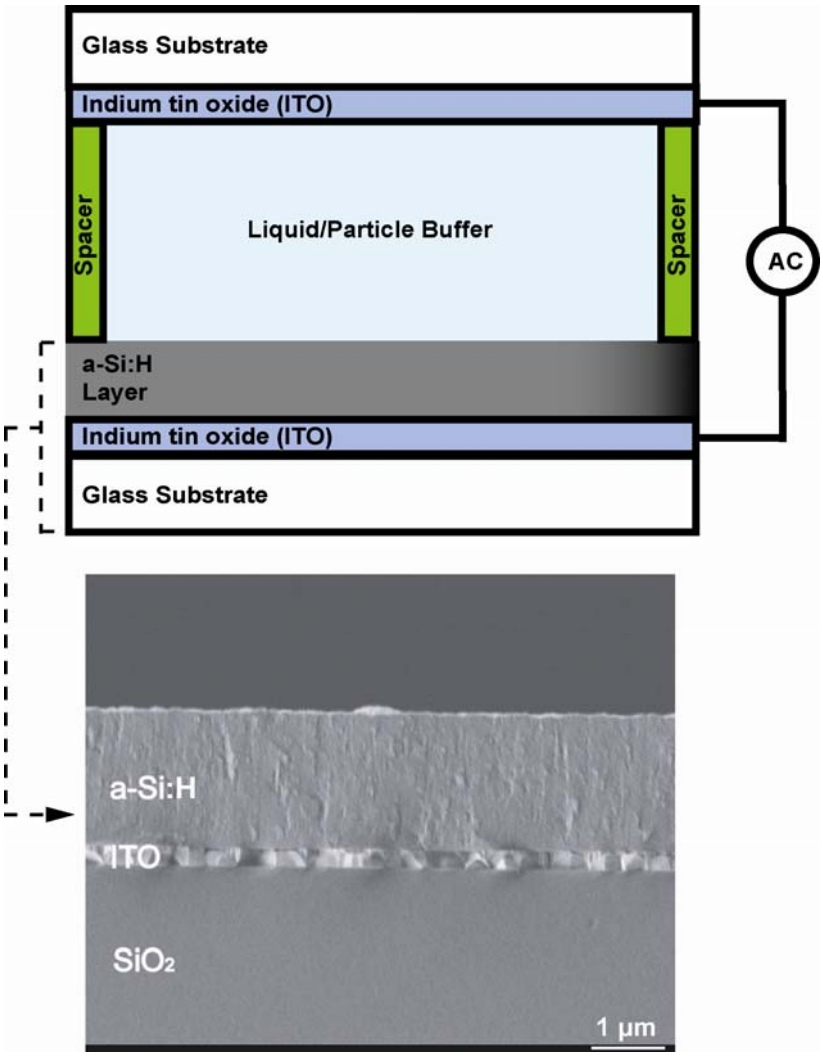

Figure 2.1 Optoelectronic tweezers (OET) device structure. The OET device consists of a top transparent ITO electrode and a bottom ITO electrode. There is a layer of photoconductive material (hydrogenated amorphous silicon) on top of the bottom electrode. An AC voltage is applied between the two electrodes. A spacer separates the top and bottom surface to form the OET chamber. The inset is an SEM image of the OET device bottom surface cross-section.

Figure 2.2 shows two common configurations for OET actuation used in this work. Figure 2.2a shows the setup for OET actuation using a low-power single laser source. The observations are made through the top microscope objective and additional bottom objective is used to focus the laser source onto the OET device. Figure 2.2b shows actuation of the OET device using a

spatial light modulator. In this case, the generated light patterns are focused onto the OET surface through the same microscope objective used for observation.

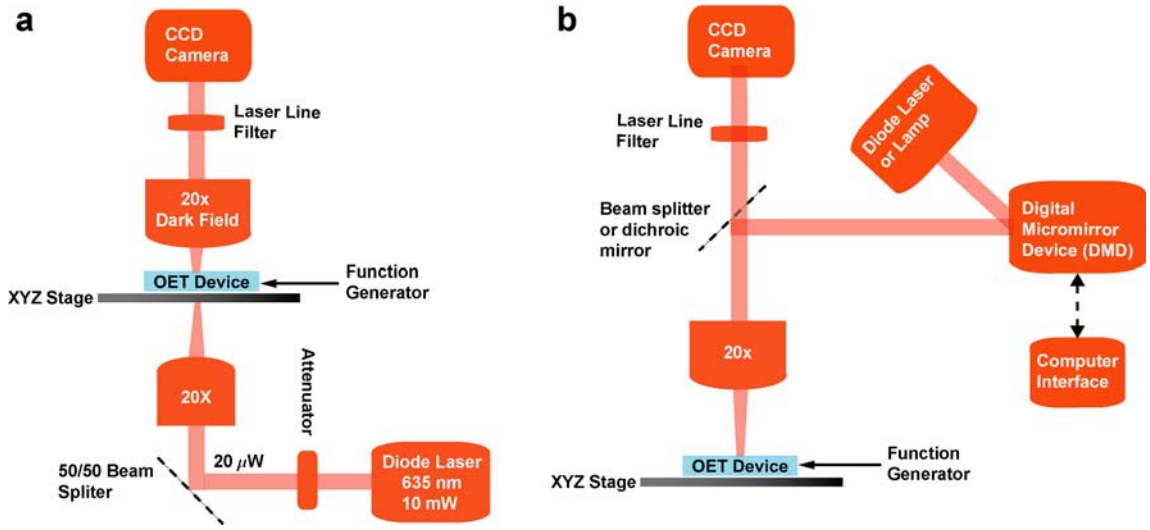

Figure 2.2 Optical setups for OET actuation. (a) A single low-power laser source is focused onto the OET device using a bottom objective and observations are made through the top microscope objective. (b) Dynamic light patterns are generated by projecting a diode laser or lamp onto a digital micromirror device (DMD) and are focused onto the OET device using the same observation objective lens.

The relaxed requirements on optical actuation of OET make it possible to integrate the OET optical manipulation setups with other forms of optical spectroscopy and characterization. An example of such techniques is Raman spectroscopy [90-92], which is an optical spectroscopic technique used to study the vibrational or rotational modes of molecules. In this technique, photons generated by a monochromatic light source (such as a laser) are inelastically scattered by the molecules and collected by an objective lens. A notch or high pass filter is typically used to remove the laser line and the remaining signal is sent to a spectrometer and detector to identify the "fingerprints" of the molecules. The "fingerprints" of the molecules are unique since their vibrational modes are related to the chemical structure of each molecule. Therefore, Raman spectroscopy is an important technique in chemical and biological characterization and identification of various materials. As we will see in future chapters, integration of OET with Raman spectroscopy opens up many possibilities for in-situ characterization and detection of trapped objects.

2.3 Optoelectronic Tweezers Device Operation

OET device actuation is achieved by modulating the impedance of the photoconductive layer (a-Si:H). Figure 2.3 shows the experimental photoconductivity values of a-Si:H as a function of the light intensity. The measurements were done by continuously attenuating a 10 mW, 632 nm diode laser focused onto a 50 μm×50 μm a-Si:H area. Voltage sweeps were applied to aluminum electrodes fabricated on the a-Si:H layer to measure the photocurrents and extract the photoconductivity values. In the absence of light, the dark conductivity of a-Si:H is approximately 10^{-5} S/m. With light illumination, electron-hole pair carriers are generated in the

photoconductive material and the photoconductivity is increased by 3 orders of magnitude to approximately 10^{-2} S/m, using a 10-100 W/cm^2 illumination intensity. The amount of light absorbed by a-Si:H is a function of its absorption coefficient which depends strongly on the illumination wavelength [93]. The absorption coefficient of a-Si:H is approximately 10^4 cm^{-1} in the visible region, which corresponds to a 90% absorption length of ~1 μm, the typical thickness of the a-Si:H layer in the OET device. Even though a-Si:H has large absorption coefficients in the UV region (10^5-10^6 cm^{-1}), the absorption length is ~100 nm and cannot fully actuate the OET device, however, reducing the thickness of a-Si:H can potentially enable UV actuation. On the other hand, a-Si:H absorption coefficient for near infrared is approximately 10^3 cm^{-1}, therefore, larger intensity illumination is required to actuate the OET device at these wavelengths.

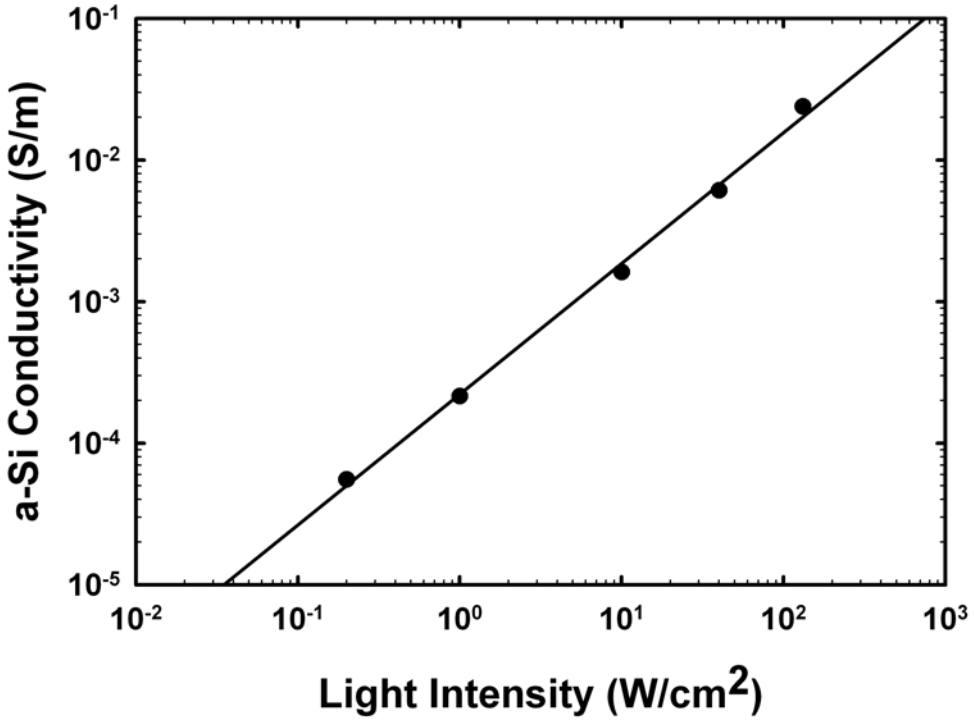

Figure 2.3 Experimental photoconductivity of a-Si:H as a function of optical intensity. [68]

To better understand the operation of the OET device, we can model it using a simple lumped circuit element model shown in Figure 2.4. When there is no light present (Figure 2.4a), the impedance of the photoconductive layer (a-Si:H), Z_{PC}, is higher than the impedance of the liquid layer, Z_L, therefore, the majority of the applied AC voltage is dropped across the photoconductive layer. However, when the light source is present (Figure 2.4b), the impedance of the photoconductive layer is reduced locally, creating a "virtual electrode", causing the majority of the AC voltage to drop across the liquid layer.

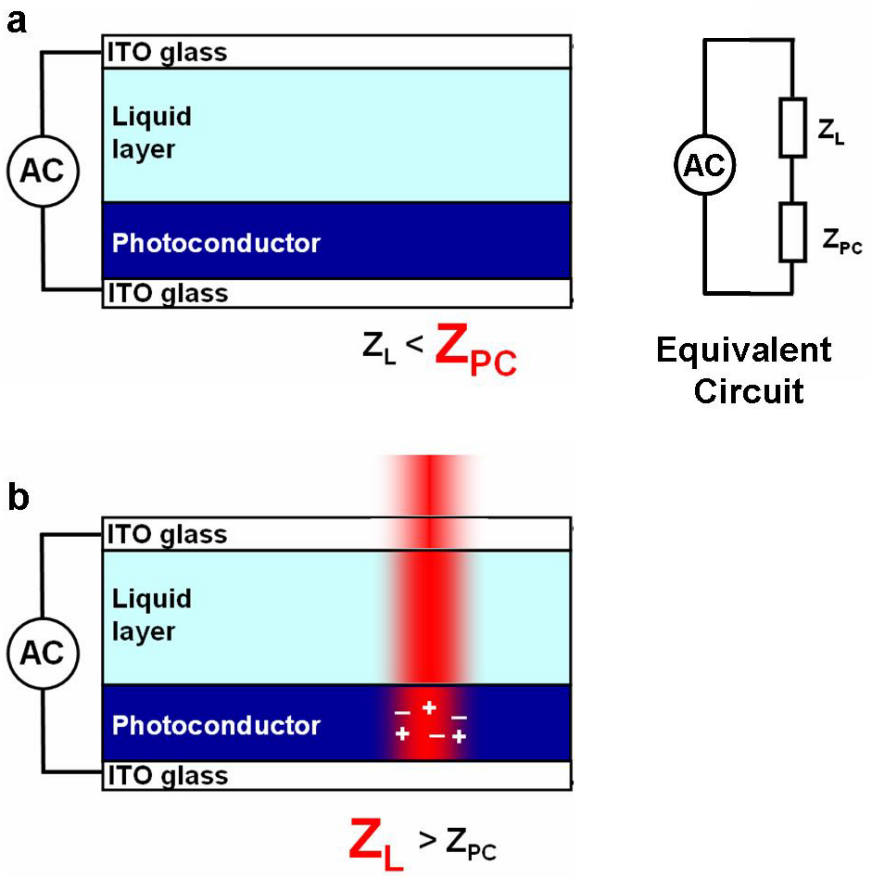

Figure 2.4 OET device operation principle. (a) In the dark state, the impedance of the photoconductive layer is higher than the impedance of the liquid layer and most of the voltage is dropped across the photoconductive layer. (b) Once the light source is applied, it generates electron-hole pairs in the photoconductive layer, reducing its impedance below that of the liquid layer, and transferring the voltage to the liquid layer in the illuminated area.

It is important to note that the impedance of the photoconductive layer is reduced only in the area that the light source is present. This is due to a-Si:H's small ambipolar diffusion length of 115 nm [94] which confines the actuated area to within the illumination region. Therefore, the resolution of the OET device virtual electrodes is fundamentally limited by the light source diffraction limit given by [95]:

$$\text{Diffraction Limit} = 1.22\frac{\lambda}{2N.A.} \tag{2.1}$$

where, λ is the wavelength of illumination and N.A. is the numerical aperture of the objective lens. Using a typical illumination wavelength of 630 nm and N.A. = 0.6, we achieve a diffraction limited spot of approximately 630 nm.

Typical liquid conductivities used for optimal OET device operation are between 1-10 mS/m. At liquid conductivity values higher than this range, the impedance of the liquid layer would be

much lower than the a-Si:H layer even under illumination, therefore, impeding the transfer of voltage from the a-Si:H layer to the liquid layer.

Since the voltage is transferred to the liquid layer only in the illuminated area, a non-uniform electric field is created in the liquid layer as shown in Figure 2.5. The interaction of this non-uniform field with the particles, liquid media, and the virtual electrodes creates various electrokinetic forces under different operational regimes. In the next section, we will explore and characterize the electrokinetic forces observed in the OET device.

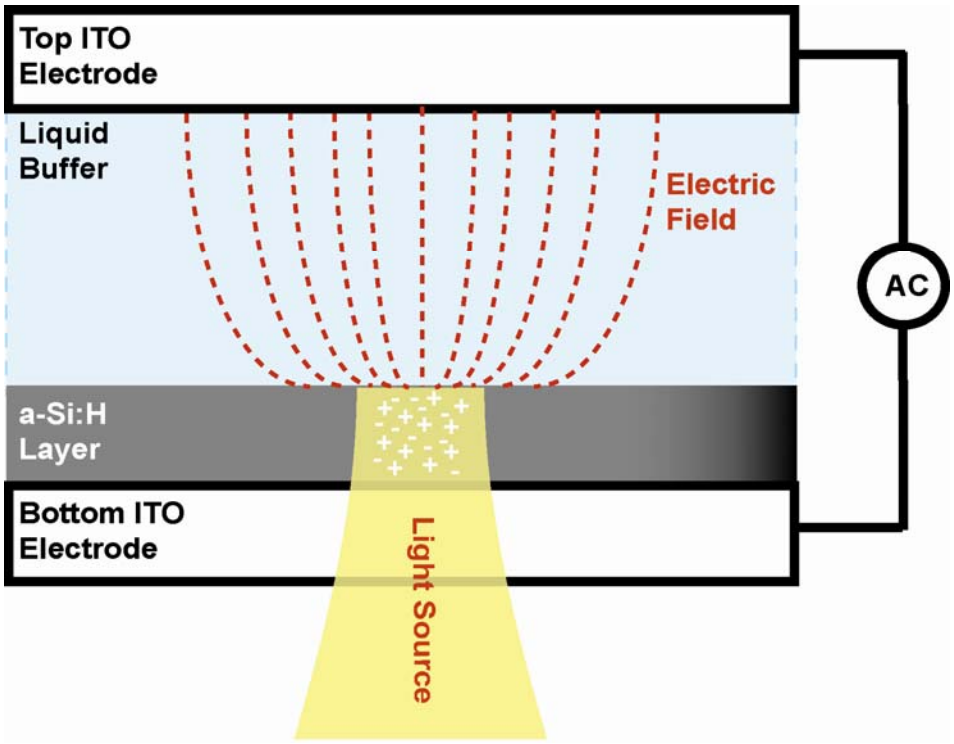

Figure 2.5 The non-uniform electric field created in the OET chamber due to the transfer of voltage from the a-Si:H layer to the liquid layer in the virtual electrode area.

2.4 Electrokinetic Forces Present in OET

2.4.1 Finite element modeling of OET device

To study the various electrokinetic effects in OET, we will use finite element simulations (COMSOL Multiphysics) to model the OET device operations. Table 2.1 summarizes various parameters used in modeling the OET device.

Parameter	Symbol	Value/Expression
Liquid conductivity	σ_{liquid}	10^{-3}-10^{-2} S/m
Relative permittivity of liquid	ε_{liquid}	78

Thermal conductivity of liquid	k_{liquid}	0.6 W/(m.K)
Dynamic viscosity of liquid	η_{liquid}	8×10^{-4} Pa.s
Relative permittivity of amorphous Silicon	ε_{aSi}	11.7
Dark conductivity of amorphous silicon	σ_{dark}	10^{-6} S/m
Light conductivity of amorphous silicon	σ_{light}	$0.01\times\left(\exp\left(-\frac{2x}{(20\times10^{-6})^2}\right)\times\exp\left(-\frac{2y}{(20\times10^{-6})^2}\right)\right)+10^{-5}$ S/m
Thermal conductivity of amorphous silicon	k_{aSi}	1 W/(m.K)
Relative permittivity of glass	ε_{glass}	2.09
Glass conductivity	σ_{glass}	10^{-14} S/m
Thermal conductivity of glass	k_{glass}	1.38 W/(m.K)

Table 2.1 Parameters used for finite-element modeling of the OET device.

To model the effect of illumination on amorphous silicon conductivity, σ_{light}, we represent σ_{light} using a Gaussian profile that follows the light source pattern as indicated in Table 2.1. Figure 2.6 shows the typical electric field distribution in the OET device with an applied voltage of 10 Vpp at 100 kHz and using the various parameters in Table 2.1. The color map indicates the magnitude of the electric field and the arrows indicate the direction of the field. It is evident that the electric field has a non-uniform profile inside the liquid area with the strongest gradient close to the a-Si:H bottom surface.

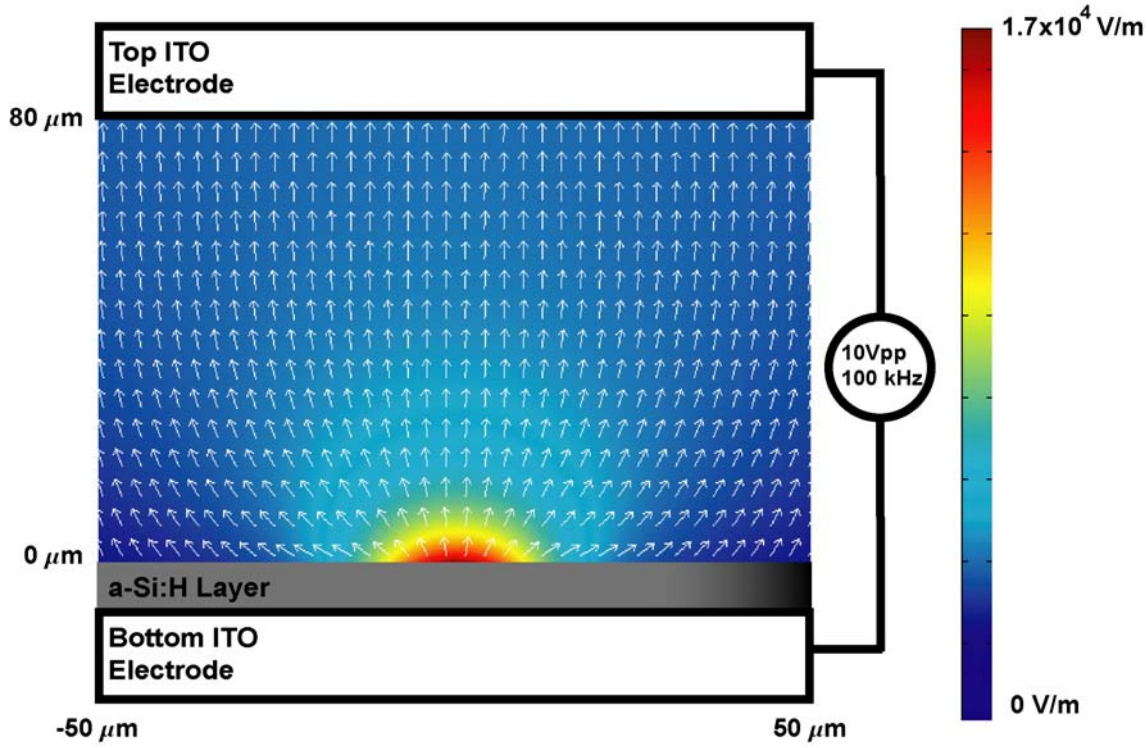

Figure 2.6 The simulated electric field profile in the OET device for an applied voltage of 10 Vpp at 100 kHz. The non-uniform field profile is clearly seen with the strongest gradients present near the bottom amorphous silicon surface.

2.4.2 Dielectrophoresis (DEP)

The first electrokinetic effect that we will describe in the OET device is the dielectrophoresis (DEP) force. DEP is a technique that uses the interaction of a non-uniform electric field with the induced dipoles on the particles to attract or repel the particles from areas of highest electric field intensity gradient. In the presence of a non-uniform electric field (E), a dipole moment (p) is induced in the particles with unequal charges on two ends. Therefore, the dipole feels a net force towards or away from areas of highest field intensity gradients depending on the AC bias frequency and properties of the particles and the liquid solution. By taking the difference between the forces experienced by the charges at the two ends of the dipole, we can approximate the DEP force as [96]:

$$F = (p \cdot \nabla)E \tag{2.2}$$

To calculate the DEP force expression on various objects, the particles are assigned an effective dipole moment which is the moment of a point dipole that creates an identical electrostatic potential when immersed in the imposed electric field. By comparing the electrostatic potential of the particle of interest to the electrostatic potential of a point dipole, and by ignoring the higher order terms in the Taylor expansion of the electric field, the following formula is derived for the DEP force on a spherical particle [96]:

$$\langle F_{DEP} \rangle = 2\pi r^3 \varepsilon_m \,\mathrm{Re}\{K^*(\omega)\}\nabla E^2 \tag{2.3}$$

$$K^*(\omega) = \frac{\varepsilon_p^* - \varepsilon_m^*}{\varepsilon_p^* + 2\varepsilon_m^*},\ \varepsilon_m^* = \varepsilon_m - j\frac{\sigma_m}{\omega},\ \varepsilon_p^* = \varepsilon_p - j\frac{\sigma_p}{\omega} \tag{2.4}$$

where r is the radius of the particle, ε_m and ε_p are the permittivities of the medium and the particle respectively, σ_m and σ_p are the conductivities of the media and the particle respectively, ω is the frequency of the AC potential, $\mathrm{Re}\{K^*\}$ is the real part of the Clausius-Mossotti (C.M.) factor (K^*), and ∇E^2 is the gradient of the electric field intensity. The C.M. factor is a function of the permittivity and conductivity of the particle and the medium, and in the case of spherical particles, has a value between -0.5 and 1. For particles that are more polarizable than the surrounding medium, the C.M. factor is positive and the particles experience a positive DEP force. However, the particles less polarizable than the surrounding medium experience a negative DEP force and are repelled from regions of highest electric field intensity gradient. The other important parameter that determines the magnitude of the DEP force is the gradient of the field intensity. In the OET device, ∇E^2 has its maximum close to the OET surface and falls off rapidly as we move further away from the surface. Figure 2.7 shows the normalized field intensity gradient as a function of distance from the OET surface at the center of the illuminated area. It is evident that the ∇E^2 magnitude drops by 1-2 orders of magnitude 10 μm away from the OET surface and it falls by roughly 3 orders of magnitude 50 μm away from the OET surface. Therefore, particles feel the maximum trapping force near the OET surface.

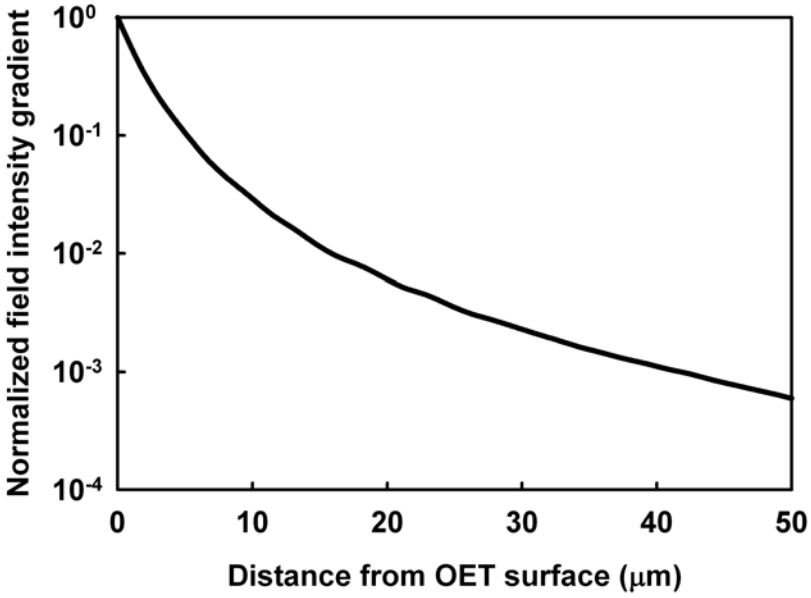

Figure 2.7 Normalized gradient of field intensity (∇E^2) as a function of distance from the OET surface in the center of the illuminated area.

Many of the nanostrucures of interest such as nanowires. carbon nanotubes, and biomaterials such as bacteria, viruses, and DNA have anisotropic geometries and can typically be modeled as

cylindrical objects. Therefore, it is important to analyze the DEP force expression for particles with anisotropic geometries. Cylindrical objects with radius r and length l can be modeled as elongated ellipsoids with *a*, *b*, and *c* dimensions, where $b = c = r$ and $a = l/2$. The effective dipole moment along the length of the ellipsoid is given by [96]:

$$(p_{eff})_l = \frac{2\pi r^2 l}{3}\varepsilon_m \left[\frac{\varepsilon_p^* - \varepsilon_m^*}{\varepsilon_m^* + (\varepsilon_p^* - \varepsilon_m^*)L_l}\right]E_l \tag{2.5}$$

where $\varepsilon^* = \varepsilon - j\sigma/\omega$, subscripts *m* and *p* denoting complex permittivity of medium and particle respectively, and L_l is the depolarization factor along the long axis of the ellipsoid. Similar expressions can be derived for polarization along the short-axis of the ellipsoid. The depolarization factor is defined by an elliptical integral and for an elongated ellipsoid, it can be approximated to be [96]:

$$L_l = \frac{lr^2}{4}\int_0^\infty \frac{ds}{(s+(l/2)^2)^{3/2}(s+r^2)} \approx 2r^2(\ln(1+f/1-f) - 2f)/l^2 f^3 \tag{2.6}$$

where,

$$f = \sqrt{(1-\ln(2r/l)^2} \tag{2.7}$$

For ellipsoids with high aspect ratio ($l >> r$), we have $L_l << L_r$ which results in much stronger polarization along the long-axis of the elongated ellipsoids.

Once the expression of the ellipsoid's effective dipole moment is known, the DEP force can be approximated using equation 2.2 as:

$$F_{DEP} = \left[\frac{2\pi r^2 l}{3}\varepsilon_m \left[\frac{\varepsilon_p^* - \varepsilon_m^*}{\varepsilon_m^* + (\varepsilon_p^* - \varepsilon_m^*)L_l}\right]E_l.\nabla\right]E_l = \left(\frac{\pi r^2 l}{3}\right)\varepsilon_m K\nabla(E_l^2) \tag{2.8}$$

where

$$K = \frac{\varepsilon_p^* - \varepsilon_m^*}{\varepsilon_m^* + (\varepsilon_p^* - \varepsilon_m^*)L_l} \tag{2.9}$$

which is the C.M. factor for ellipsoidal particles. Therefore, the time-averaged DEP force is given by:

$$\langle F_{DEP}\rangle = \left(\frac{\pi r^2 l}{6}\right)\varepsilon_m \,\mathrm{Re}\{K\}\nabla(E_l^2) \tag{2.10}$$

For high aspect ratio ellipsoids, the depolarization factor along the long axis of the particle is much smaller than depolarization factor for spherical particles (1/3). Therefore, the real part of the C.M. factor can be much larger than one for elongated ellipsoids ($\mathrm{Re}\{K_{Ellipsoid}\} >> 1$), as opposed to the C.M. factor of spherical particles, which has a value between -0.5 to 1 ($-0.5 \leq$

Re$\{K_{Spherical}\} \leq$ 1). Therefore, the DEP force for high-aspect ratio ellipsoids is considerably enhanced compared to spherical particles with similar dimensions. Figure 2.8 shows the value of the CM factor as a function of the aspect ratio of the particle, assuming a frequency of 100 kHz, liquid relative permittivity ε_m = 80 and conductivity σ_m = 10 mS/m, and particle relative permittivity ε_p = 12 and conductivity σ_p = 10 S/m. For an aspect ratio equal to two, such as spherical particles, the CM factor is 1 (due to high polarizability of the particle assumed here). However, as the aspect ratio of the particle increases, corresponding to particles with ellipsoidal and cylindrical geometries, the value of the CM factor increases by 2-3 orders of magnitude, for aspect ratios over 100.

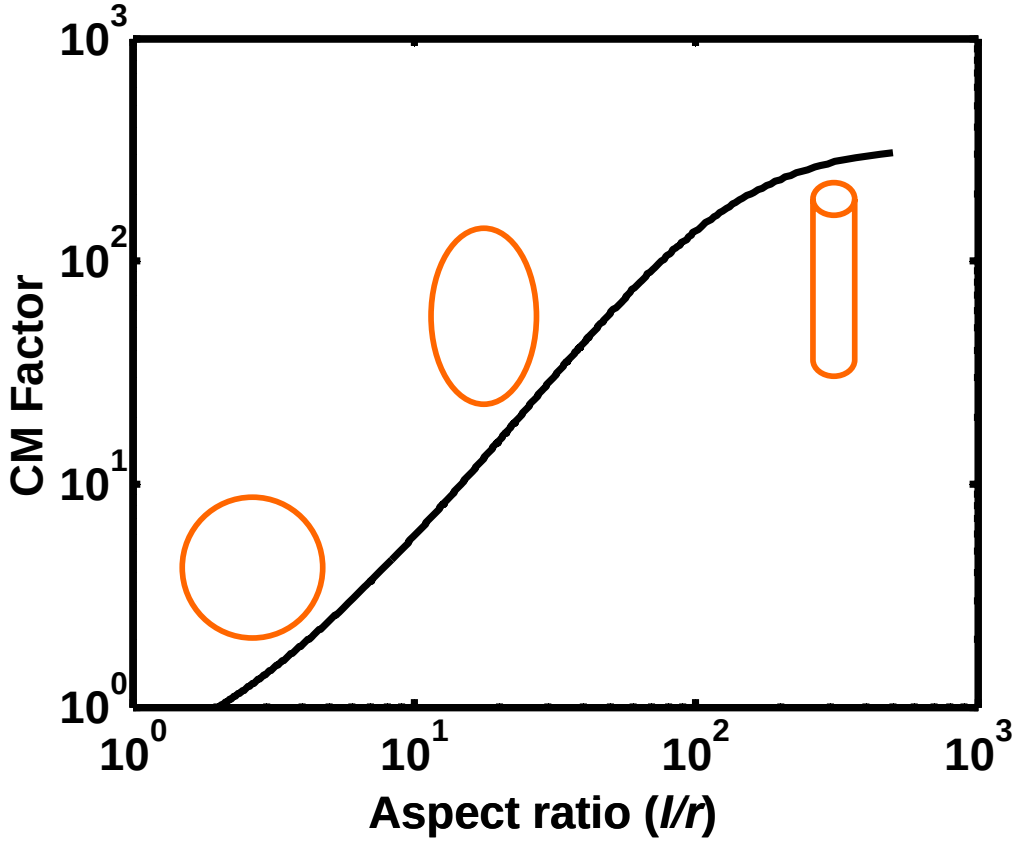

Figure 2.8 The value of the Clausius-Mossotti factor as a function of the aspect ratio of the particle.

This enhancement in the C.M. factor value has important implications in DEP manipulation of particles with anisotropic geometries such as nanowires and carbon nanotubes and we will explore how it affects the trapping of such objects in the next chapters.

Cylindrical objects in a non-uniform electric field also experience a torque aligning them with the electric field lines. The torque for cylindrical objects is given by [96]:

$$T_z = \frac{4\pi r l^2 (\varepsilon_p - \varepsilon_m)^2 (L_r - L_l) E_{0,l} E_{0,r}}{3\varepsilon_m \left[1 + \frac{\varepsilon_p - \varepsilon_m}{\varepsilon_m} L_r\right]\left[1 + \frac{\varepsilon_p - \varepsilon_m}{\varepsilon_m} L_l\right]} \tag{2.11}$$

$$\Rightarrow \quad T_z \propto (L_r - L_l) E_{0,l} E_{0,r} \tag{2.12}$$

where L_r and L_l are the deplorization factors in the radius and length direction of the cylinder, respectively, and $E_{0,l}$ and $E_{0,r}$ are the electric field in the radius and length direction of the cylinder.

When objects move in a liquid medium, a net hydrodynamic force opposes the motion, this force is typically referred to as the drag force. The approximate drag forces for a spherical particle and a cylindrical object moving perpendicular to its long-axis are given by [97]:

$$F_{Drag} = 6\pi r \eta v_{drag} \tag{2.13}$$

$$F_{Drag} = \frac{8\pi\eta l v_{drag}}{(2\ln(2l/r) - 1)} \tag{2.14}$$

where η is the viscosity of the surrounding medium. When objects are transported using the DEP force in a liquid medium, we can calculate the velocity of the particles due to the DEP force by equating the DEP force to the drag force:

$$F_{DEP} = F_{drag} \tag{2.15}$$

Using this formula and equations 2.3 and 2.10 for the DEP force on spherical and elongated ellipsoidal particles, respectively, we can calculate the velocity of these particles due to the DEP force in the OET device.

Figure 2.9 shows the velocity due to the DEP force as a function of the distance from the center of the illuminated area for a spherical particle and an elongated ellipsoid. The liquid conductivity is assumed to be 1 mS/m and an AC voltage of 10Vpp at 100kHz is applied to the device. The average gradient of field intensity for each particle is calculated at a distance equal to half the length of the particle from the OET surface. The spherical particle is assumed to be a polystyrene bead with 10 μm diameter, relative permittivity ε_p = 2.56, and conductivity much lower than the liquid medium, this results in a CM factor close to -0.5. Therefore, the polystyrene bead experiences a negative DEP force. The dotted portion of the speed calculation in Figure 2.9 for the spherical particle does not present valid simulated velocities. This is because the vertical negative DEP force component will cause the particle to rise off the OET substrate near the beam center. This occurs when the vertical DEP component and buoyancy forces balance one another which occurs at around 18 μm from the beam center according to the experiments. As discussed, horizontal DEP force drops dramatically as we move away from the OET surface. Therefore, once the particle leaves the surface, the particle often slips over the light pattern and results in the loss of particle control. Therefore, the DEP-induced velocity is only meaningful for distances from the beam center at which the particle still remains on the OET surface.

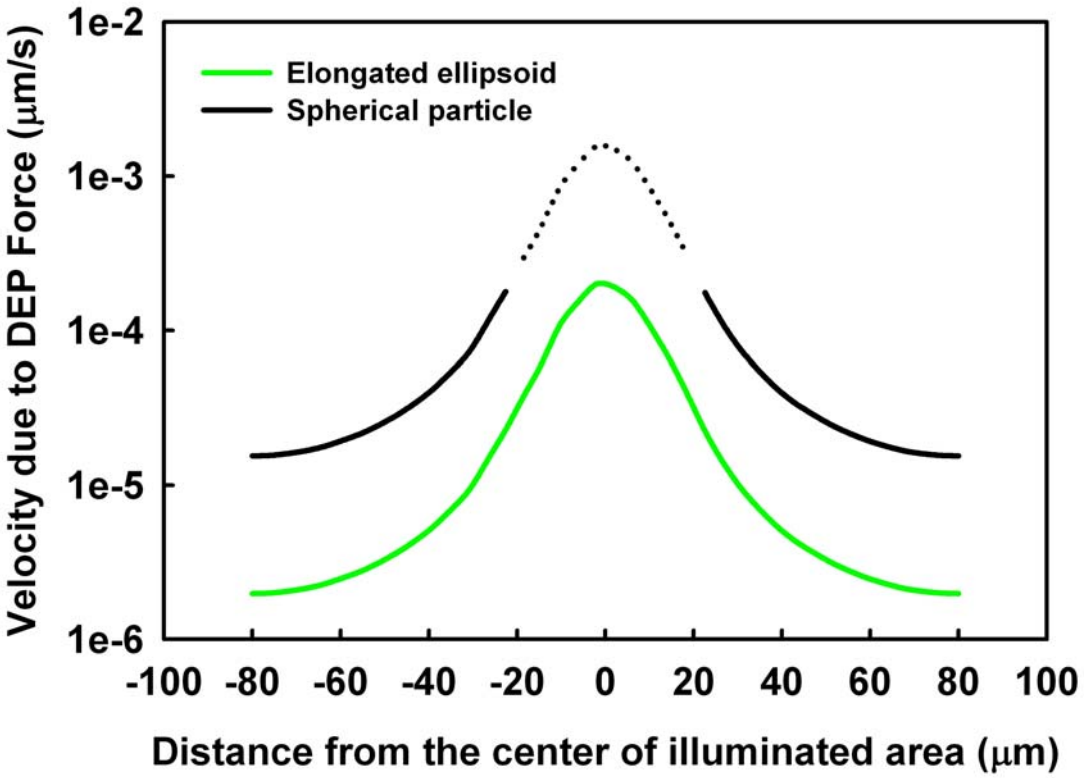

Figure 2.9 Velocity due to optically-induced DEP force in the OET device as a function of the distance from the center of the trap for a spherical particle, 10 μm in diameter (black) and an elongated ellipsoid, 5 μm in length and 100 nm in diameter (green).

The elongated ellipsoid particle is assumed to be 5 μm in length, 100 nm in diameter with relative permittivity ε_p = 12 and conductivity σ_p = 1 S/m, which results in a C.M. factor of approximately +640, therefore, the particle will experience a positive DEP force. As opposed to the polystyrene bead case, the DEP force is attractive for the elongated particle assumed here and the particle is pulled down towards the OET surface. Therefore, the large velocities in the illuminated area present valid simulated velocities. As we will discuss in future chapters, many nanoscale particles such as nanowires and carbon nanotubes have similar physical properties and can be modeled as elongated ellipsoids.

In summary, even though the elongated ellipsoidal particle has approximately 10,000× smaller volume relative to the spherical particle, they both experience DEP forces of similar magnitude in the OET device. There are three main reasons for this: First, the elongated particle has a much larger C.M. factor due its anisotropic geometry. Second, due to its higher polarizability relative to the liquid medium, the elongated particle experiences a positive DEP force and is attracted towards the illuminated area. In contrast, the spherical particle experiences a negative DEP force and is pushed up from the OET surface before it can reach the high field intensity region in the illuminated area. As we will see in future chapters, the nanostructures studied in this work experience attractive DEP forces due to their higher polarizability relative to the liquid medium. In fact, our analysis here suggests that DEP manipulation of nanoparticles

with negative DEP response would be challenging. However, this also presents an opportunity for separation and purification of nanoparticle solutions composed of particles with negative and positive DEP responses. Third, the gradient of field intensity drops rapidly as the distance from the OET surface increases, as shown in figure 2.7. Therefore, due to its smaller length, the elongated particle settles closer to the OET surface and experiences stronger average field intensities relative to the spherical particle. As we will see in Chapter 5, this is an important effect for spherical nanoparticles which are immersed in the high field region near the OET surface.

2.4.3 Light-actuated AC Electroosmosis (LACE)

The application of an electrical potential to an ionic fluid results in the formation of an electrical double layer. If a tangential electric field component is present in the double layer region, ions in the layer will move in response to this field. The velocity of these ions is referred to as the slip velocity and is expressed by the Helmholtz-Smoluchowski equation [98]:

$$v_{SLIP} = -\frac{\varepsilon_m \zeta E_t}{\eta} \tag{2.16}$$

where ε_m is the permittivity of the liquid, ζ is the zeta potential (defined as the voltage drop across the electrical double layer), E_t is the tangential electric field, and η is the fluid viscosity.

Electro-osmotic flows have been used in applications such as microfluidic pumps [99] and are generated using either a DC bias [100, 101] or an AC bias [102]. In the case of AC Electro-osmosis flow, the ionic charge at the surface of the double layer switches polarity in response to the applied AC field and results in a steady state motion of the ions in one direction. AC electro-osmosis also exhibit frequency dependence which arises from the fact that the electrical double layer acts as a capacitor and, therefore, has an intrinsic roll-off frequency. Above this critical frequency, the double layer can no longer sustain a voltage drop across itself and the zeta potential, along with the slip velocity, approach zero.

In the OET device, the creation of a virtual electrode upon localized illumination results in a tangential electric field which produces a slip velocity, resulting in light induced AC Electro-osmosis (LACE) flows [103].

In order to model this effect, an equivalent circuit model, shown in Figure 2.10a, is used to extract the zeta potential. In this model, the electrical double layer is treated as a simple parallel plate capacitor in series with resistors accounting for the liquid layer and a-Si:H layer. The double layer capacitance depends on its thickness, which is a function of the liquid conductivity. This relationship, described by Gouy-Chapman theory, is governed by the following equation [104]:

$$d = \left(\frac{2\sigma_m z^2 e}{\mu_m \varepsilon k T} \right)^{-1/2} \tag{2.17}$$

where σ_m is the liquid conductivity, μ_m is the bulk ion mobility (8×10^{-8} $m^2/(V.s)$ for KCl), z is the valence of the ion (e.g. 1 for KCl), e is the charge on an electron, k is Boltzmann's constant, and T is the temperature. We assume that $\sigma_m = e\mu_m n^0$, where n^0 is the bulk ion concentration. Figure

2.10b shows the dependence of the electrical double layer thickness on the liquid conductivity. For a 1 mS/m solution, the double layer thickness is calculated to be approximately 25 nm.

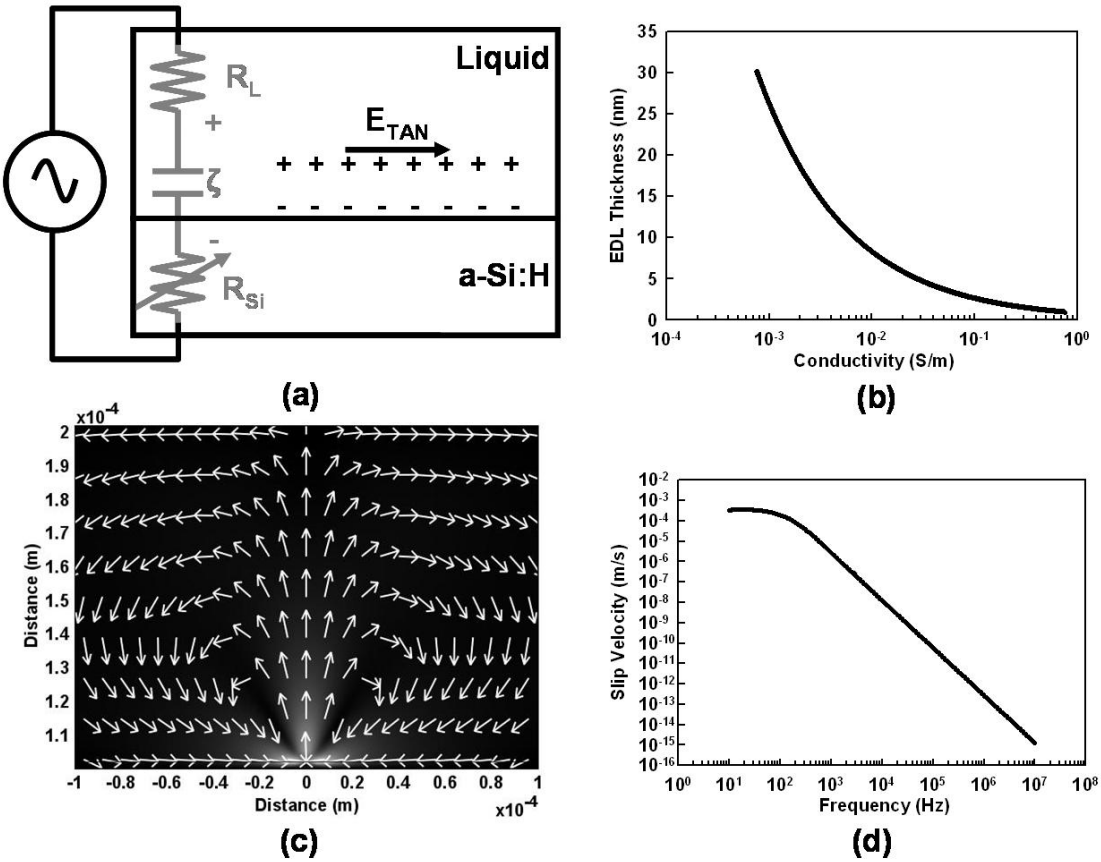

Figure 2.10 (a) Equivalent circuit schematic of LACE. Ions in the electrical double layer respond to tangential electric resulting in a slip velocity. (b) Electrical double layer (EDL) thickness versus KCl conductivity. (c) Fluid flow pattern due to LACE in the absence of other forces at 1 kHz. (d) Fluid velocity due to LACE versus frequency. (© IEEE [68])

Once the zeta potential is known, the tangential electric field is extracted from finite-element simulations and a slip velocity is calculated. This velocity is entered into the Navier-Stokes equation as a boundary condition at the a-Si:H/liquid interface. The resulting fluid flow pattern is shown in Figure 2.10c. Similar to AC electro-osmosis, LACE also exhibits frequency dependence; Figure 2.10d shows the maximum fluid flow due to LACE versus frequency.

2.4.4 Electrothermal Flow

The energy of incident photons absorbed in the a-Si:H is dissipated through either electron-hole pair or phonon generation. The latter can be modeled as a localized heat source in the a-Si:H layer. Additionally, joule heating in the liquid occurs from the applied electric field according to the equation:

$$W = \sigma_m E^2 \tag{2.18}$$

where W is the power generated per unit volume and σ_m is the conductivity of the medium.

The generated heat results in a gradient in electrical permittivity and conductivity in the solution. In turn, these gradients interact with the surrounding electric field to produce a body force on the surrounding liquid. The time averaged force per unit volume on the liquid is given by the following equation [105]:

$$\left\langle f_{ET} \right\rangle = \frac{1}{2}\mathrm{Re}\left[\left(\frac{\sigma_m \varepsilon_m}{\sigma_m + i\omega\varepsilon_m}\left(\kappa_\varepsilon - \kappa_\sigma\right)\right)\left(\nabla T \cdot E\right)E^*\right] - \frac{1}{2}\left|E\right|^2 \kappa_\varepsilon \varepsilon_m \nabla T \tag{2.19}$$

where κ_σ and κ_ε are empirical constants which represent the percentage change per unit temperature in conductivity and electrical permittivity, respectively. For typical electrolytes, κ_σ = 2% K^{-1} and κ_ε = -0.4% K^{-1} [105].

The simulated fluid temperature distribution in the OET device for a 1 mW laser with a 20 μm beam diameter (250 W/cm^2) at a bias of 20 Vpp is shown in Figure 2.11a. The maximum temperature increase is about 2.4 K. By calculating the temperature distribution for a given optical power density and bias, equation 2.19 can be entered into the Navier-Stokes equation as a perturbing force and the resulting fluid flow can be observed (Figure 2.11b). The maximum fluid velocity versus optical power (in the absence of all other effects) is shown Figure 2.11c. It is important to note that the effects of ET flow will be dominant at high optical power densities (higher temperature gradients) and high electric fields.

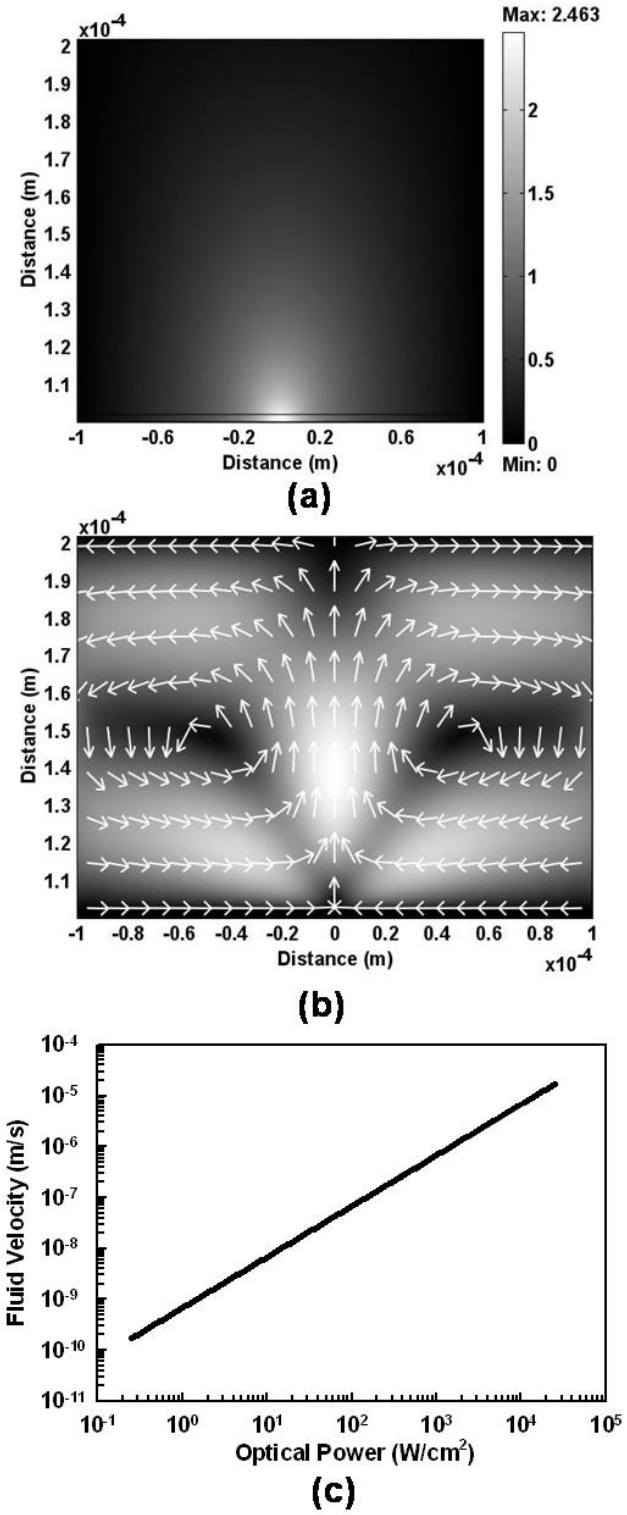

Figure 2.11 (a) Temperature increase distribution due to a 1 mW laser focused to a 20 μm spot size. (b) Simulated flow due to electro-thermal effects. (c) Dependence of ET fluid velocity on incident optical power. (© IEEE [68])

2.4.5 Electrolysis

The electrolysis effect is observed in the OET device when a DC voltage or an AC voltage with frequency below 1 kHz is applied to the device. The formation of bubbles due to electrolysis interferes with the OET operation and can potentially damage the photoconductive layer; therefore, operational regimes at which the electrolysis can occur are usually avoided.

2.4.6 Buoyancy

The density of a liquid is a function of temperature. Therefore, a localized temperature gradient can result in a fluid density gradient which, under the influence of gravity will result in fluid flow. This flow can be characterized by the following equation [106]:

$$f_G = \frac{\partial \rho_m}{\partial T} \Delta T \cdot g \tag{2.20}$$

where, ρ_m is the fluid density, ΔT is the change in temperature, and g is the acceleration due to gravity (9.8 m/s^2).

Unlike the other effects mentioned already, this flow can occur in the OET device in the absence of an applied bias. Thus, given a high enough temperature gradient, it is possible to move objects in the absence of applied bias.

This force, like the ET force, is entered into the Navier-Stokes equation as a fluidic perturbation. The resulting fluid flow is shown in Figure 2.12a. The maximum fluid velocity versus optical power density is shown in Figure 2.12b. The magnitude of buoyancy driven flow is much less than the other effects. Therefore, we do not expect buoyancy to play a role in OET operation except in the absence of external biasing.

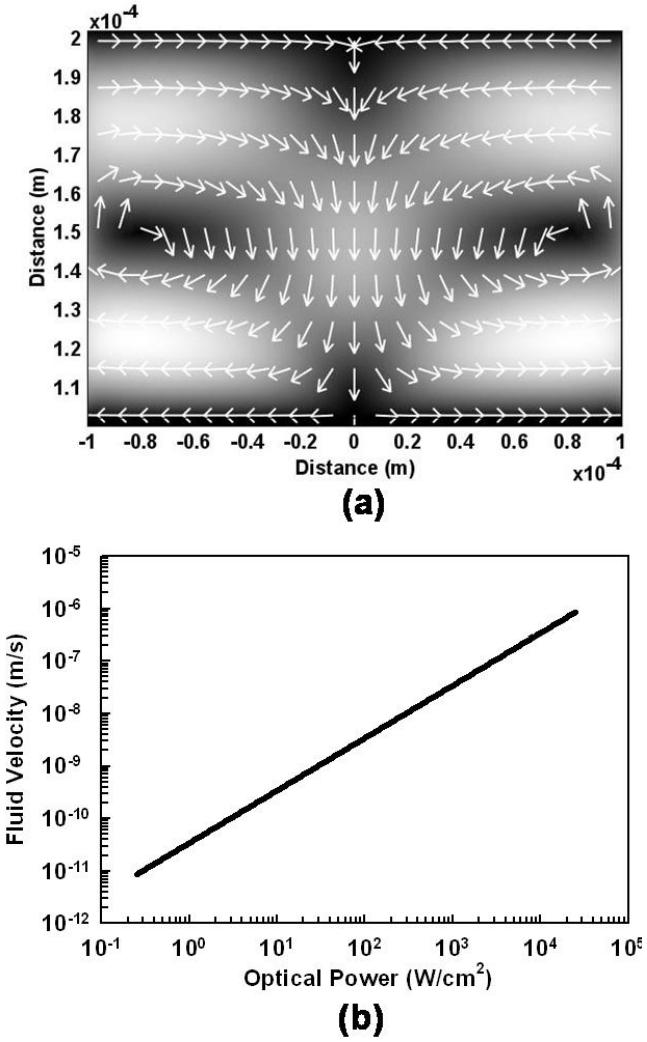

Figure 2.12 (a) Simulated fluid flow due to buoyancy effects. (b) Dependence of buoyancy fluid velocity on optical power. Note that the fluid velocity due to buoyancy is much smaller than that imposed by the other effects. (© IEEE [68])

2.4.7 Figure of merit

In order to determine which of the aforementioned effects is dominant for a given set of device and bias conditions, a figure of merit has been developed. Since all of the effects described eventually manifest themselves as a fluid or particle velocity, it makes sense to use this factor as a means for comparison. Specifically, we can compare the speed due to DEP force to that induced by other effects in the fluid. Thereby, we define a dimensionless value β for each point in the liquid as:

$$\beta \equiv \frac{X_{DEP} - X_{EXT} - \langle X_{BROWNIAN} \rangle}{X_{DEP} + X_{EXT} + \langle X_{BROWNIAN} \rangle} \tag{2.21}$$

where X_{DEP}, X_{EXT}, and $\langle X_{BROWNIAN} \rangle$ refer to the distance the particle travels in one second due to DEP force, external forces (LACE, ET, and Buoyancy), and Brownian motion, respectively. The average distance a spherical particle travels in one second due to Brownian motion is defined as [107]:

$$\langle X_{BROWNIAN} \rangle = \sqrt{\frac{kT}{3\pi\eta r}} \tag{2.22}$$

Therefore, a β value close to 1 corresponds to near complete dominance, or control, by the DEP force. Likewise, a β value near -1 indicates DEP force has little control over the particle motion.

Applying this definition of β to the simulation grid, we can calculate a value of β for each point in the mesh. It is therefore necessary to reduce this array of β values down to a single number, or figure of merit. Thus, we define a number B as:

$$\mathrm{B} \equiv \frac{1}{A}\int_{A} \beta dxdy, \mathrm{x} \in [-\mathrm{r}, \mathrm{r}], \mathrm{y} \in [0, \mathrm{d}] \tag{2.23}$$

where r is defined as the control radius, d is the thickness of the liquid layer, and A is the area of integration equal to $2 \times r \times d$. The control radius is determined by the greatest radius from the beam center at which particle perturbation is expected, since fundamentally, ignoring other effects, DEP can induce a particle velocity at a distance. Therefore, B is an average value of β over a predefined area and has a value between -1 and 1 which can be interpreted as the extent of DEP control for a given set of parameters. Figure 2.13 shows the experimental and simulated results for various OET operational regimes. Simulated values of normalized B are plotted on a contour plot while experimental results are overlaid as points. The experimental results follow the B contour lines quite well. It appears that, for this liquid solution, a normalized B value of greater than 0.8 results in DEP actuation. DEP actuation, as predicated by the theory, is overcome by LACE at low frequencies, ET at high optical powers, and both LACE and ET at high optical powers and low frequencies. Therefore, it appears that to ensure DEP dominance over external effects (e.g. LACE, ET, Buoyancy) the OET device should be operated at frequencies above the LACE cutoff (~1 kHz for 1 mS/m solution) and low optical powers (less than 1 kW/cm^2) to prevent ET flow effects.

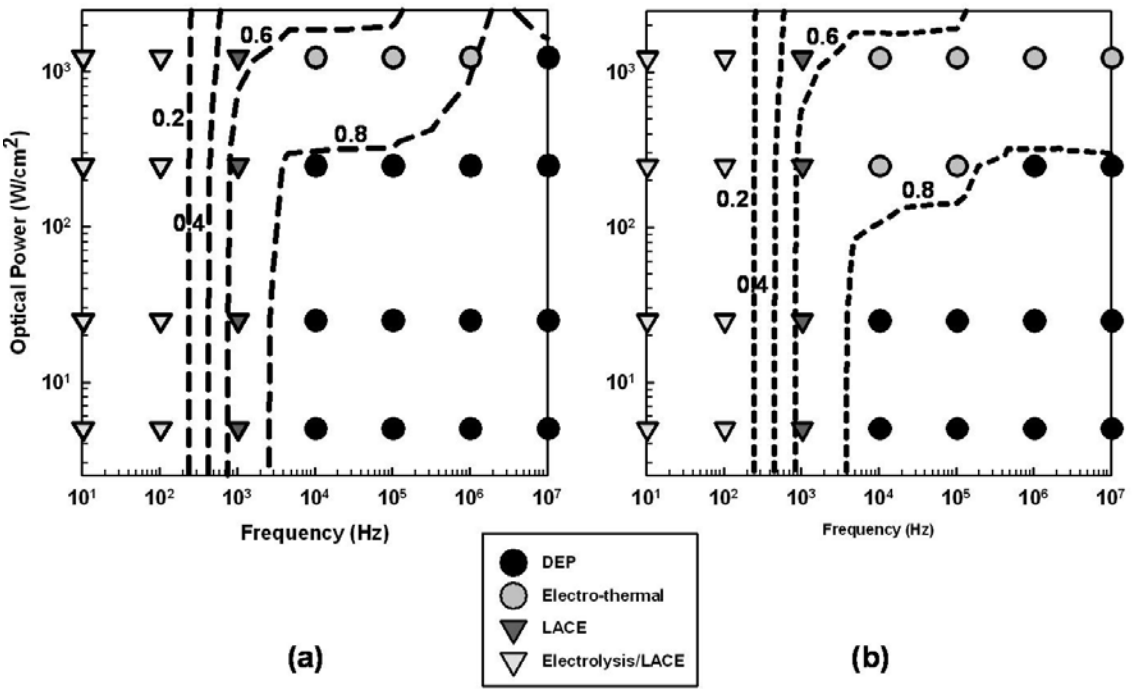

Figure 2.13 Overlay of observed dominant effect with theoretical predictions for 1 mS/m at (a) 20 Vpp and (b) 10 Vpp. (© IEEE [68])

2.5 Summary

In this chapter, we have described the optoelectronic tweezers device and characterized the various electrokinetic forces present in the OET device. There are three main operational regimes in the OET device: dielectrophoresis (DEP), electro-thermal (ET) flow, and light-actuated AC electro-osmosis (LACE). These different operational regimes can be achieved in OET by tuning the parameters such as optical power and frequency. Figure 2.14 shows which effect dominates in the OET device as a function of optical power and frequency.

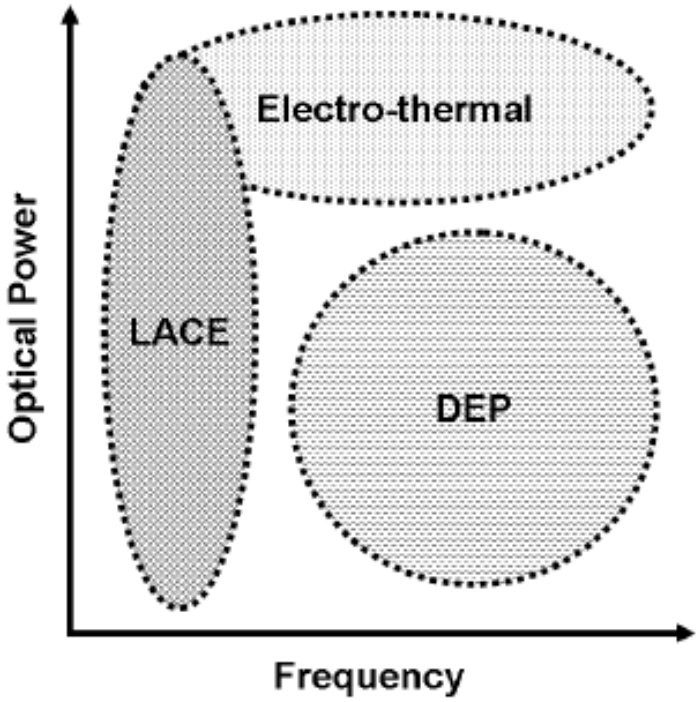

Figure 2.14 OET operational regimes as a function of optical power and frequency.

In the next chapters, we will take a closer look at applications of the OET device to nanoscale particles and explore the use of the various electrokinetic effects introduced in this chapter, in particular light-induced dielectrophoresis, for manipulation, assembly, and patterning of various nanostructures.

Chapter 3 Dynamic Manipulation and Separation of Individual Seminconducting and Metallic Nanowires

3.1 Motivation

In the past decade, many synthesis techniques have been developed to create nanowires with various material properties and shapes. Nanowires unique physical properties make them attractive candidates for fabrication of a range of novel high performance electronic and optoelectronic devices. However, heterogeneous integration of nanowires requires development of techniques for manipulation of individual nanowires with arbitrary composition. Current integration techniques either lack the capability to manipulate nanowires in a large-scale and flexible fashion or are unable to address individual nanowires. In this chapter, we will demonstrate the use of OET for large-scale and dynamic manipulation, assembly, and separation of individual nanowires, therefore, establishing OET as an important optoelectronic method for heterogeneous nanowire organization.

3.2 Manipulation of Nanowires

3.2.1 Modeling and Simulation

As mentioned before, OET works based on the optically-induced dielectrophoresis (DEP) principle. Since the magnitude of the DEP force scales with the volume of the particle, OET trapping of particles becomes more challenging as their size reduces. However, there are a variety of factors that can be exploited to overcome this challenge. As discussed in section 2.4.2, the theory of dielectrophoretic trapping [96] suggests that one way to manipulate objects with sub-micron dimensions is to work with highly elongated structures, where two dimensions of the

particle can be significantly below 100 nm, while the third dimension is on the order of micrometers. This can be seen bu modeling the force using an elongated ellipsoid model [96], the DEP force for a nanowire is given by equation 2.10. For nanowires that are much more polarizable than the surrounding media and have high aspect ratios, the C.M. factor can be much larger than 1.

Figure 3.1a shows the schematic of the electric field distribution around a nanowire inside the OET device. Using the finite element simulations to approximate field gradients we can estimate the corresponding forces on suspended nanowires. We can also compare the magnitude of the DEP force on a nanowire (length = 5 μm) and a spherical particle over a range of radii, assuming the same field intensity for both cases (Figure 3.1b). It is evident that the nanowire experiences a DEP force two to three orders of magnitude larger than the spherical particle. The reason for this enhancement in the nanowire DEP force relative to the spherical particle is two fold: first, one of the dimensions of the nanowire (length) is larger than the spherical particle and second, the increase in the C.M. factor of the nanowire results in higher DEP forces. Moreover, the C.M. factor is a function of the aspect ratio and has a larger value for higher aspect ratios (smaller radii). The C.M. factor is also a function of relative polarizability of the particle to the liquid medium. The inset of Figure 3.1b shows the simulated values of the C.M. factor for a nanowire of length 5 μm and radius 50 nm for different values of nanowire resistivity over a range of frequencies. As the resistivity of the nanowire is reduced from 390 Ω.cm to 10 Ω.cm, the C.M. factor is increased by roughly 4×.

From these simulations, it is expected that the increase in the DEP force due to their anisotropic geometry makes it possible to trap individual nanowires with two dimensions in the nanoscale. We will explore this possibility experimentally in next sections.

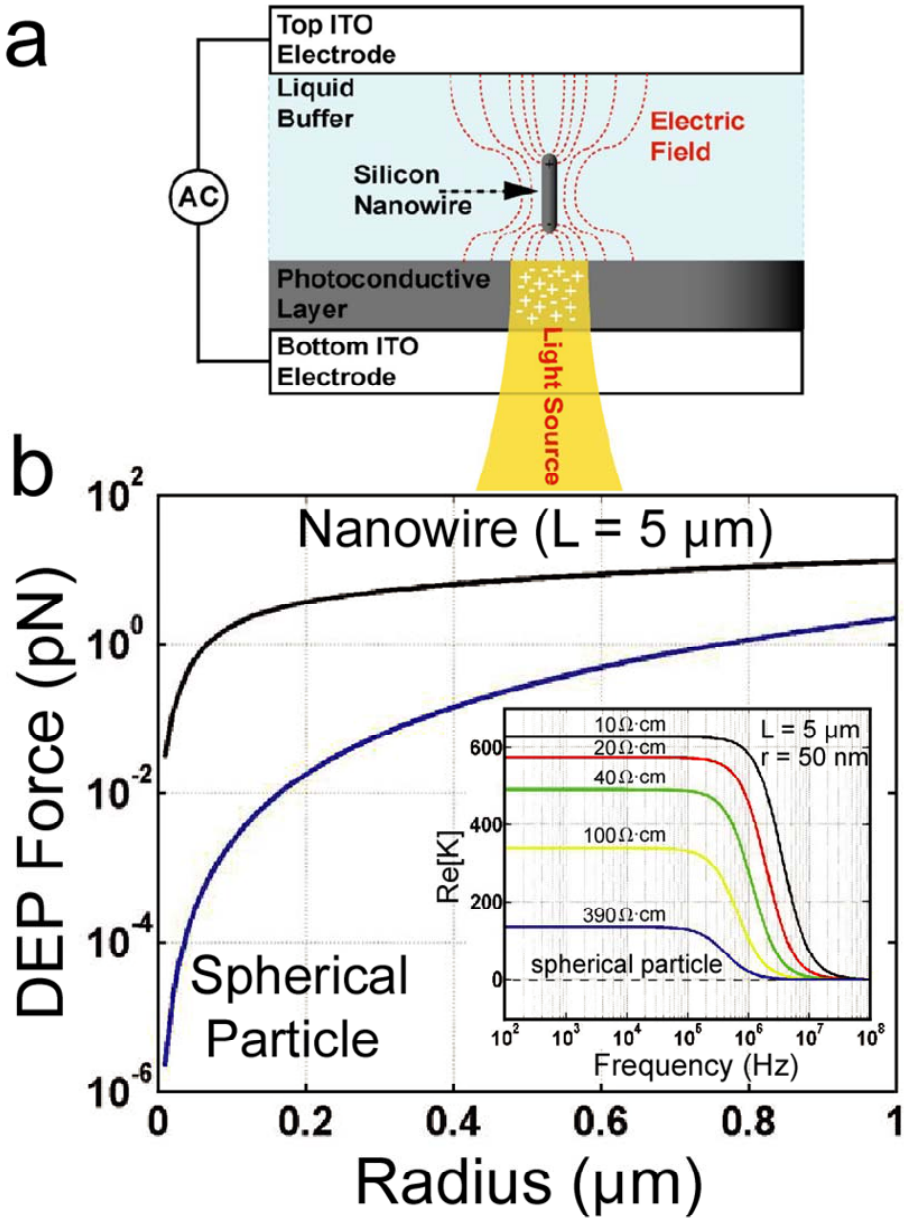

Figure 3.1 (a) Optoelectronic tweezers device structure with an individual nanowire trapped at the laser spot. (b) Comparison of the DEP force of a 5-μm-long nanowire and a spherical particle as a function of radius. The inset shows the calculated values of Clausius-Mossotti factor over a range of frequencies for different nanowire conductivities (for a nanowires with 5 μm length, and a 50 nm diameter).

3.2.2 Nanowire Samples

Before we move on to experimental trapping of nanowires, we will briefly describe the nanowire samples used in the experiments. Silicon nanowires were grown using the vapor-liquid solid (VLS) method through chemical vapor deposition of silicon tetrachloride ($SiCl_4$) onto a silicon wafer, which was gold coated by e-beam evaporation of Au, in a 850°C furnace for

approximately 30 minutes [108]. Figures 3.2a and 3.2b show the transmission electron microscopy (TEM) and scanning electron microscopy (SEM) images of the silicon nanowire samples.

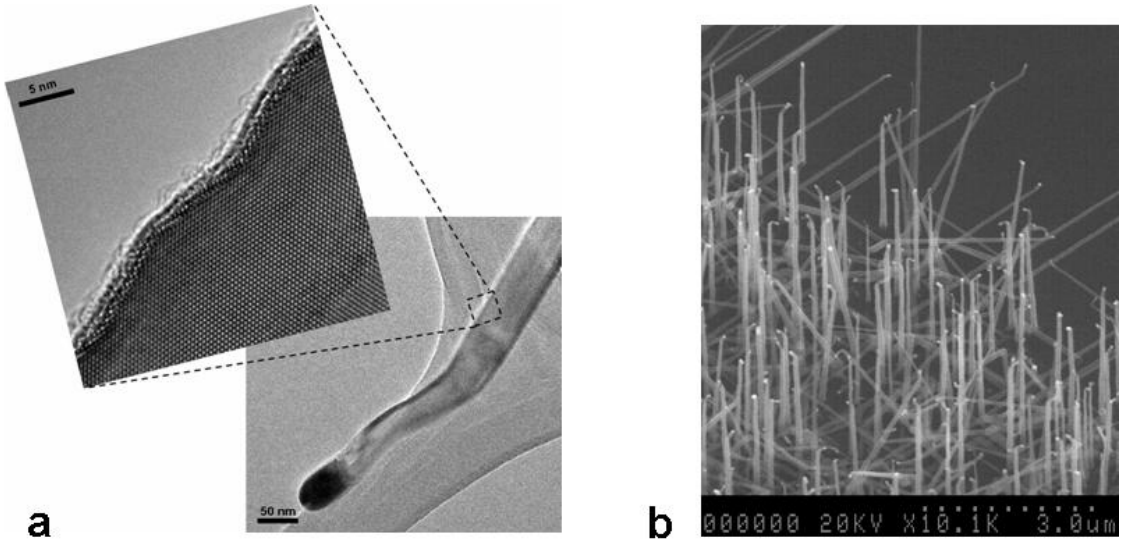

Figure 3.2 (a) Transmission electron microscopy (TEM) images of the silicon nanowire samples at 2.9K and 41K magnifications. (b) Scanning electron microscopy (SEM) images of silicon nanowire samples at 10.1K magnification.

The TEM images indicate that the nanowire samples do not have any noticeable gold catalyst residues on their surface. In addition, there is a thin layer of oxide, a few angstroms in size, on the surface of the nanowires. Using the SEM images, we can characterize the radius and length of the silicon nanowires. On average, the silicon nanowires have a radius of approximately 100 nm and length of approximately 5 μm. The change in the growth direction is due to cutting off the gas flow at the end of the growth process.

Another silicon nanowire sample used in certain experiments was prepared by etching a single crystalline silicon wafer followed by electroless metal deposition [109]. The ability to etch the nanowires out of a silicon wafer allows for preparation of nanowires with specific doping and orientations. Figures 3.3a and 3.3b show two TEM images of these nanowires.

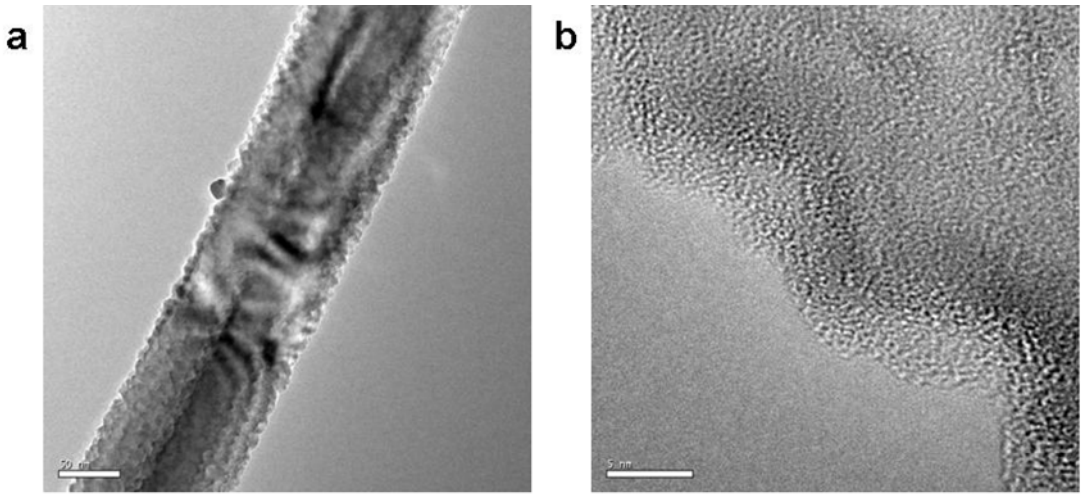

Figure 3.3 (a)-(b) Transmission electron microscopy images of etched silicon nanowire samples.

It is evident from the TEM images that the surfaces of these wires are rougher than the wires grown using the vapor-liquid-solid (VLS) method. The diameter and length of the wires are harder to control using this method, and are typically from 50-150 nm and 5-50 μm, respectively.

Silver nanowires used in the experiments were prepared using poly(vinyl pyrrolidone) (PVP) as the capping agent [110] and were found to have diameters of 80 to 100 nm, and lengths from 1 to 10 μm.

3.2.3 Manipulation of Individual Nanowires

To determine whether OET forces could address nanowires suspended in a fluid matrix, we transferred an aqueous suspension of silicon nanowires to a device chamber. Figures 3.4a-c show the process of trapping an individual silicon nanowire using a 633 nm HeNe laser (10 μm FWHM and 100 W/cm^2). In Figure 3.4a there is no voltage applied across the device and the nanowire undergoes Brownian motion. Once the voltage is applied (Figure 3.4b), the long axis of the nanowire aligns with the electric field in a fraction of a second, due to the torque experienced by elongated objects in electric fields, and the nanowire follows the laser trap as the beam is manually scanned across the stage (Figure 3.4c). Maximum trapping speeds for an individual silicon nanowire with 100 nm diameter and 5 μm length approach 135 μm/s with a peak-to-peak trapping voltage of 20Vpp. This is approximately 4 times the maximum speed achievable by optical tweezers [20] and is reached with five to six orders of magnitude less optical power density than optical tweezers.

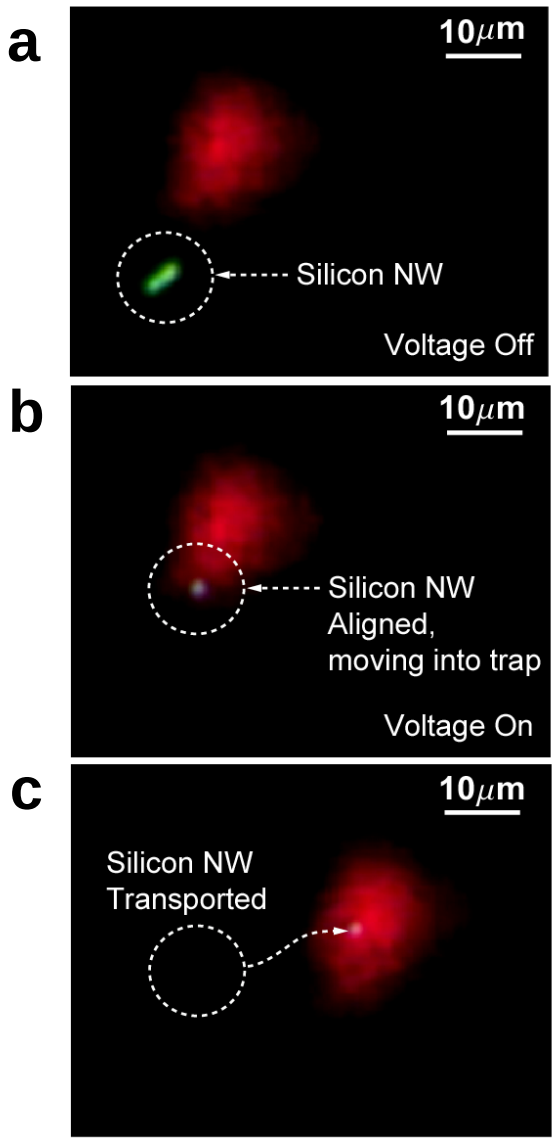

Figure 3.4 Trapping of an individual silicon nanowire using a laser spot. (a) No voltage is applied across the device, and the nanowire undergoes Brownian motion. (b) The voltage is applied, the long-axis of the nanowire aligns with the electric field and the nanowire moves into the trap. (c) The nanowire follows the laser trap position.

To characterize the OET trap, we can measure the trap stiffness as shown in Figure 3.5. The stiffness (k) is measured by measuring the relative displacement of the nanowire for negative and positive displacements for different translation speeds. The translation speed of the nanowires is used to calculate the DEP force (F_{DEP}) by equating the drag force to the DEP force, as discussed in section 2.4.2. By dividing the DEP force by the displacement, we can calculate the trap stiffness to be 0.16 pN/μm for a silicon nanowire with 100 nm diameter, 5 μm length and a maximum speed of 50 μm/s at 15 Vpp voltage. A 100 μW trapping source was used for measuring the trap stiffness which gives an OET trap stiffness figure-of-merit of 1.6×10^{-6} N/(m×mW), which is approximately two orders of magnitude larger than trap stiffness figure-of-

merit of optical tweezers [20]. Therefore, OET can achieve comparable trap stiffnesses to optical tweezers with 100× less optical power, resulting in a 100× larger figures of merit.

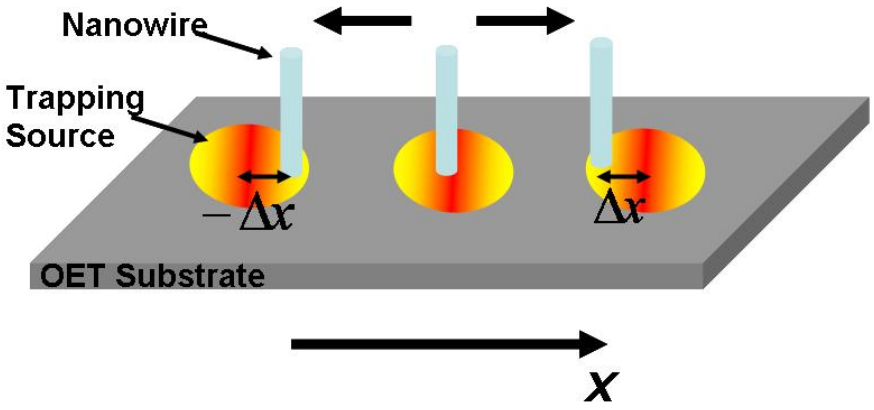

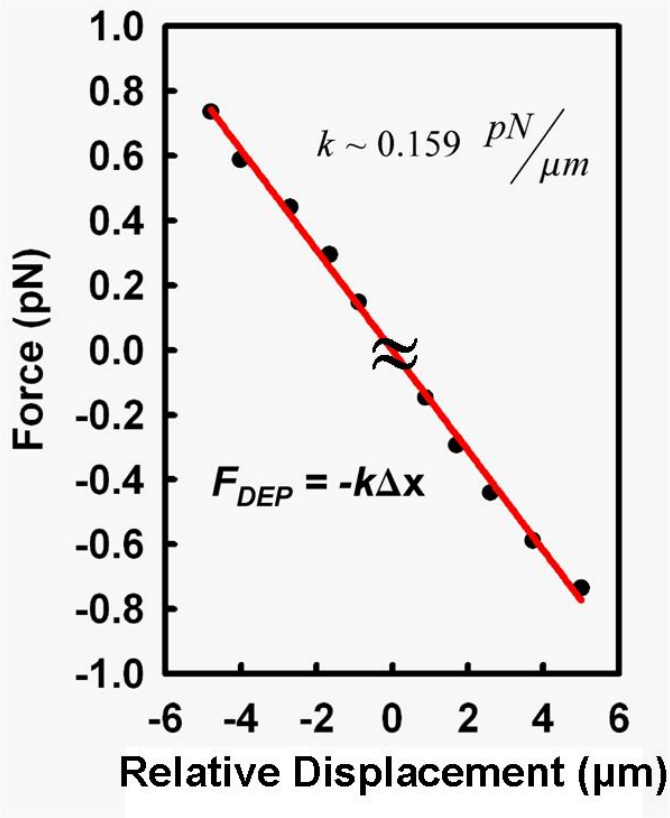

Figure 3.5 Measurement of the trap stiffness for a silicon nanowire. The trap stiffness for a silicon nanowire with 100 nm diameter and 5 μm length is measured to be ~0.16 pN/μm for an applied voltage of 15 Vpp and a maximum translation speed of 50 μm/s. For 100 μW trapping source, the OET trap stiffness figure-of-merit translates to 1.6×10^{-6} N/(m×mW).

As mentioned in Section 2.3, fundamentally, the size of the OET trapping potentials are diffraction-limited. However, Brownian motion displacement is inversely proportional to size of the particles, as shown in equation 2.22, and can play a more significant role in positioning accuracy of trapped objects as the size of the particle is reduced. To characterize the effect of Brownian motion in case of nanowires, we have used particle tracking image analysis [111]. Figure 3.6 shows the process of trapping a single silicon nanowire and the corresponding nanowire trajectory. A single silicon nanowire undergoes Brownian motion in the field of view, covering an area of 28.9 μm^2 (Figure 3.6d), once a trapping laser is positioned near the nanowire, it is attracted toward the laser (Figure 3.6c) and moved to a final location (Figure 3.6b). The nanowire is localized inside the trap to an area less than 0.22 μm^2 due to Brownian motion.

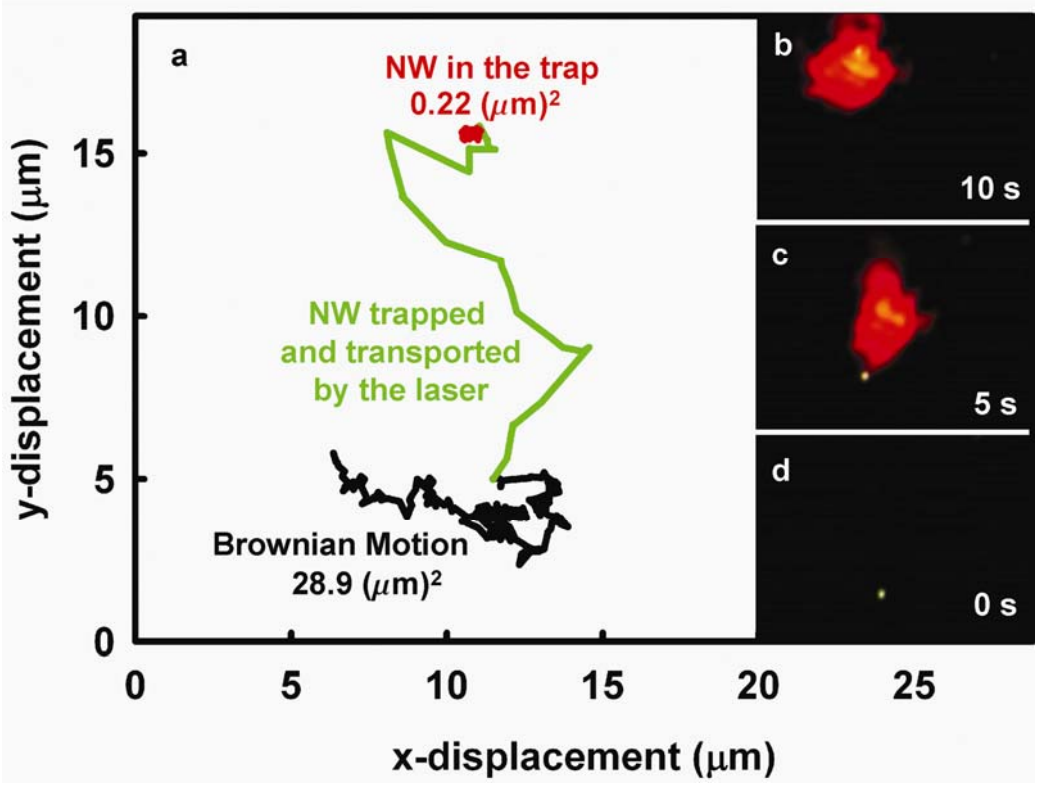

Figure 3.6 Manipulation trajectory of an individual silicon nanowire. (a) Measured trajectory of a single silicon nanowire. (b) while the nanowire is in the trap (spans an area of 0.22 μm^2). (c) as the nanowire is trapped by the laser trap and transported to a new location. (d) as the nanowire undergoes Brownian motion (spans an area of 28.9 μm^2).

In addition to trapping single nanowires, it is possible to trap multiple wires simultaneously in a given area, simply by adjustment of the optical spot's size (Figure 3.7).

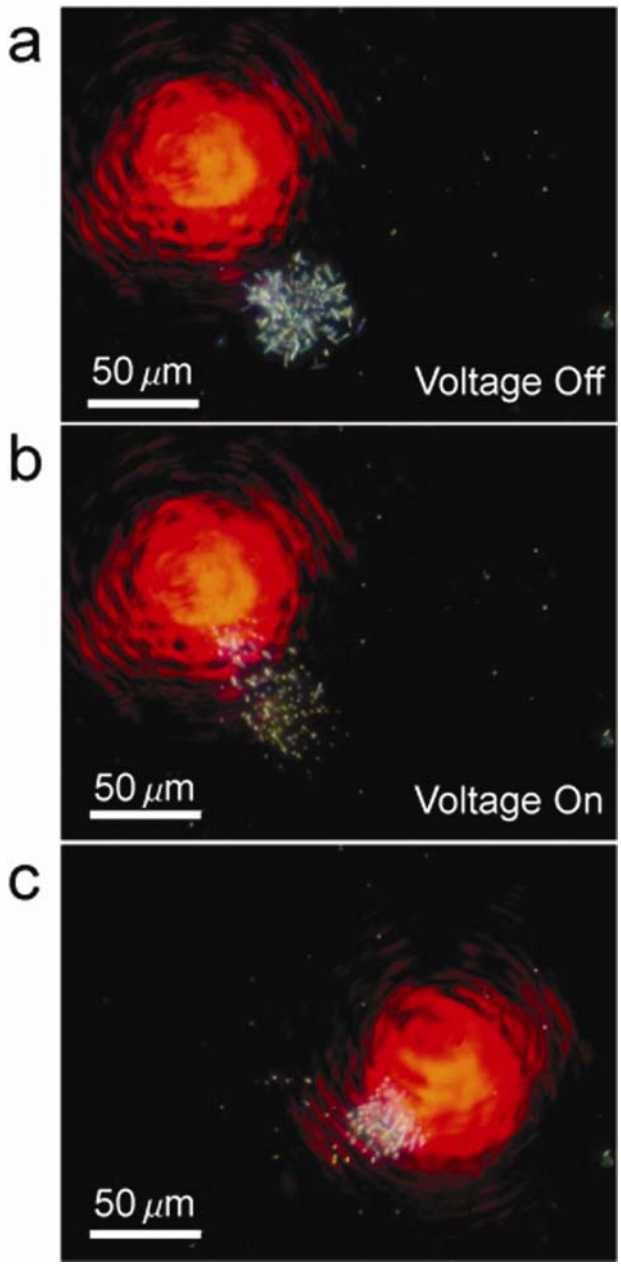

Figure 3.7 Collection of a large number of silicon nanowires. (a) There is no voltage applied to the OET device and nanowires undergo Brownian motion. (b) Once the voltage is applied the nanowires' long-axis aligns with the electric field simultaneously. (c) Nanowires follow the laser trap as it is scanned across the stage.

In addition to trapping semiconductor nanowires, OET is also capable of trapping and manipulating metallic (silver) nanowires. Prior experiments with a single-beam infrared laser trap has showed that high laser powers led to intense heating and scattering forces that prevented the optical trapping of silver nanowires [20]. Silver nanowires were found to show interesting OET trapping characteristics (Figure 3.8) due to their very high polarizability which forces them to align strongly with the electric field present in the liquid layer. Figure 3.8b,c show the process

of trapping three silver nanowires over a period of 4 seconds. It is interesting to note that the silver nanowires are trapped in the laser spot at an angle, as depicted in Figure 3.8a. The trapping angle, θ_m, of silver wires in the OET potential (Figure 3.8c) is measured to be approximately 74° using the relation

$$\theta_{\mathrm{m}} = \cos^{-1}\left(\frac{\mathrm{L_t}}{\mathrm{L_o}}\right) \tag{3.1}$$

where L_o equals the total length of the horizontal, non-trapped nanowire and L_t equals the observed length of the nanowires once they are in the trap. The silver nanowires are trapped in the region of highest electric field gradient and it is expected that they align to the electric field in that region due to their high polarizability. Using the simulated values for ∇E^2 (Figure 3.8a), we also calculate, θ_c, the angle of the electric field in high-∇E^2 region and find it to be approximately 64°, which is within 15% of the experimentally measured value.

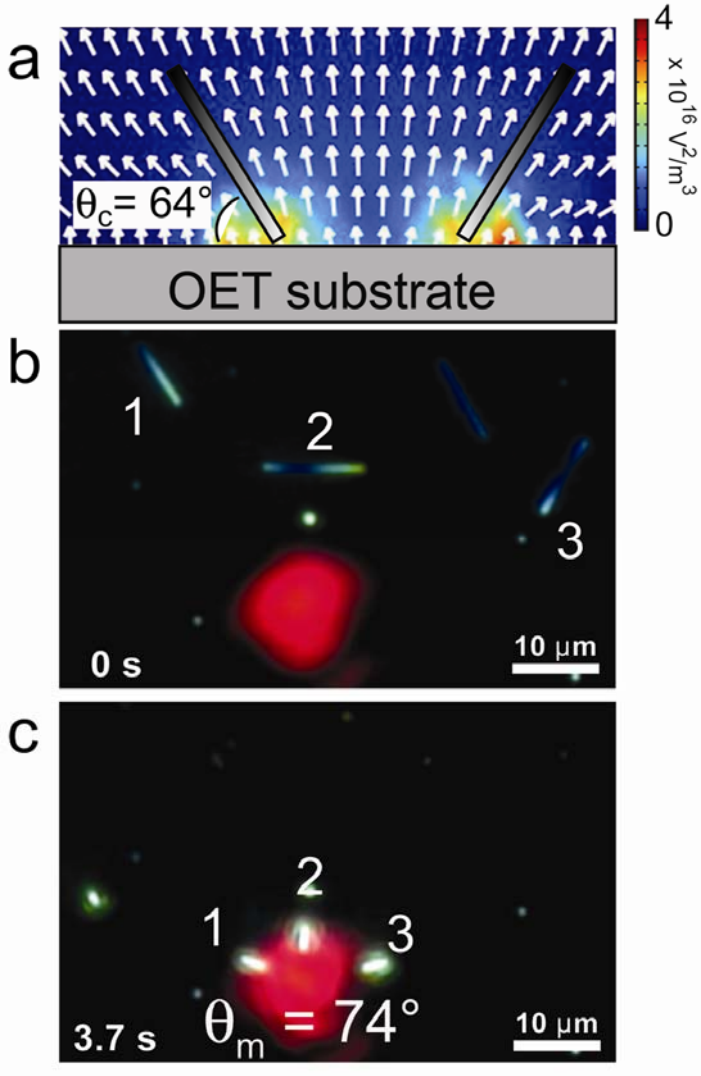

Figure 3.8 (a) Simulation of ∇E^2 (color plot) and the electric field (arrows) for a 50kHz, 8V peak-to-peak bias applied to the device. The electric field in the area of highest ∇E^2 (where the wires are trapped) is calculated to have an angle of θ_c = 64° with the OET surface. (b) No voltage is applied to the device, therefore the silver nanowires undergo Brownian motion and are not attracted to the laser spot. (c) Once the voltage is turned on the nanowires align with the electric field and are trapped in the laser spot at an angle of approximately θ_m = 74° which is within 15% of the calculated value.

3.2.4 Immobilization of Trapped Nanowires

The ability to preserve the position and orientation of OET-trapped nanowires is critical for enabling later post-processing steps, such as the deposition of metallic contacts. In this section, we will explore one possible way to achieve this for OET-trapped nanowires. Poly(ethylene glycol) diacrylate (PEGDA) is a UV-curable polymer [112, 113] that forms a three-dimensional polymer matrix in the presence of a UV source and a photoinitiator material (Figure 3.9). Exposure to UV illumination starts the polymerization process by creating free radicals from the

photoinitiator that attack the PEGDA molecules forming new free radicals and resulting in a chain reaction.

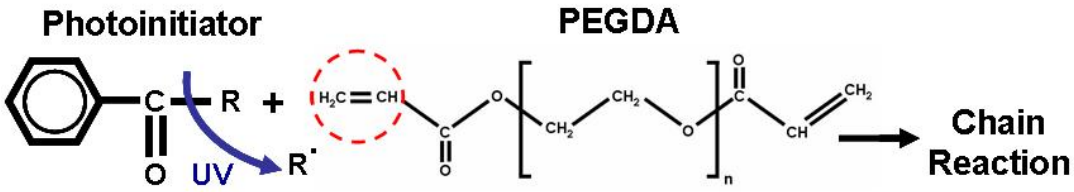

Figure 3.9 The process of PEGDA chain reaction is started using a photoinitiator. Exposure of the photoinitiator to UV source forms free radicals that attack the PEGDA, forming more free radicals, resulting in a chain reaction.

The transport and mechanical properties of PEGDA are customizable through adjusting the molecular weight and polymer percentage of the solution. In addition, high water content and tissue-like mechanical properties of PEGDA makes it a biocompatible material. PEGDA can be mixed with liquid solution containing the nanowires to enable immobilization of nanowires positioned at desired locations by exposure to a UV source. Figure 3.10 shows trapping and immobilization of a single silver nanowire in a PEGDA solution. The silver nanowires are dispersed in a solution containing 20% w/v PEGDA and 0.2% w/v photoinitiator (Irgacure 2959). After the solution is introduced into the OET chamber, the silver nanowires can be trapped and transported in the PEGDA solution. Once desired positioning is achieved, it is possible to freeze the nanowires in place in 3-4 seconds, by introducing a UV source (325 nm, 8 mW HeCd laser) from the top transparent ITO electrode and starting the polymerization process. Since PEGDA forms a three-dimensional matrix in the area that UV is present in such short time span, the orientation of the trapped wires is preserved in the immobilization process. One adverse effect of using PEGDA is that the presence of PEGDA increases the conductivity of the liquid approximately 6× the optimal liquid conductivity for nanowire manipulation which screens the polarizability of the nanowires, decreasing the DEP force that nanowires experience. In addition, PEGDA increases the viscosity of the solution, decreasing the translation speed of the nanowires further.

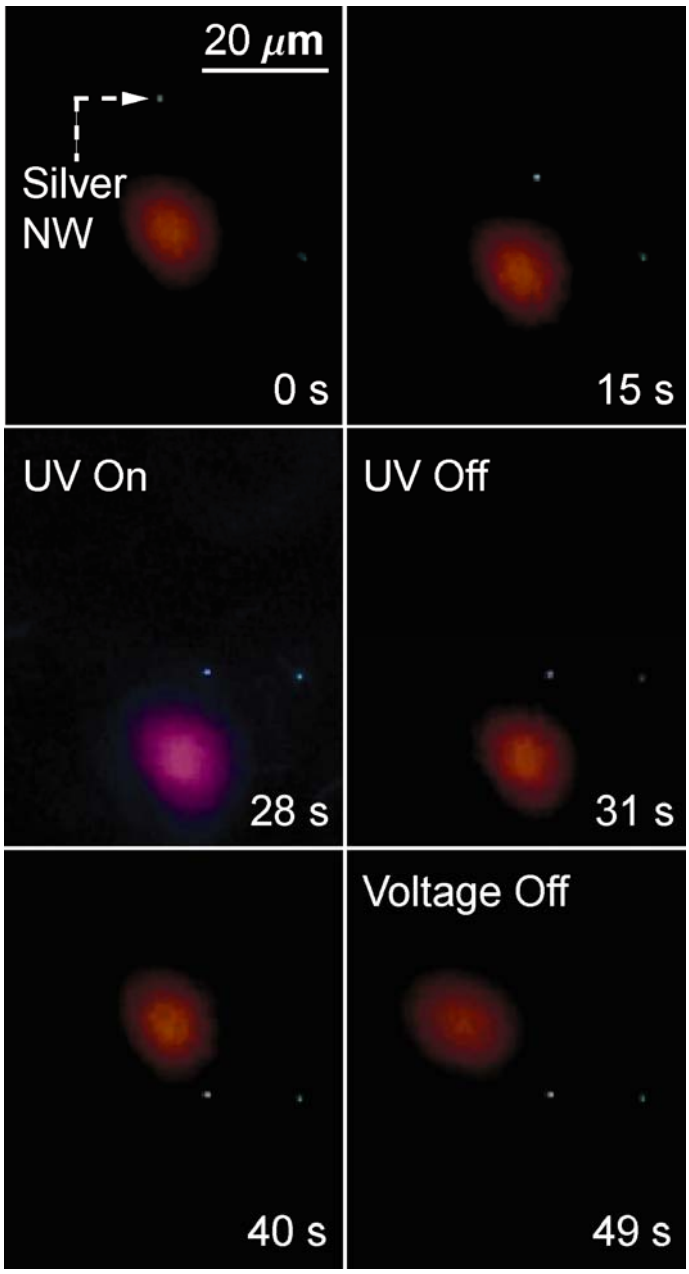

Figure 3.10 In-situ trapping and immobilization of an individual silver nanowire in a photocurable polymer matrix. A single silver nanowire is transported using OET in PEGDA photocurable polymer solution. Once the nanowire is positioned at the desired location, the manipulation area is exposed to a UV source (325 nm, 8 mW, HeCd laser), polymerizing the hydrogel solution and fixing the wire in place. After the polymerization the nanowire does not undergo Brownian motion and the laser trapping source is unable to move the nanowire. In addition, after turning off the AC potential, the nanowire's position and orientation are unaffected.

3.2.5 In-situ Raman Measurement of OET-trapped Nanowires

As mentioned before, OET optical manipulation setup can be integrated with other optical characterization techniques such as Raman spectroscopy. In-situ Raman spectroscopy has been used by other manipulation methods such as optical tweezers to study biological cells, micro and nanostructures [3,4]. However, OET's low required optical power density, large working area, and ability to massively manipulate cells in liquid buffer makes it highly biocompatible [1]. Therefore, OET-trapped nanostructures can be used for future non-invasive probing and imaging applications. In addition, in-situ Raman measurements of OET-trapped individual nanowires will be useful for sorting and separating nanowires of different compositions, sizes, surface functionalities, as well as for creating arrays of single nanowires of alternating properties.

Figure 3.11a shows the experimental setup for Raman measurements of trapped silicon nanowires. The liquid buffer containing the silicon nanowires (100 nm diameter, 10-20 μm in length) was introduced into the OET device. In this case, the same trapping laser (830 nm, 20 mW) has also been used for excitation of Raman signal. At first, no voltage was applied to the device and the nanowires were undergoing Brownian motion. Once the voltage was applied to the device, a single silicon nanowire was attracted to the laser spot. Upon trapping of the individual silicon nanowire, the silicon Raman peak was observed in the Raman spectra (Figure 3.11b). The Raman peak, approximately 520 cm^{-1}, agrees with typical reported values for silicon nanowires [5].

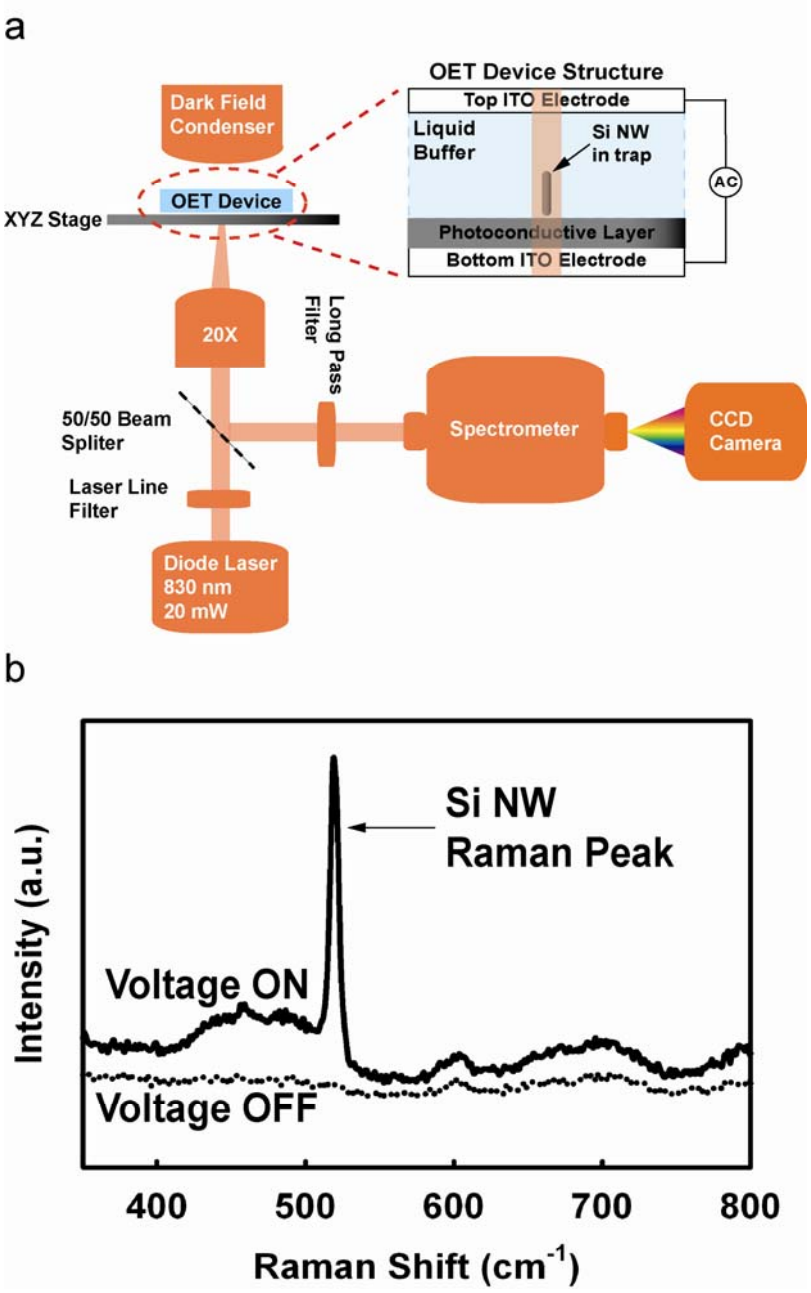

Figure 3.11 (a) Experimental setup for Raman measurement of an individual silicon nanowire: a diode laser (830 nm , 20 mW optical power) is focused onto the OET surface using a 20× objective. An AC voltage of 15 Vpp at 100 kHz is applied across the device. The Raman signal is collected using a spectrometer and a CCD camera. (b) No Raman signal was detected in the absence of an AC voltage (dotted line). Once the voltage was applied, an individual silicon nanowire was attracted to the laser and the silicon Raman peak was detected (solid line).

3.3 Separation of Semiconducting and Metallic Nanowires

As mentioned before, the strength of the DEP force depends on the relative permittivities and conductivities of the nanowire and suspension medium. Therefore, in the case of semiconducting (silicon) nanowires versus metallic (silver) nanowires, it is expected that the silver nanowires experience a larger DEP force due to their higher polarizabilities. Figure 3.12a shows the maximum trapping speeds achieved for individual silicon and silver nanowires for a range of peak-to-peak AC voltages. With an 8 V peak-to-peak AC bias applied across the OET device, the silver nanowires experience speeds up to 125 μm/s while remaining trapped, whereas silicon nanowires remain trapped only for speeds ≤ 2 μm/s. Thus, it is possible to separate silicon and silver nanowires by adjusting the scanning speed of the trapping laser while using a suitable peak-to-peak AC bias; so that the silver nanowires will be captured by the laser trap while silicon nanowires will be left behind. Figures 3.12b-d show the process of separating an individual silver nanowire from a silicon nanowire. The silver nanowire is aligned with the electric field even at 8 V peak-to-peak due to its high polarizablitliy, whereas the silicon nanowire is not aligned. A line laser is used to trap the silicon and silver nanowires (Figure 3.12b) and as the laser is scanned across the stage, the silicon nanowire is left behind whereas the silver nanowire stays with the trap (Figure 3.12d). In addition, control experiments were performed using silicon nanowires of comparable or larger lengths than the silver nanowires and the same separation effect was observed. We expect this approach to nanowire separations may also be extended to the separation of semiconducting and metallic carbon nanotubes. Despite the smaller cross sectional area of carbon nanotubes and the r^2 dependence of F_{DEP}, the increased aspect ratio and higher electrical conductivity of carbon nanotubes suggest OET as a promising direction for nanotube separations. We will explore the OET manipulation of carbon nanotubes in Chapter 4.

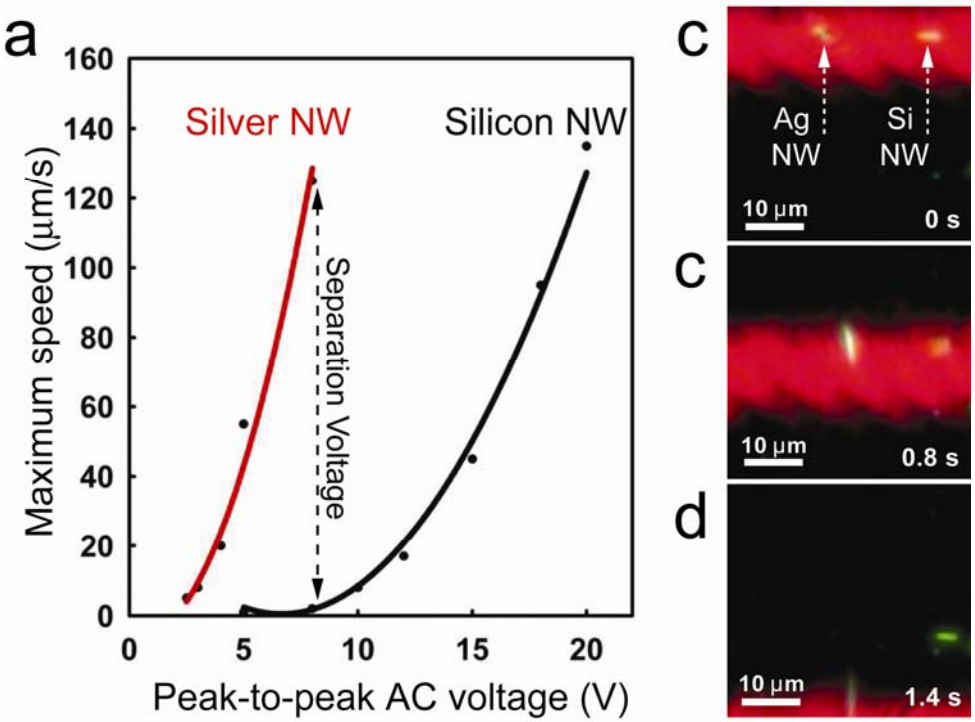

Figure 3.12 Separation process of an individual silver nanowire from an individual silicon nanowire by adjusting the scanning speed of a line laser. (a) Maximum experimental trapping speed for an individual silicon and silver nanowire over a range of peak-to-peak AC voltages. Due to the high polarizability of silver nanowires, at 8V peak-to-peak, the silver nanowires experience speeds up to 125 μm/s while silicon nanowires only experience speeds less than 2 μm/s. The solid lines in the plot are quadratic fits to the experimental data points. (b) Both silver and silicon nanowires rest in the stationary trapping potential. (c) The translation of the line potential begins the separation. (d) Scanning of the laser line with speeds greater than approximately 2 μm/s causes final separation of the silver and silicon nanowires.

3.4 Large-Scale Assembly of Nanowires

Recently there has been interest in vertically aligned nanowire arrays for solar energy conversion [114], thermoelectric cooling [115], and vertical field effect transistor [116] applications. One powerful aspect of OET is its ability to perform large-scale assembly of objects with a digital micromirror device (DMD) [57]. Figures 3.13a-b show examples of large-scale assembly of nanowires using real-time dynamic trapping. Figure 3.13a shows the formation of a 5×5 array of single silver nanowires which are individually addressable in real-time. Another approach to formation of large-scale arrays of nanowires is to use larger trapping patterns. Figure 3.13b shows the process of tuning the density of silver nanowires trapped by varying the size of a rectangular trapping pattern in real-time. It is interesting to note that when multiple wires are trapped in a single potential, they are observed to repel each other and fill the active trapping pattern due to dipole-dipole interactions. We will study this dipole-dipole interaction in detail in the next section.

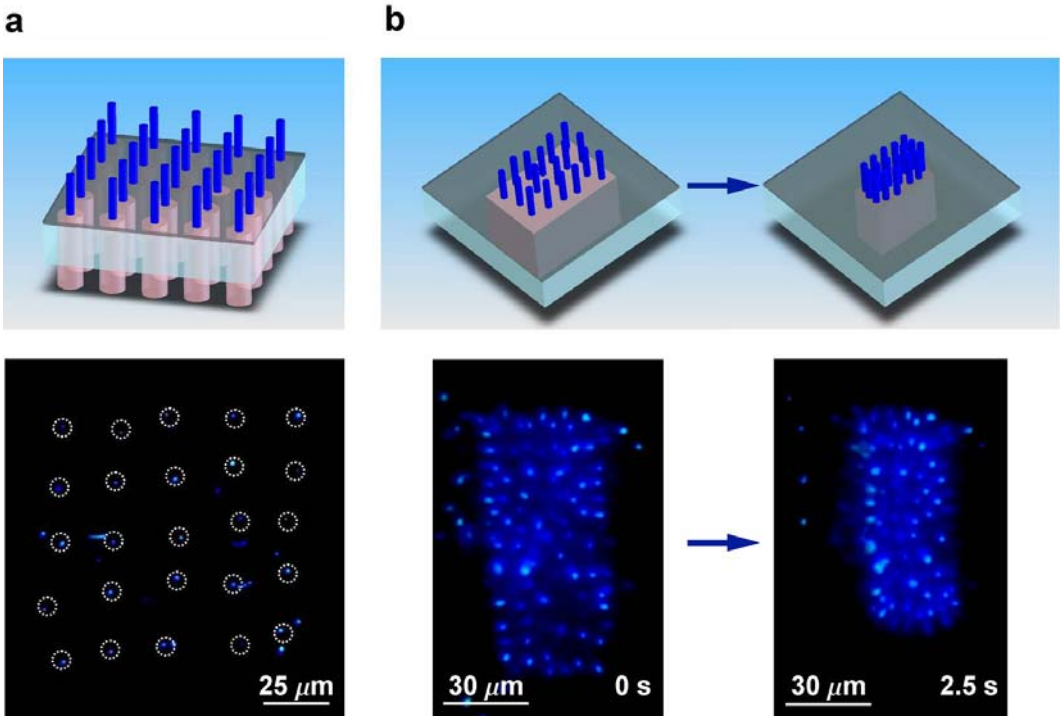

Figure 3.13 Large-scale manipulation of silver nanowires using traps created with a digital micromirror spatial light modulator and positioned with a computer-mouse-controlled GUI. (a) Formation of a 5×5 single silver nanowire array. (b) Large-scale control of nanowire density by adjusting the size of the trapping pattern. A collection of more than 80 Silver nanowires is concentrated from an area of approximately 3000 μm^2 to 2000 μm^2. The laser source is filtered out digitally in the images to aid pattern observation.

3.5 Dipole-Dipole Interactions between Nanowires

Metallic nanowires and nanorods have been used in a variety of novel applications such as multiplexed biodetection assays [117, 118], molecular sensing [119], nanophotonics [120-122], and nanomedicine [123] due to their interesting physical and chemical properties. Therefore, study and characterization of metallic nanowire and nanorod properties is essential to understanding their behavior in various applications. For example, hydrodynamic and electrokinetic characteristics of nanowires and nanorods, such as induced charge electroosmosis (ICEO) [124-128], have been extensively studied and characterized. As we mentioned in the previous section, another technique that greatly benefits from electrokinetic characterization of these nanostructures is dielectrophoresis [96] (DEP), which is the operational principle of OET. In the DEP technique, in addition to interacting with the non-uniform field, the induced dipoles on nanowires also interact among themselves. When the dipoles line up, they attract each other, creating a "pearl chaining" effect [96], which has been observed in both micro and nanoparticles [96, 129-132]. On the other hand, when the dipoles are parallel to each other, the particles will repel each other. This is a unique feature that can be used to produce self-assembled, equally-spaced nanoparticle arrays [133].

Figure 3.14 shows the OET device structure and major forces acting on two OET-trapped silver nanowires. As mentioned previously, the nanowires experience a positive DEP force (F_{OET}) and are trapped in the OET-induced potential. However, the induced dipoles of each nanowire are parallel to each other, resulting in a net repulsive force (F_{dipole}) on each nanowire from the aligned dipoles. This repulsive force repels the nanowires from each other and pushes them away from the OET trap. Therefore, the nanowires are positioned at the balance-point between the DEP force and the dipole-dipole repulsive force.

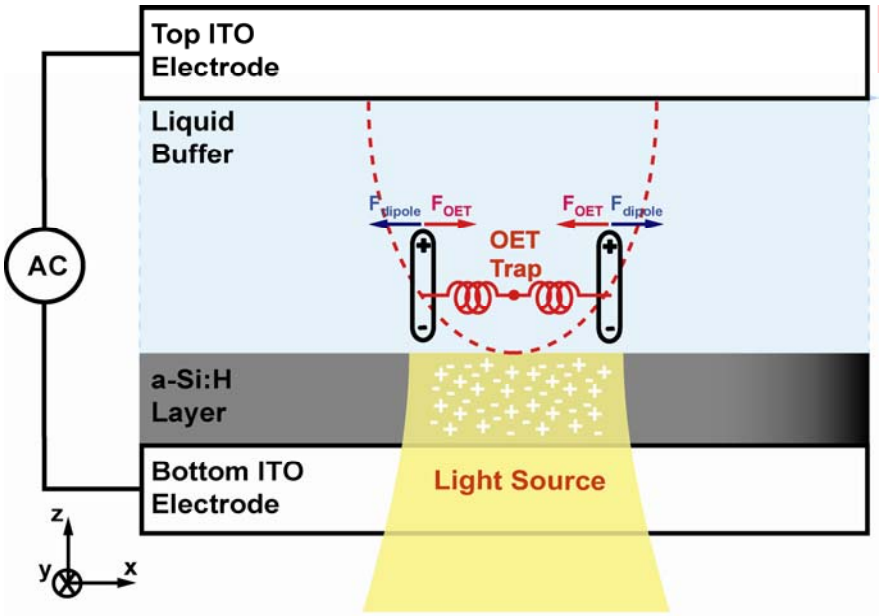

Figure 3.14 Optoelectronic tweezers (OET) device structure for study of dipole-dipole interaction between two silver nanowires. The nanowires are pulled towards the trap by the DEP force (F_{OET}) and are pushed away from the trap by the dipole-dipole repulsive force (F_{dipole}). Once the laser source is removed, the nanowires are no longer held together by the DEP force and are pushed away from the trap, until the dipole-dipole repulsive force cannot overcome the Brownian motion.

To study the dipole-dipole interactions between nanowires, a 3-µL solution of silver nanowires was introduced into the OET device chamber. The silver nanowires, grown using aqueous reduction of silver ions [110], with 7 µm average length and 50-80 nm diameter were dispersed in a 1:1 ethanol and KCl / deionized water solution with 1-5 mS/m conductivity. A 635-nm diode laser with a measured power of 100 µW at the OET surface was used to trap the silver nanowires. AC voltages of 5-8 Vpp at 50-100 kHz were applied to the OET device.

Figure 3.15a shows two silver nanowires trapped in the laser spot. Once the laser is turned off, the nanowires are no longer confined by the DEP force ($F_{DEP} = 0$), and are pushed away from the trap by the repulsive dipole-dipole force. The trajectories of the nanowires, shown in Figure 3.15b, were extracted using a Matlab-based particle tracking software. The nanowires are displaced by an average distance of ~3±0.6 µm along the x-direction due to the repulsive dipole-dipole force. Since the dipole-dipole force falls off rapidly with the distance between the nanowires, the maximum net repulsive force on one wire can be calculated by measuring the maximum nanowire displacement per unit of time, immediately after the trapping source is

removed. Figure 3.15c shows the x-displacement of the two nanowires in Figure 3.15a versus time. The nanowires experience a maximum repulsive speed of approximately 5.5±1 μm/s immediately after removing the trap. To estimate the repulsive force magnitude, we can calculate the drag force acting on the nanowire and equate the dipole-dipole interaction force (F_{dipole}) to the drag force which results in a maximum F_{dipole} on the nanowires of approximately 0.1±0.02 pN.

A similar repulsive response is observed for four OET-trapped nanowires as depicted in Figure 3.15d, the extracted trajectories of the nanowires are overlaid on the 4 seconds frame. The average displacement of the four nanowires due to dipole-dipole force is approximately 10±0.8 μm.

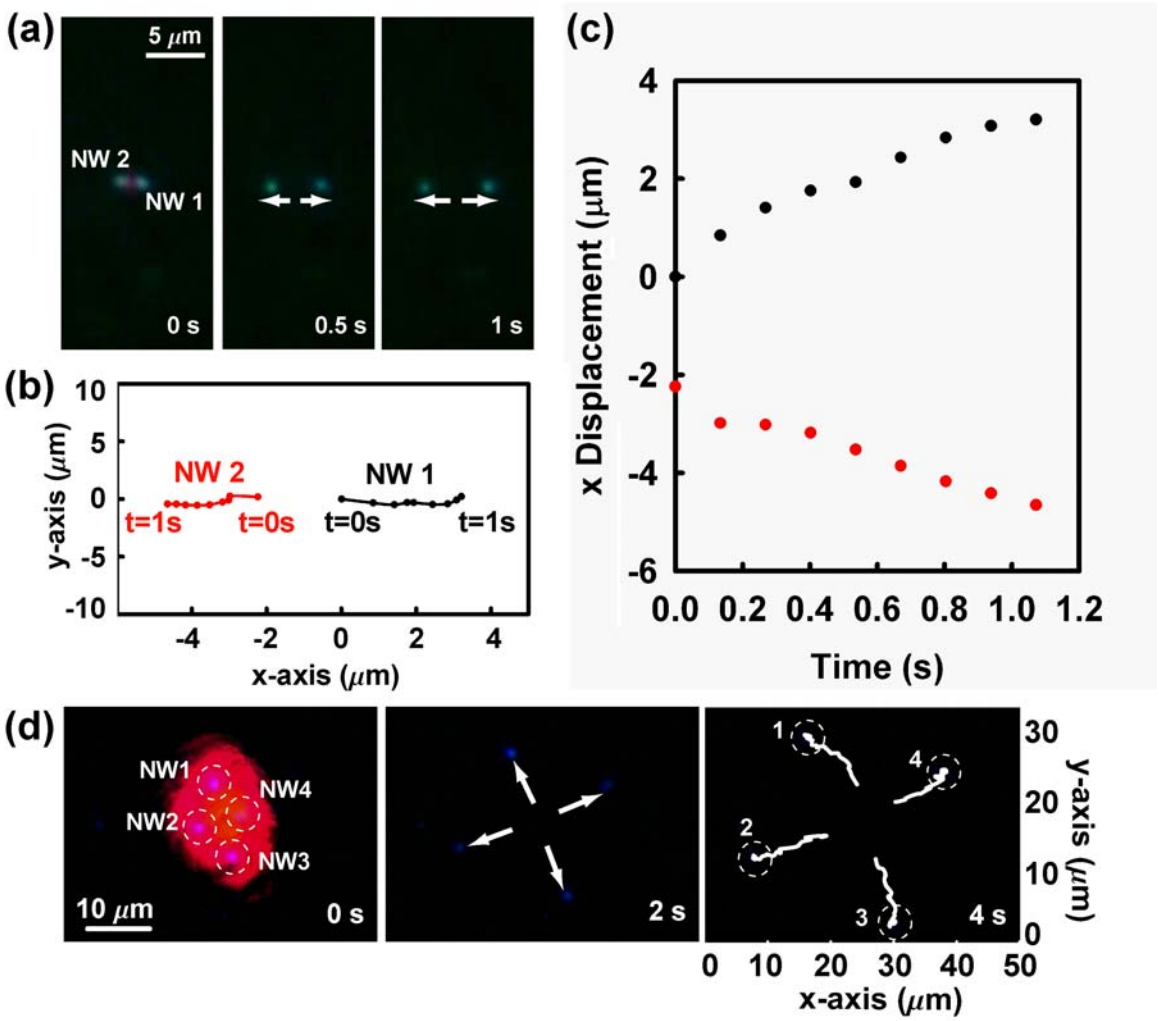

Figure 3.15 (a) The process of dipole-dipole repulsion between two OET-trapped nanowires (2.2 μm apart). In the beginning the nanowires are trapped. Once the laser trap is removed the nanowires repel each other. The time stamps indicate the time elapsed since the laser removal. (b) The trajectory of the two nanowires. The initial position of nanowires1 is used as the origin. (c) The x-displacement of the two nanowires versus time due to dipole-dipole repulsion. The magnitude of the dipole-dipole repulsive force (F_{dipole}) can be calculated by measuring the initial speed of the nanowires immediately after the trap removal which is 5.5±1 μm/s. This speed corresponds to a force of F_{dipole} = 0.11±0.02 pN. (d) The dipole-dipole repulsion process for four OET-trapped NWs. The white trajectories on the 4s frame indicate the extracted trajectories of four nanowires after removing the OET trap.

Another interesting aspect of the dipole-dipole interaction is that multiple nanowires confined in the same OET trap will spontaneously assemble into patterns with the lowest potential energy. This is observed experimentally, where two nanowires trapped by OET form a line, three nanowires form an equilateral triangle, four nanowires form a square, and five nanowires form a pentagonal structure (Figure 3.16a-d). These regular nanowire patterns present stable arrangements with the lowest possible potential energy. Figure 3.16e-g shows the process

of adding a nanowire to the two nanowire structure to make a triangle. In the beginning there are two nanowires in the trap forming a line (NWs 2,3) and a third nanowire (NW1) is attracted to the OET trap from the bottom of the screen. Once NW1 reaches a distance of ~4.4 μm from NW3, the dipole-dipole repulsive force of the two nanowires pushes them in the opposite direction and self-organizes the three nanowires in the form of a rectangle.

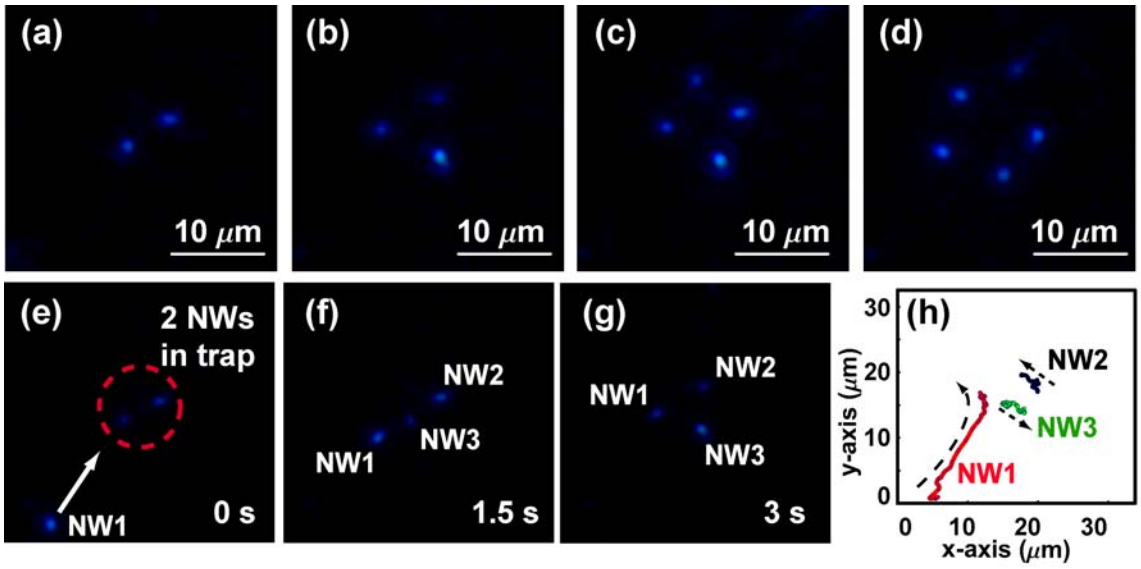

Figure 3.16 Formation of smallest possible energy systems by nanowires trapped using OET. Formation of (a) a line for two nanowires trapped (b) an equilateral triangle for three nanowires trapped (c) a square for four nanowires trapped, and (d) a pentagonal structure for five nanowires trapped. The trapping laser source is filtered out in the images. (e-g) show the process of addition of a nanowire to the two nanowire ensemble. (e) NW1 is attracted to the OET trap from the bottom of the screen. (f) Once NW1 reaches a distance ~4.4μm from NW3, (g) it pushes NW3 to the side and three NWs re-assemble to form a triangle structure in the trap. (h) trajectories of the three nanowires. The arrows indicate the direction of the nanowires motion.

3.6 Assembly of Nanowires using Lateral Field OET (LOET)

As we have seen in previous sections, in addition to the DEP force, the nanowires experience a torque which aligns their long-axis with the electric field. In the conventional OET device, the field lines are perpendicular to the bottom and top surfaces. Therefore, elongated particles are manipulated perpendicular to the device surface. Though this feature is desirable in forming highly aligned nanowire arrays, as discussed in Section 3.4, for many applications such as fabrication of electronic and optoelectronic devices, it is desirable to manipulate and position nanowires in a lateral fashion. A new version of the OET device called lateral-field optoelectronic tweezers (LOET) [71] has been developed to enable lateral manipulation of objects. Figure 3.17 compares the device structure for conventional OET and lateral-field OET (LOET). LOET is able to dynamically manipulate objects laterally by patterning the bottom a-Si:H surface in the form of interdigitated electrodes and applying an AC bias between the electrodes. This results in electric field lines in parallel with the manipulation plane and simplifies the assembly process.

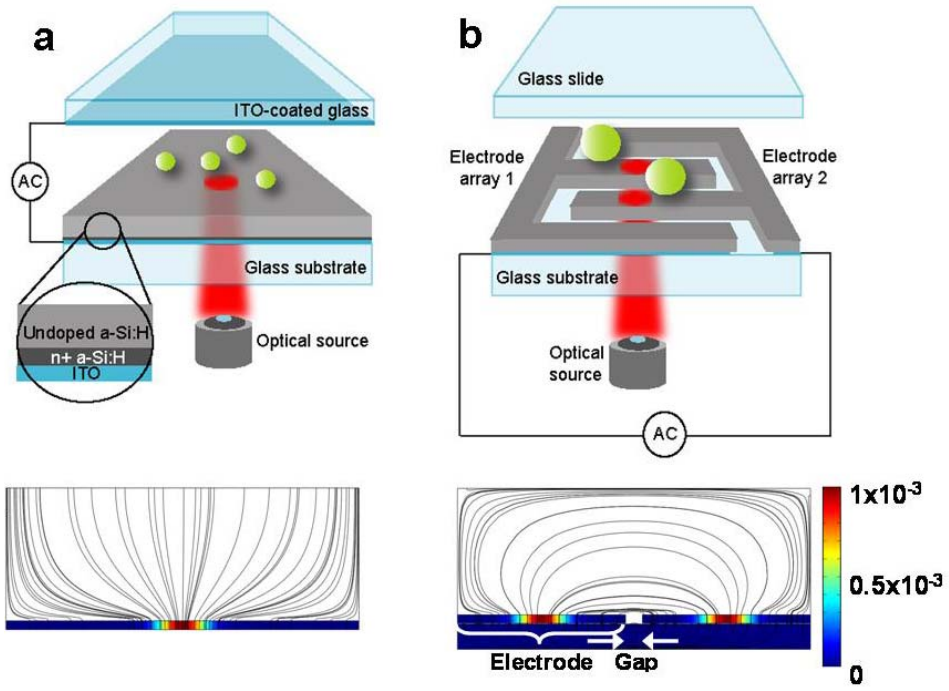

Figure 3.17 (a) Conventional and (b) Lateral-field OET device structures and simulated electric field lines for each case. (© Optical Society of America [76])

Figure 3.18a-d shows the process of trapping and translation of a single silicon nanowire using LOET with an applied voltage of 5 Vpp at 50 kHz. In the beginning there is no voltage applied to the device and the nanowire is undergoing Brownian motion. Once the AC voltage is applied, the nanowire is attracted to the laser spot and can be translated. The long-axis of the wire remains aligned with the lateral electric fields created between the interdigitated electrodes.

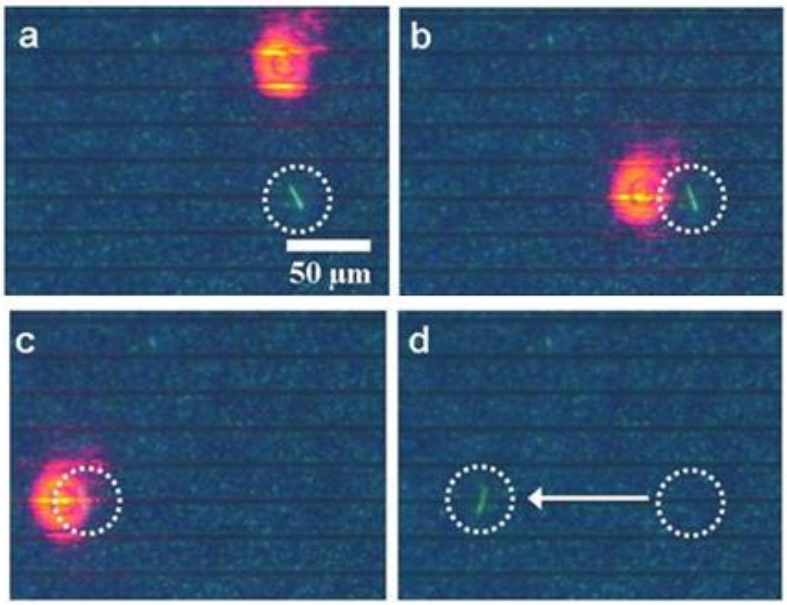

Figure 3.18 Trapping and transport of a single silicon nanowire using lateral optoelectronic tweezers (LOET). (© Optical Society of America [76])

One application of LOET assembly has been demonstrated in formation of RGB pixels for low power display applications for a variety of devices including cell phones. Current display technologies such as liquid crystal displays (LCDs) and organic light emitting diodes (OLED) suffer from poor efficiencies (5-10%) or short lifetimes, respectively. Therefore, semiconductor nanowire LEDs offer an attractive alternative due to their long lifetime and low-cost synthesis. However, the main challenge in using nanowires is to find methods capable of heterogeneous integration of nanowires with different materials. As discussed previously, OET presents an optofluidic method for addressing this challenge. To assemble an RGB pixel, CdSe (λ = 685nm), ZnO (λ = 518nm), and CdS (λ = 496nm) nanowires have been used for red, green, and blue pixels, respectively. Figure 3.19a-c shows the excitation of each nanowire with a UV light source (HeCd, 325 nm, 8 mW). Figure 3.19d shows the dark field image of the nanowire array assembled using a variation of LOET [75, 77]. These results show that LOET can be used as a tool to manipulate nanowires and heterogeneously integrate them into an array. Potentially, the nanowire array can be directly assembled on CMOS circuit drivers for a full colour display.

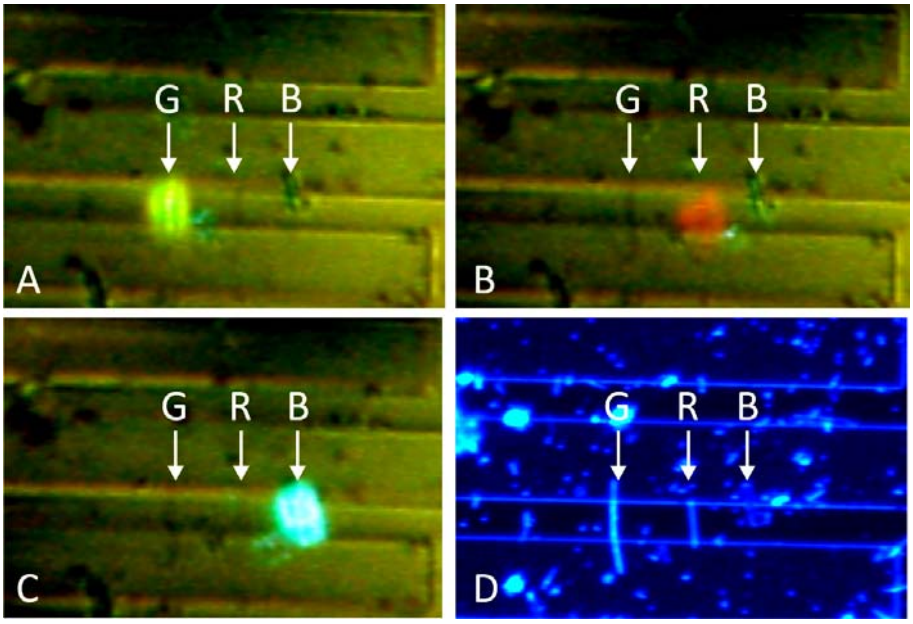

Figure 3.19 (a) to (c) show the ZnO, CdSe and CdS nanowires being illuminated successively by the UV laser. These images show that the photoluminescence from these nanowires is of different wavelength and can hence be used as a RGB pixel. (d) shows a dark field image of the nanowire array. (© Optical Society of America [75])

3.7 Summary

In its present form, OET offers real-time, parallel, and high-speed manipulation for a broad range of one-dimensional materials, enabling dynamic positioning, assembly, and rapid separation of semiconducting and metallic nanowires. However, many challenges remain before OET becomes viable for large-scale nanowire integration. Manipulation is restricted to the 2D surface coated by a photoconductive thin film, limiting the construction of 3D heterostructures. Additionally, wires are observed to adhere to the samples surface through non-specific binding which limits the ease of manipulation. Though, it has been demonstrated recently that nanowire surface functionalization is an effective tool to control interactions between nanowires and surfaces [134] and these methods can potentially be used to reduce the nanowire adhesion.

Chapter 4 Manipulation of Multi-walled and Single-walled Carbon Nanotubes

4.1 Motivation

Over the past two decades single- wall and multi-wall carbon nanotubes have been employed in myriad applications including desalination membranes [135], chemical sensors [136], additives for high-strength polymer composites [137], field emitters [138], and integrated circuits [8, 139]. Although an impressive degree of control has been achieved for carbon nanotube synthesis [140], currently few optical method exists for freely trapping and translating individual nanotubes in solution, with contemporary approaches typically relying on either dielectrophoresis (DEP) or single-beam laser tweezers. However, OET is particularly well suited for trapping of carbon nanotubes since it can combine the massive parallelism of DEP with the optical flexibility of laser tweezers by using optical intensities low enough to minimize detrimental effects due to optical absorption. In this chapter, we will explore the use of OET for manipulation of multi-wall and single-wall carbon nanotube samples with potential applications in separation of semiconducting and metallic nanowires and device fabrication.

4.2 Preparation of Carbon Nanotube Samples

There are two main challenges in handling samples of carbon nanotubes in aqueous solutions. First is the tendency of carbon nanotubes to form bundles in solution and second is the difficulty in observation of carbon nanotubes due to their extremely small size. In this section, we will discuss and characterize the carbon nanotube samples used for manipulation experiments.

4.2.1 Multi-wall Carbon Nanotubes (MWCNT)

To prevent carbon nanotube samples from bundling in solution, they are typically mixed with a surfactant solution [141]. The hydrophobic end of surfactant molecules attaches to the hydrophobic surface of carbon nanotubes, leaving the hydrophilic end of surfactant molecules on the surface interacting with the solution, and therefore solubalizing the sample. MWCNTs were purchased from SES Solutions and dispersed in water (Millipore) with a surfactant (sodium dodecylbenzenesulfonate or SDBS) at a mass ratio of 5:1 surfactant:MWCNTs, sonicated for 30 min, and then centrifuged for 10 min at 16,000 g yielding a semitransparent solution. The initial loading of MWCNTs in solution typically is on the order of 0.1 mg/mL, and final solution conductivities can be varied between 1-100 mS/m. Typical MWCNTs have diameters and lengths ranging between 10 – 80 nm and 0.3 - 6 μm, respectively, with an average diameter of 38 nm measured from scanning electron microscopy (Figure 4.1).

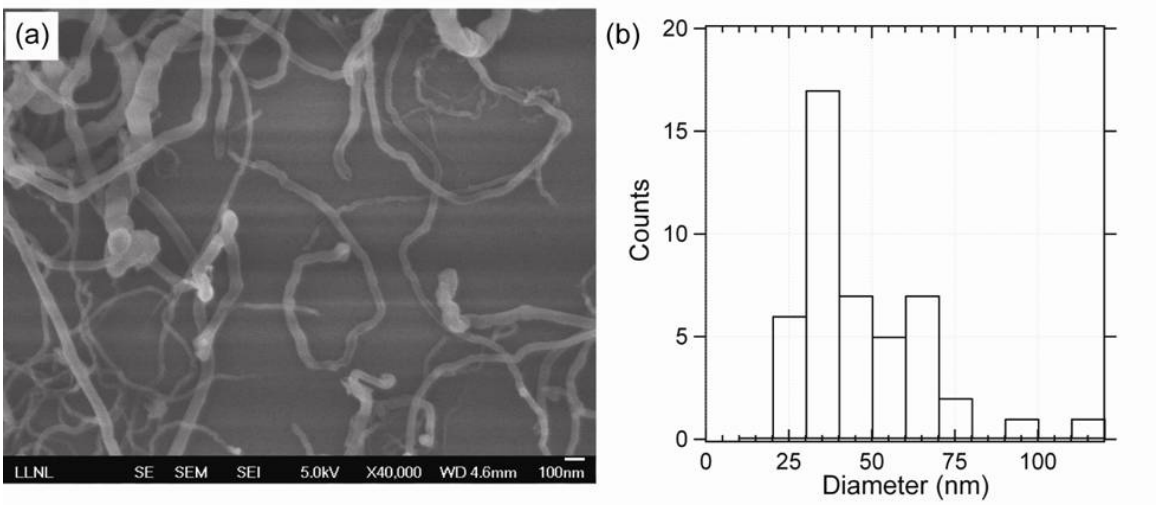

Figure 4.1 Diameter distribution of MWCNTs (a) SEM of MWCNTs imaged within an OET chamber following a typical OET trapping experiment (b) Histogram of MWCNT diameters from (a) with an average diameter of 38 nm. (© American Institute of Physics [78])

Figure 4.2 shows transmission electron micrograph of a multi-wall carbon nanotube with a hollow core.

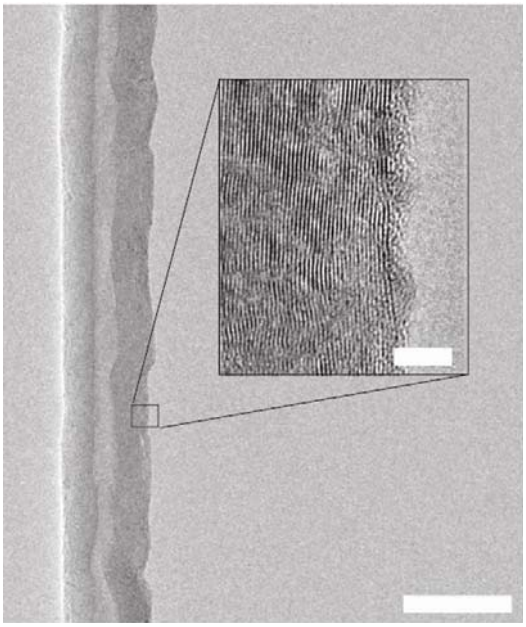

Figure 4.2 Transmission electron microscopy image of a multi-wall carbon nanotube with hollow core. Scale bar - 100 nm. Inset shows individual graphite layers of the tube Scale bar - 5 nm. (© American Institute of Physics [78])

4.2.2 Single-wall Carbon Nanotubes (SWCNT)

COOH-functionalized carbon nanotubes have been used as a surfactant-free alternative for aqueous SWCNT suspensions, with the hydrophilic COOH-surface functional groups serving as a means to suspend the nanotubes on polar solvents such as water [142]. COOH-functionalized SWCNTs (P3, Carbon Solutions, Inc., ~4 atomic % COOH-functionalization) were dispersed as-made in Milli-Q deionized water, bath-sonicated for 30 min, and centrifuged for 30 min at 16,000 g to remove large bundles and other metallic catalyst particles yielding a semitransparent solution. Transmission electron microscopy and atomic force microscopy can be used to characterize the physical dimensions for the nanotube bundles, with diameters ranging from 2 to 11 nm, and lengths ranging from 0.1 to 2 μm (Figure 4.3a,b), with a mean bundle diameter of 6.4 ± 2.4 nm. We assume the bundles consist of a mixture of semiconducting and metallic tubes, with the dielectric properties of the metallic tubes dominating the overall dielectric response of the bundles.

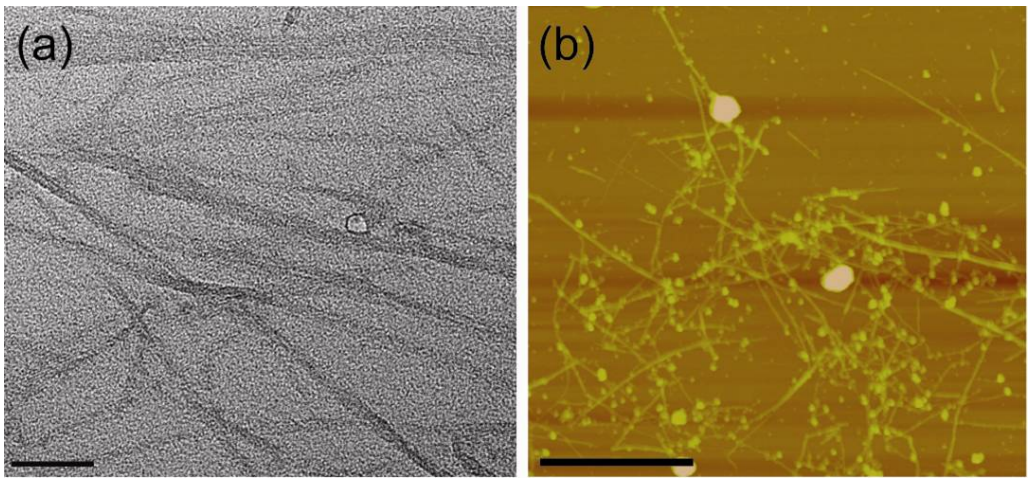

Figure 4.3 Characterization of COOH-functionalized SWCNTs (a) Bright field transmission electron micrograph. Scale bar - 50 nm. (b) Atomic force micrograph of SWCNTs on an aminoproylesilane coated mica wafer. Scalebar - 1μm.

4.3 Manipulation of an Individual Multi-wall Carbon Nanotube

Several methods have been used to overcome the challenge of observing carbon nanotubes in solution. Single nanotube imaging employing either fluorescent labels [143] or intrinsic SWCNT photoluminescence [144] has been used recently to measure translational and rotational diffusion coefficient for individual SWCNT structures. Individual MWCNTs can also be observed without fluorescent labeling due to their large Rayleigh scattering cross section using dark-field microscopy and either a color or electron-multiplying CCD [145]. Figure 4.4a shows the schematic of a multi-wall carbon nanotube in the OET chamber. A large (80 nm diameter) multi-walled carbon nanofiber is shown in Figure 4.4b, representing the upper bound of the MWCNT size used here. In solution, MWCNTs undergo Brownian motion before the trapping voltage is applied to the chamber (Figure 4.4b). Once the trapping voltage is applied to the OET device, the MWCNTs experience a torque aligning them with the electric field (Figure 4.4c) and a positive DEP force causing them to translate towards the OET laser trap (Figure 4.4d), analogous to what we discussed for nanowires.

The MWCNT is observed to follow the laser trap as it translates throughout the OET device. We can use a particle tracking software to extract the motion of the tube from video frames [111]. Discrete translation events are labeled in Figure 4.4e by a Roman numeral with an arrow indicating the direction of motion. Circled regions indicate where the laser trap was brought to momentary rest. For the first MWCNT translation, the laser is stationary and the MWCNT moves into the trap after the AC field is applied across the ITO electrodes. The trap is then translated by hand through a diamond shaped course filling a region of approximately 100 μm^2 before it is brought to rest. When the trapping spot is stationary, the MWCNT is confined to a region less than 1 μm^2 (Figure 4.4e, inset) while continuing to undergo Brownian motion.

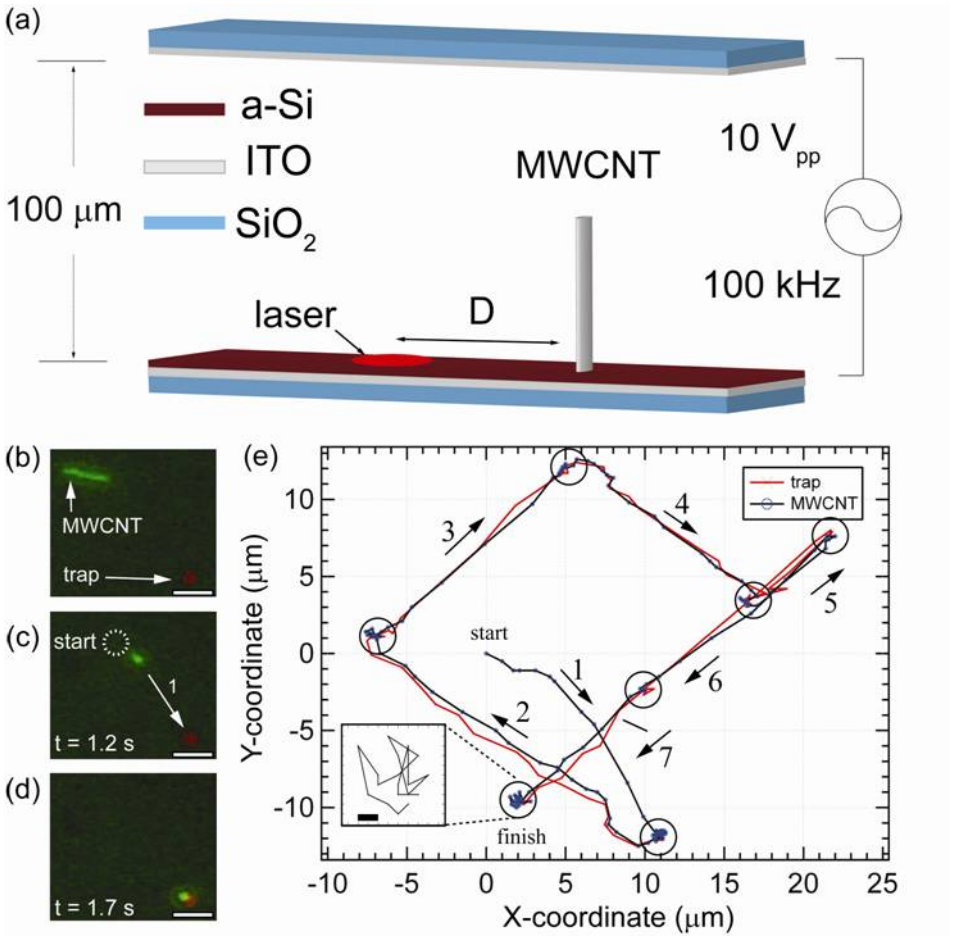

Figure 4.4 (a) OET chamber schematic. (b) Dark field image of an isolated MWCNT in Brownian motion. Scale bar - 5 μm. (c) Alignment and initial translation of the MWCNT following 10Vpp, 100 kHz field applied to chamber. (d) Translation over ~15 μm of the MWCNT into the OET trap. (e) X-Y coordinates of MWCNT and trapping laser measured from video frames. Circles indicate locations where trapping laser was temporarily static. Inset: Coordinates of trapped MWCNT in static laser at finish. Scale bar - 200 nm. (© American Institute of Physics [78])

The respective position coordinates for the MWCNT and trapping laser spot can be analyzed further to gain information on the absolute speed of the MWCNT and trap, as well as their relative separation. Figure 4.5a shows the instantaneous speeds for both the MWCNT and trapping laser over the course of approximately 20 seconds while Figure 4.5b shows their relative separation. During trace 1 (when the laser velocity is zero), the tube velocity exceeds 30 μm/s as it translates into the trapping laser. The trap is then translated through traces 2 – 7, and the MWCNT's velocity is observed to respond after each translation event.

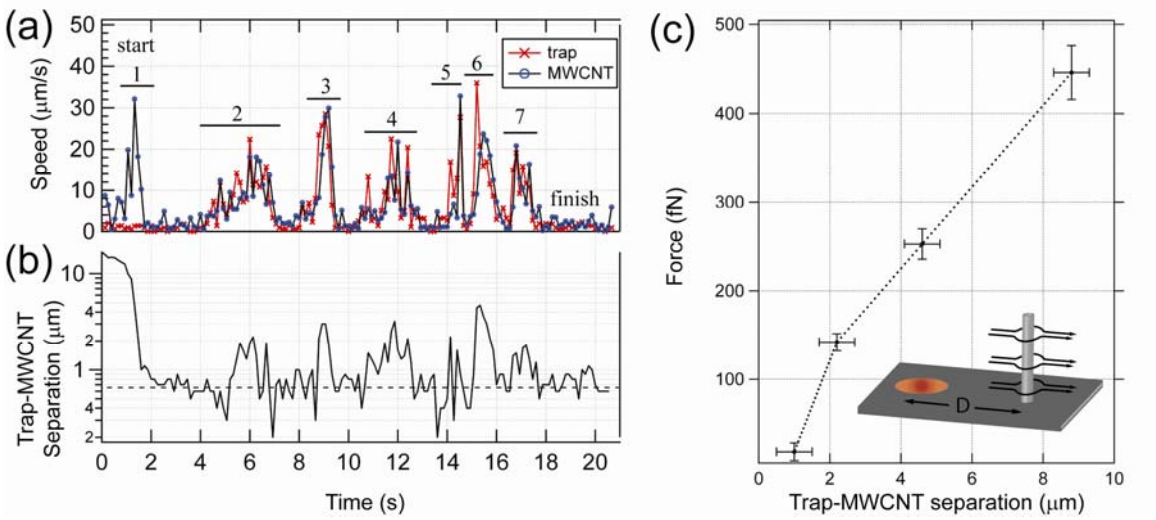

Figure 4.5 (a) Absolute speed and (b) absolute separation of MWCNT and laser during the course of the trapping measurement in Figure 4.4. (c) Trapping stiffness measurement from force on MWCNT measured from Stokes drag exerted by the trapping laser during trace 1 in Fig. 4.4. Inset: schematic of fluid flow around MWCNT. (© American Institute of Physics [78])

Inertial forces are negligible in the trap as a consequence of the extremely small Reynolds number that exists at the operating conditions of this device (Re ~ 10^{-6}). Therefore, MWCNT motion is dominated by a competition between OET forces, Brownian motion, and viscous drag. Due to their large aspect ratios and the variable shape of their end-facts, we model the MWCNTs as elongated, prolate-ellipsoids, as discussed in Section 2.4.2. By neglecting end-facet dissipation, this calculation provides a conservative lower-bound measure of applied forces that are approximately 10% lower than for a circular cylinder [146] with an equivalent aspect ratio. In Figure 4.5c the calculated force as a function of absolute MWCNT-trap separation is plotted using the measured MWCNT length of ~6 μm and the upper-bound diameter of 80 nm for the sample of MWCNTs. This results in an approximately linear response as the MWCNT moves into the stationary laser trap over a distance of ~10 μm. A linear fit to this region of data reveals an approximate trap stiffness of 50 fN/μm. Additional experiments with a motorized translation stage (Newport) have shown MWCNTs to move with speeds of 235 ± 29 μm/s, which is in agreement with calculated trapping forces on the order of pico-Newtons.

Many post-synthetic processing techniques such as selective surface binding [147], inkjet printing [148], or microcontact stamps [149] operate on large ensembles of nanotubes. Consequently, parallel MWCNT processing with OET requires investigation of the case when multiple MWCNTs are trapped simultaneously in a virtual electrode. Figure 4.6a,b shows dark-field images of the two MWCNTs trapped together in a common virtual electrode, as well as the MWCNTs in Brownian motion after the trapping voltage is turned off (Figure 4.6c). The Brownian motion of the tubes shown in Figure 4.6d differs significantly from that of a single trapped MWCNT (Figure 4.4e, inset) in that the pair of tubes are not free to move across the OET virtual electrode, but rather occupy separate sides due to mutual repulsion from in-phase induced dipole moments, as discussed for nanowires in Section 3.5. Figure 4.6e shows the

histogram of tube-tube separation with the mean separation of the tubes measured to be roughly 3 μm, consistent with the size of the trapping spot.

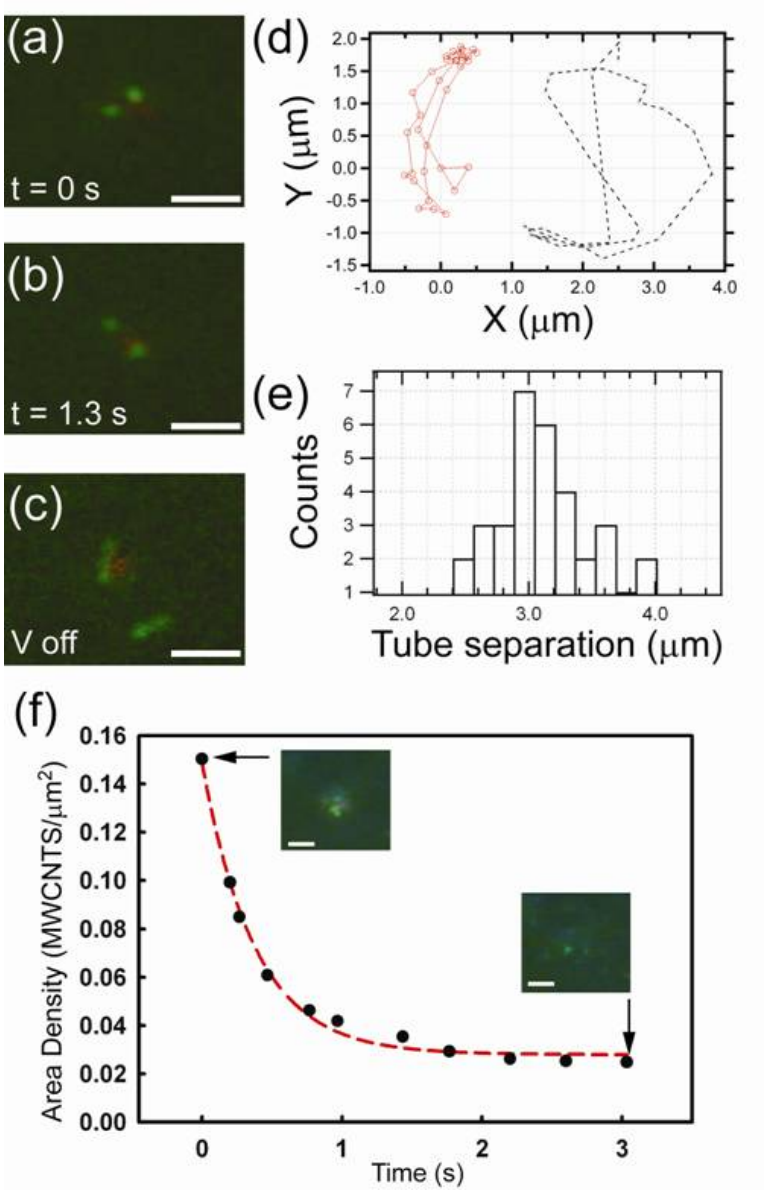

Figure 4.6 (a-b) Dark-field microscope images of two MWCNTs trapped in a single OET virtual electrode at different times with voltage on. Scale bar - 5μm. (c) Corresponding MWCNTs with voltage off. (d) The Brownian motion trajectory of the tubes inside the trap, occupying separate sides of the trap from dipole-dipole interaction. (e) Histogram of tube-tube separation. (f) Number density of >15 MWCNTs in a ~10 μm OET trapping spot before and after trapping laser is turned off. Insets show dark-field images corresponding to when the OET laser is on an off. Scale bar - 5 μm. (© American Institute of Physics [78])

This observed mutual dipole-dipole repulsion can be used for modulating the number density of MWCNTs in the OET device simply by actuating the virtual electrode. In Figure 4.6f, measurements are made on the number density of >15 MWCNTs in a ~10 μm OET trapping spot. By turning on the trapping spot, all tubes are collected in the virtual electrode, with a number density of approximately 0.2 MWCNTs/μm^2. When the laser is removed, the tubes experience an immediate dipole-induced repulsion, with an exponentially decaying number density that reaches a baseline value of 0.02 MWCNTs/μm^2 in approximately 3 seconds. This number density is still two orders of magnitude below what has been achieved with high-density MWCNT synthesis [135] but represents a rapid optical method for locally tuning the density of MWCNTs over an order of magnitude.

4.4 Manipulation of Bundles of Single-wall Carbon Nanotubes

In this section, we will explore the OET manipulation of single-wall carbon nanotubes. Observation of single-wall carbon nanotubes is more challenging than multi-wall samples, due to their small dimensions. However, dark-field optical microscopy can be used [145] to image aqueous suspensions of SWCNT bundles with a video-rate EMCCD (Andor, iXon). When a 15Vpp, 100kHz trapping voltage is applied across the OET chamber the SWCNTs are observed to move away from one another (Figure 4.7a) due to repulsive, in-phase dipole-dipole interactions. When the trapping laser is turned on (488 nm, 100 μW) SWCNT bundles are observed to migrate into the laser spot (Figure 4.7b), agreeing with previous reports of positive dielectrophoresis forces for metallic SWCNTs [26].

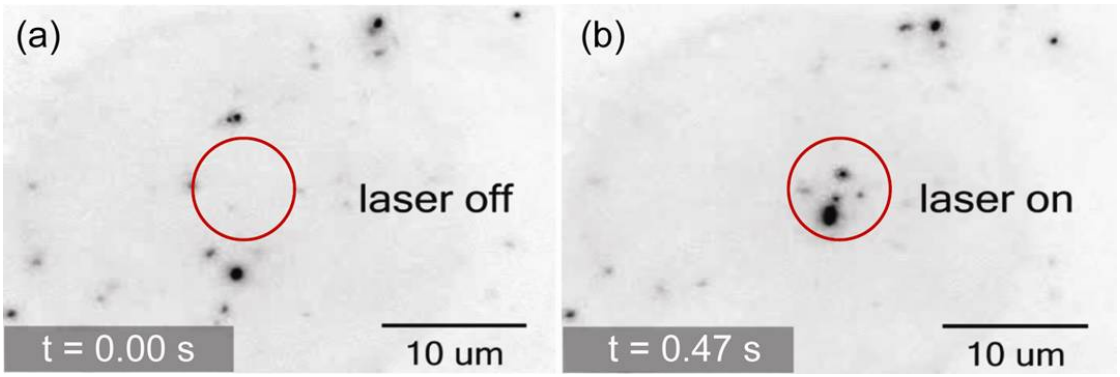

Figure 4.7 Dark-field EMCCD video microscopy of optoelectronic trapping of COOH-SWCNTs with laser off (a) and on (b) at an AC bias of 15Vpp, 100kHz. Images are inverted to enhance visibility of faint light scattering of SWCNT bundles. The laser line (Ar^+, 488 nm) is blocked by a holographic notch filter.

Even though dark-field microscopy can be used for observation of single-wall carbon nanotubes bundles, it is difficult to confirm trapping of smaller bundles or single tubes optically. Therefore, high trapping voltages (20 Vpp, 100kHz) the SWCNTs were used to attract and attach the trapped objects irreversibly to the a-Si:H surface. Electron beam lithography was used to pattern a grid of metallic fiducial markers (20 nm Ti, 50 nm Au) on top of the polished a-Si:H layer which are then used to locate regions on the OET surface following Raman deposition experiments. Using SEM of deposited structures next to an e-beam fiducial (Figure 4.8a) and

Raman spectroscopy (Figure 4.8b) for *ex situ* characterization, we are able to confirm that the deposited structures are indeed SWCNT bundles.

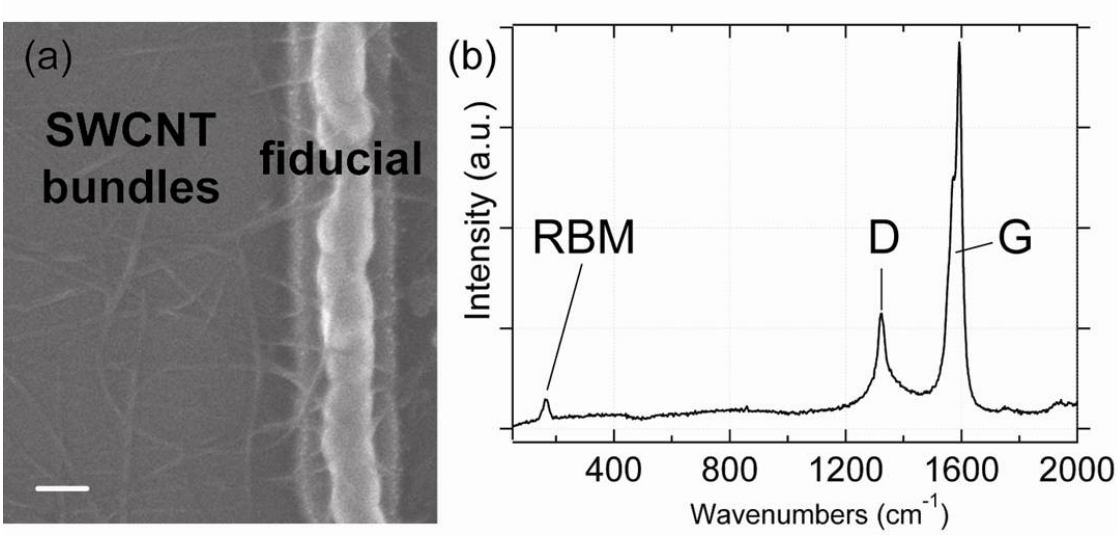

Figure 4.8 *ex situ* characterization of COOH-SWCNTs following deposition with optoelectronic tweezers at high peak-to-peak voltages. (a) SEM image of SWCNT bundles deposited next to a Ti/Au fiducial marker. Scalebar - 100 nm. (b) Raman spectrum of deposited SWCNT bundles showing radial breathing mode (RBM), D, and G bands; a-Si:H background subtracted.

Single beam laser tweezers [17] have been used previously for three-dimensional trapping [150, 151], and Raman characterization [152] of SWCNT suspensions, however, they typically require several milliwatts of power to produce electric field gradients sufficient for trapping. Confocal Raman measurements may also be performed with OET in an upright backscattering configuration. Generally, several hundred μW from the polarized 632.8 nm line of a CW He:Ne laser (Figure 4.9a) are focused to an area of ~75 μm^2, yielding a maximum local irradiance of <500W/cm^2 which is more than sufficient to actuate the OET virtual trapping electrodes while simultaneously providing enough inelastically scattered photons for Raman spectroscopy. The focal point is positioned in the chamber with a motorized translation stage, using the Raman signal of the a-Si:H as a means of ensuring that the Raman focal volume coincides directly with the OET-trapping volume.

When Raman spectra are taken from the COOH-SWCNT dispersions, signal levels are low due to both the low concentration of tubes in solution as well as defects within the carbon lattice that decrease the inelastic scattering cross section [153]. Raman spectra are acquired both with and without the OET trapping voltage (6 Vpp, 100 kHz) at both the a-Si/fluid interface (Figure 4.9a) and ~20μm above the a-Si. Once the trapping voltage is applied the in-plane asymmetric E_{2g} stretching mode at 1591 cm^{-1} collected from the a-Si/fluid interface shows an 18-fold increase based on a ratio of integrated 1591 cm^{-1} peak areas. The enhancement exists both when compared to the case with the trapping voltage off, and with the voltage on, but with the focus ~20 μm above the a-Si surface (Figure 4.9b). The signal enhancement is reversible, depending only on whether the laser is present to generate inhomogeneous lateral electric trapping fields.

When the AC-voltage is turned off, the signal relaxes to the background level, suggesting that trapped SWCNTs become free to diffuse through solution in agreement with dark-field images.

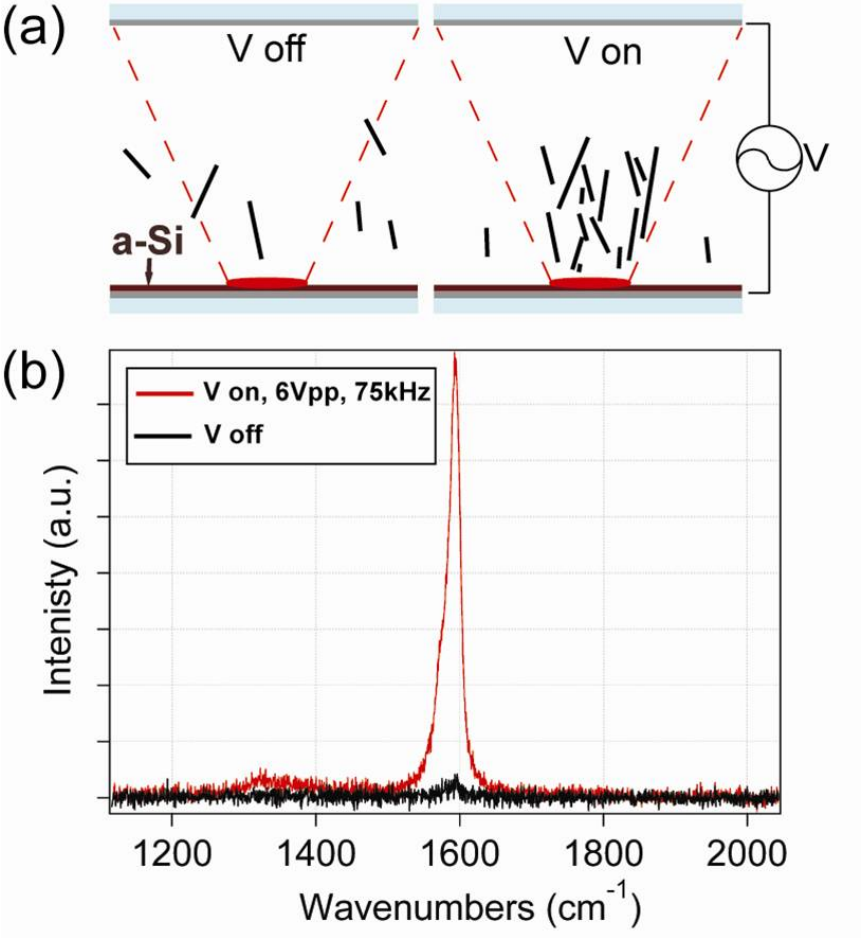

Figure 4.9 Enhanced Raman signal from COOH-SWCNTs trapped with OET (a) Schematic of Raman experiment. (b) Raman spectrum with (red) and without (black) OET trapping bias of 6Vpp, 75kHz.

This signal enrichment can potentially be combined with other Raman enhancement techniques such as surface-enhanced Raman spectroscopy (SERS) to create more sensitive Raman probes. OET is unique in that low laser intensities can be used to enrich the local analyte concentration while simultaneously producing inelastically scattered photons for sample characterization.

Finally, characterization of single-wall nanotubes trapping characteristics is an important step towards separation of tubes according to their material properties. Despite numerous demonstrations of superior physical properties [154] (such as ballistic electron transport and ultra-high mechanical strength), the practical use of carbon nanotubes has been frustrated by one simple yet crucial limitation—the challenge of growing purely semiconducting or metallic material [155]. In particular, roughly 30% of all tubes for a given synthesis (such as pulsed laser ablation and chemical vapor deposition) are metallic due to how the electronic band structure is affected by the random way graphite sheets may roll to make a tube. The resulting heterogeneity

is an intrinsic barrier that has seriously hindered the widespread application of carbon nanotubes. For example, transistors and photodetectors require semiconducting components and the metallic fraction in a heterogeneous carbon nanotube sample contaminates the device, greatly limiting the performance of the resulting circuitry.

To achieve separation between metallic and semiconducting nanotubes, one of their differing physical properties such as density, conductivity, or chemical reactivity has to be exploited. Many techniques have been used to address this challenge, dielectrophoresis with lithographically patterned electrodes has been used to demonstrate an enrichment of metallic nanotubes from a heterogeneous mixture based on their conductivity [26]. The method uses an alternating electric field to distinguish between the unique polarizability of metallic and semiconducting tubes, though the technique suffers from adhesion of the nanotubes to the fixed electrodes. Another technique, density gradient ultracentrifugation [156] has been used to fractionate nanotubes based on their relative densities. This technique is limited to batch-level processing, with no direct pathway for continuous high-volume throughput. Size-exclusion and ion exchange chromatography have been employed recently [157] to address the challenge of high throughput separations, though the process is heavily labor intensive and has not yielded material suitable for device applications

As discussed in this chapter, optoelectronic tweezers offers the ability to perform massively parallel manipulation of carbon nanotubes. The in-situ Raman characterization capability allows also for characterization of trapped objects in solution. Moreover, since OET works based on the DEP principle, it can also distinguish between different material properties due to their varying polarizability. This property was used in Section 3.3 to separate semiconducting and metallic nanowires. Therefore, OET offers an ideal platform for future investigations of massively parallel separation of semiconducting and metallic nanotube.

4.5 Summary

In conclusion, we have demonstrated that carbon nanotubes be translated and positioned in solution using OET virtual electrodes. OET is used as a general method to freely manipulate aqueous surfactant or surface functionalized dispersions of nanotubes in two dimensions. Optical control of nanotubes' density offers a potential means to tune electrical, thermal, optical, and mass transport properties in nanotube-composite thin films, opening new possibilities for device fabrication. The ability to perform in-situ Raman measurements is important for characterization of manipulated structures. In addition, the Raman signal enrichment can be used to create more sensitive Raman probes suggesting a broad range of applications chemical/biological sensing. Furthermore, this preliminary study will help guide future OET studies with semiconducting and metallic SWCNTs including separation of semiconducting and metallic nanotubes.

Chapter 5 Manipulation of Spherical Metallic Nanoparticles

5.1 Motivation

In recent years, there has been much interest in metallic nanoparticles as biological nano-sensors due to their interesting optical properties [9]. Optical tweezers have been used previously to trap metallic nanoparticles of different sizes [158, 159]; however, the high optical power intensities required for stable trapping ($\sim 10^7$ W/cm^2) result in excessive heating in metallic nanoparticles ($\Delta T > 55°C$) [160], hampering the application of optical tweezer-trapped particles in biological environments. Dielectrophoresis (DEP) can trap nanoparticles using fixed electrodes [161]; however, since the trapping positions are lithographically defined, fixed-electrode DEP lacks the capability to dynamically scan and manipulate the trapped particles. Trapping of single molecules has also been achieved using an Anti-Brownian Electrokinetic (ABEL) trap [6] which provides extensive information about the particle dynamics. However, this technique requires the molecules to be fluorescent.

In this chapter we will explore the application of OET in trapping, translation, and concentration of metallic nanocrystals (60 to 250 nm diameter).

5.2 Trapping of Individual Spherical Metallic Nanoparticles

5.2.1 Simulation and Modeling

Figure 5.1a shows the schematic of a single metallic nanoparticle trapped using OET. As discussed in Chapter 2, the magnitude of the DEP force is proportional to the volume of the particles and drops rapidly as the size of the particle reduces. However, the DEP force is also dependent on the gradient of the field intensity. As shown in Figure 5.1b, the gradient of field intensity is strongest near the OET surface and falls off sharply as we move away from the surface. Therefore, due to their small size, nanoparticles are immersed in the high-∇E^2 region

near the OET surface and feel a stronger field gradient relative to larger objects. The gradient of field intensity can be simulated using COMSOL finite-element modeling and is estimated to be 10^{16} – 10^{17} V^2/m^3 near the OET surface. Using this value, we can estimate the strength of the DEP force for a 100 nm diameter metallic nanoparticle to be approximately 0.1 pN, assuming a Clausius-Mossotti factor of 1 due to much higher conductivity of metal particle relative to the liquid medium. To estimate the velocity of the nanoparticles due to this DEP force, we can equate the drag force acting on the spherical nanoparticles to the DEP force ($F_{DEP} = F_{Drag}$), which results in a speed close to 100 μm/s. This suggests that spherical nanoparticles with dimensions close to 100 nm can be trapped and manipulated near the OET surface.

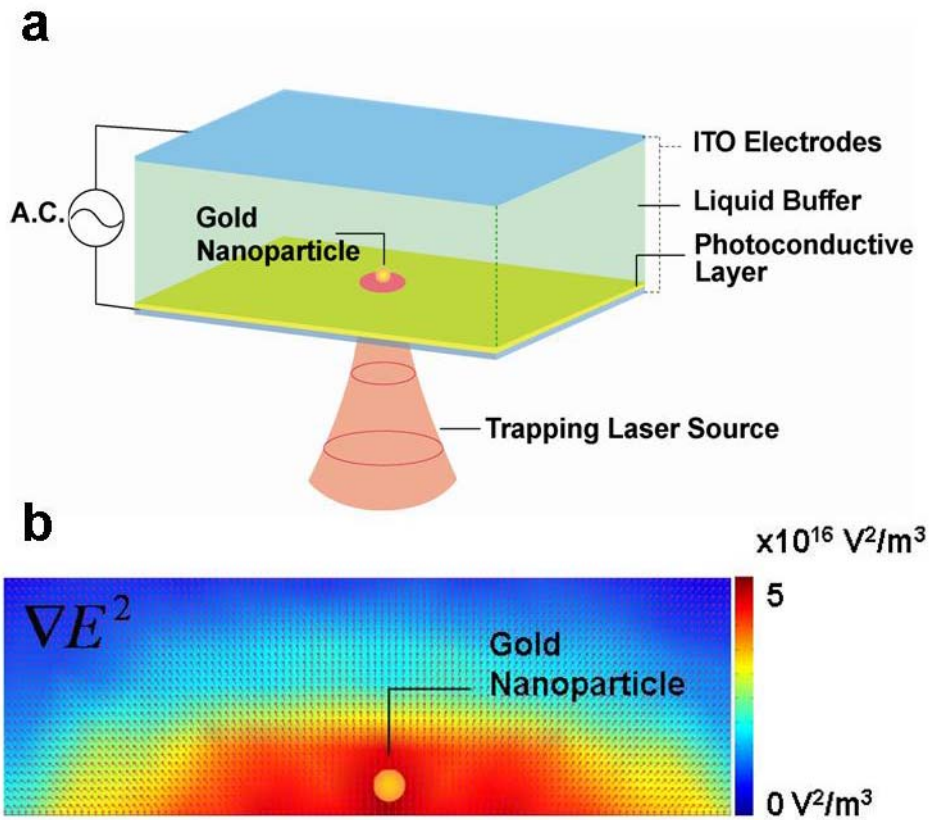

Figure 5.1 (a) Optoelectronic tweezers (OET) device structure for manipulation of nanoparticles. (b) The simulated gradient of electric field intensity is shown near the OET surface. The nanoparticles are immersed and trapped in the high field intensity gradient region near the OET surface. (© IEEE [79])

5.2.2 Temperature Analysis

Before we move on to metallic nanoparticle manipulation experimental results, it is important to discuss the amount of temperature increase for manipulated particles in the liquid solution. The temperature increase during the OET manipulation process is due to two effects: First is the absorption of trapping source illumination in the metallic particles. This is the main factor contributing to high temperature increase in metallic nanoparticles trapped with optical tweezers. However, as we will see, this effect is almost negligible in the case of OET since the

trapping sources are orders of magnitude less in optical intensity relative to optical tweezers. The second source of temperature increase is due to the joule heating of the liquid and absorption of illumination in the photoconductive layer. This effect is present in the OET device due to application of the AC voltage bias.

To estimate the temperature increase due to the absorption of the trapping laser source in metallic particles, we will follow an analysis similar to reference [160]. The temperature increase in OET-trapped nanoparticles can be estimated as:

$$\Delta T = \frac{P_{abs}}{4\pi r C} \tag{5.1}$$

where C is the thermal conductivity of water (0.6 W/K.m), r is the radial distance from the nanoparticle's center, and P_{abs} is the absorbed power in the nanoparticle given by:

$$P_{abs} = \sigma_{abs} I^2 \tag{5.2}$$

where I is the laser intensity and σ_{abs} is the absorption cross section of the nanoparticle given by:

$$\sigma_{abs} = \frac{2\pi n_m}{\lambda} \times \mathrm{Im}\left[\frac{3V(\varepsilon_p^* - \varepsilon_m^*)}{\varepsilon_p^* + 2\varepsilon_m^*}\right] \tag{5.3}$$

where $\varepsilon_m^* \approx 1.77$ ($n_m \approx 1.33$) and $\varepsilon_p^* \approx -10.66 + i1.37$ at λ = 635 nm and V is the volume of the nanoparticle. For a 20 μW trapping laser source with 1.7 μm (FWHM) spot size, we can estimate the temperature increase at the surface of 60 to 250 nm diameter gold nanoparticles due to absorption to be less than 0.1°C. Therefore, this effect is almost negligible relative to very high temperature increases observed in optical tweezers (ΔT > 55°C) [160].

The second source of temperature increase in OET is due to the joule heating of the liquid solution and the photoconductive layer. We characterized this effect in Section 2.4.4 and simulated the temperature increase to be approximately 2-3°C. We can also estimate the joule heating effect using [162]:

$$\Delta T_{joule} = \frac{\sigma_{liquid} V^2}{2C} \tag{5.4}$$

where σ_{liquid} is the liquid conductivity, V is the applied voltage, and C is the thermal conductivity of water. Using the typical experimental values for nanoparticle trapping (σ_{liquid} = 1-10 mS/m, V = 10-20 V peak-to-peak), we can estimate the temperature increase due to joule heating to be less than 2°C, which is about an order of magnitude larger than the temperature increase due to absorption in metallic nanoparticles. Therefore, joule heating would be the dominant effect in the OET environment. However, the combined effect of joule heating and absorption in OET produce temperature increases of 2-3°C, which is at least an order of magnitude smaller than optical tweezers and is within acceptable range for biological experiments.

5.2.3 DEP Manipulation of Spherical Gold Nanoparticles

Gold nanoparticles with 60 to 250 nm diameters with an approximately 10^{10} particles/ml density were diluted in a 2.6 mS/m conductivity solution of DI water and KCl. 4 μL of the sample was introduced into the OET device. Majority of the nanoparticles showed strong Brownian while a portion of the particles adhered to the surface. A 635 nm diode laser with 20 μW power and 1.7 μm (FWHM) optical spot size at the OET surface was used to trap the nanoparticles. AC voltages of 10-20 Vpp at 50-100 kHz frequency were applied to the OET device. Dark field microscopy using a BX51M Olympus microscope was used to visualize the nanoparticles and images were captured using a CCD camera. Figure 5.2 shows trapping of a single 100 nm gold nanoparticle using OET. The nanoparticle experiences a positive DEP force and is attracted to the laser trapping source. By manually adjusting the laser trap position, the nanoparticle is transported over an approximately 200 μm^2 area in 12 seconds.

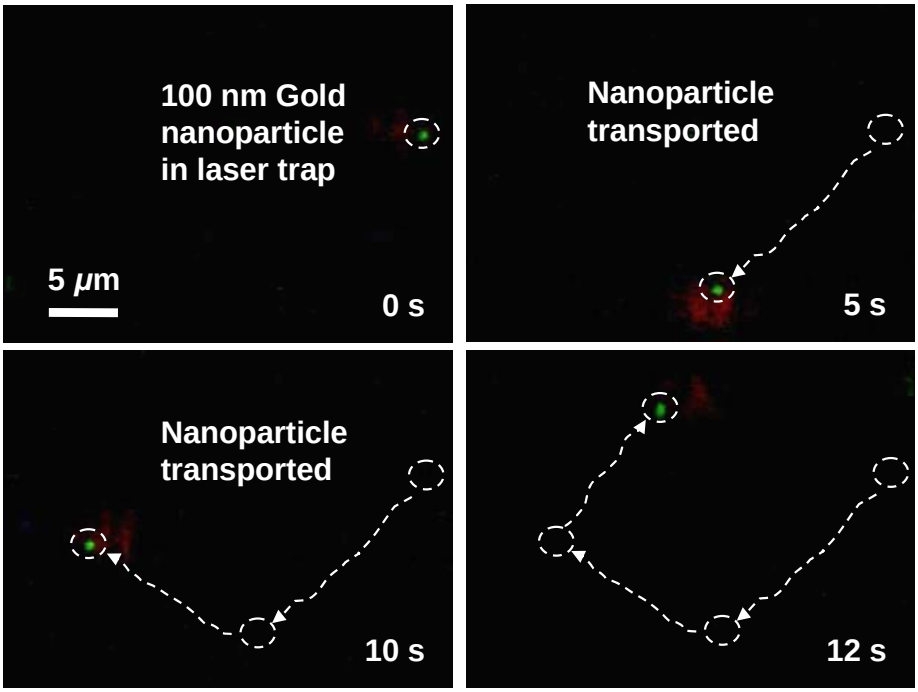

Figure 5.2 Trapping and transport process of a single 100 nm gold nanoparticle using OET. The nanoparticle is transported over an approximately 200 μm^2 area in 12 seconds. (© IEEE [79])

To quantify the maximum trapping speed of the metallic gold nanoparticles, an ESP-300 Newport motorized actuator controller and a LTA-HL motorized actuator was used to move the microscope stage relative to the optical pattern. Figure 5.3 shows the maximum translational speeds of 100 nm gold nanoparticles as a function of the applied AC voltage. The experimental data follows a quadratic trend (black fitted line) which is expected since the DEP force is proportional to the gradient of the field intensity. A 68 μm/s maximum translation speed is

measured for an applied AC voltage of 20 Vpp. This measured translational speed is close to the calculated speeds for metallic nanoparticles.

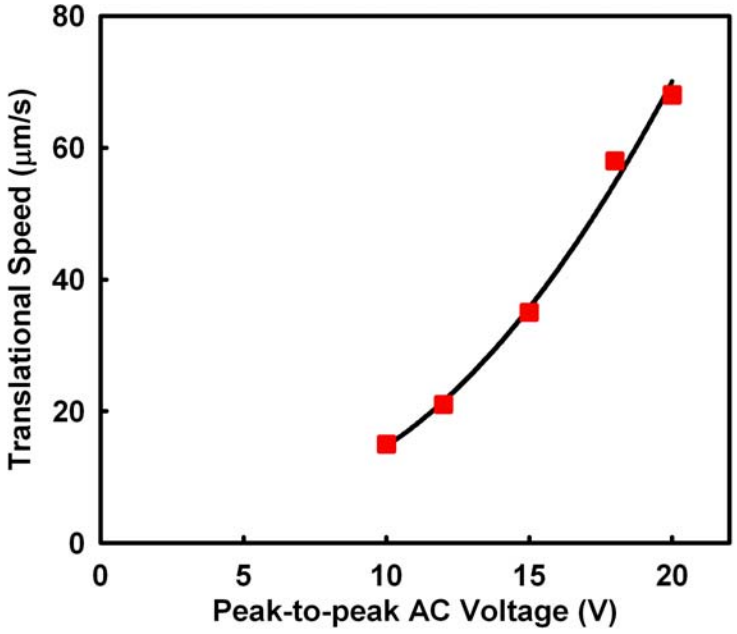

Figure 5.3 OET-trapped nanoparticles' translational speed as a function of the applied voltage. A maximum translational speed of 68 μm/s at 20 Vpp is achieved. The experimental data follows a quadratic trend (black fitted curve). This is expected since the DEP force is proportional to ∇E^2. (© IEEE [79])

When more than one nanoparticle is trapped in the laser, the particles experience a mutual repulsive force due to two effects. First, nanoparticles carry a negative surface charge with a zeta potential of ξ = -70 mV resulting in a mutual columbic repulsion. Second, the dipoles induced in the nanoparticles interact with each other resulting in a dipole-dipole repulsive force which is a function of the applied voltage. By measuring the translation speeds of the particles after removing the laser trap, the net repulsive force between two 100 nm gold nanoparticles can be calculated to be approximately 23 fN at 20 Vpp (Figure 5.4a). This repulsive force acting on more than two particles can also be observed as shown in Figure 5.4b for three nanoparticles. In the beginning the three particles are trapped in the laser source (filtered out), once the laser trap is removed, the mutual repulsion between the particles repels them from each other.

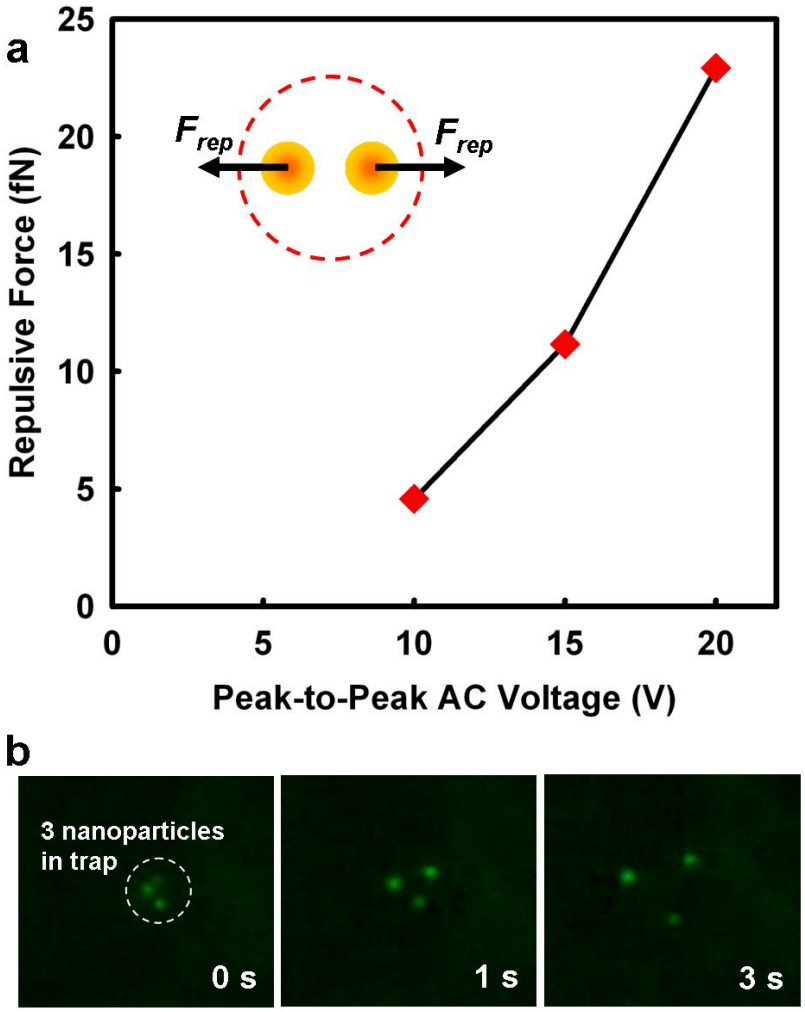

Figure 5.4 (a) The repulsive force (F_{rep}) between two nanoparticles (due to dipole-dipole interaction and columbic repulsion) as a function of applied voltage. (b) The repulsive force interaction is also observed for three nanoparticles. In the beginning, the particles are trapped using OET (laser filtered out), once the trap is removed, the nanoparticles repel each other. (© IEEE [79])

Figure 5.5a-d shows trapping and transport of five 250 nm gold nanoparticles using OET. Nanoparticles are concentrated in the OET trap and can be transported by scanning the laser trap manually, once the laser trap is removed, nanoparticles undergo Brownian motion and the five gold nanoparticles are distinctly observable. The ability to concentrate the nanoparticles in a single spot is important to enhance the sensitivity of the dynamic hot-spots for imaging and sensing applications.

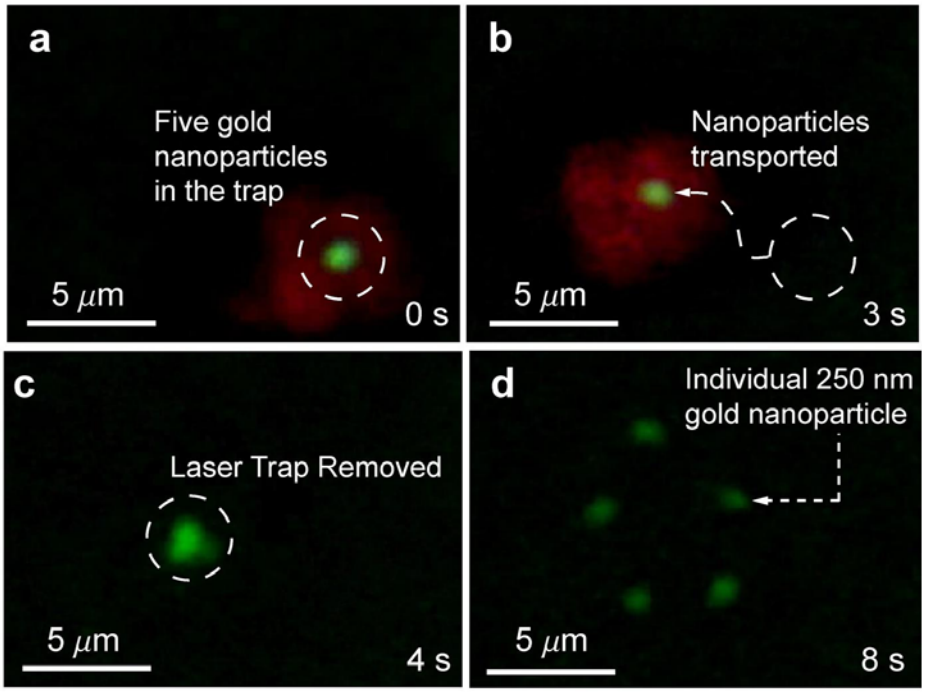

Figure 5.5 Trapping and transport of five 250 nm gold nanoparticles. (a) Nanoparticles are trapped and concentrated in the laser trap. (b) Nanoparticles are transported to a new location by manually adjusting the laser position. (c) Laser trap is removed and nanoparticles undergo Brownian motion. (d) Five gold nanoparticles are distinctly observable after removal of the trap. (© IEEE [79])

5.3 In-situ surface enhanced Raman spectroscopy (SERS) using metallic nanocrystals

As discussed in section 3.2.5, it is possible to integrate the OET manipulation setup with a Raman spectroscopy setup to perform in-situ Raman measurement of trapped objects. Metallic nanocrystals such as gold nanoparticles have been shown to enhance the magnitude of Raman signals from molecules placed in their vicinity as much as 10^{14} times [10, 11]. This effect is referred to as surface-enhanced Raman spectroscopy or SERS and plays an important role in sensing applications since Raman scattering is an inherently inefficient process and the enhancement of Raman signal makes it much easier to detect the "fingerprint" of molecules. Therefore, the OET-trapped nanoparticles can be used as a dynamic sensor in the OET chamber to sense the Raman signal from a dilute solution of molecules. To demonstrate this capability, we have mixed a 24 μM solution of trans-1,2-bis(4-pyridyl)ethane [163] (BPE) molecules with the nanoparticles solution in 1:1 ratio. A single laser source (785 nm, 30 mW) was used to collect the nanoparticles and detect the Raman signal. Figure 5.6 shows the collection of nanoparticles after the application of trapping laser, the dotted line indicates the laser area.

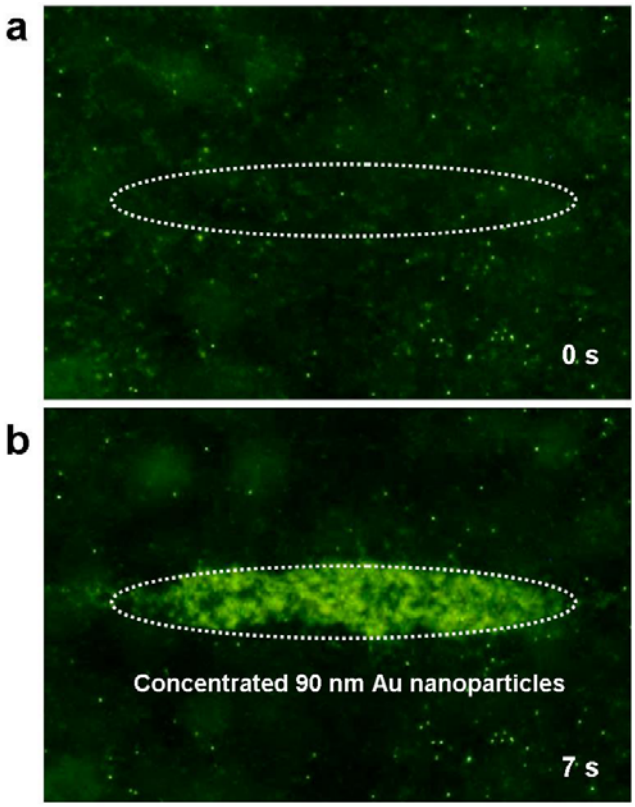

Figure 5.6 Collection of 90 nm gold nanoparticles in the OET chamber for enhancement of Raman signal from a dilute solution of BPE molecules.

Figure 5.7 shows the detected Raman signal from the BPE molecules in the solution as a function of time. There are nine individual spectra acquired 4 seconds apart from each other starting at the onset of application of the laser source. As we can see, the Raman signal grows over time and reaches a maximum which indicates the maximum concentration of nanoparticles achieved. We can also observe the same effect by leaving the laser on but suddenly turning on the AC voltage and observing the Raman signal grow over time (Figure 5.8) as more particles are attracted to the illumination area.

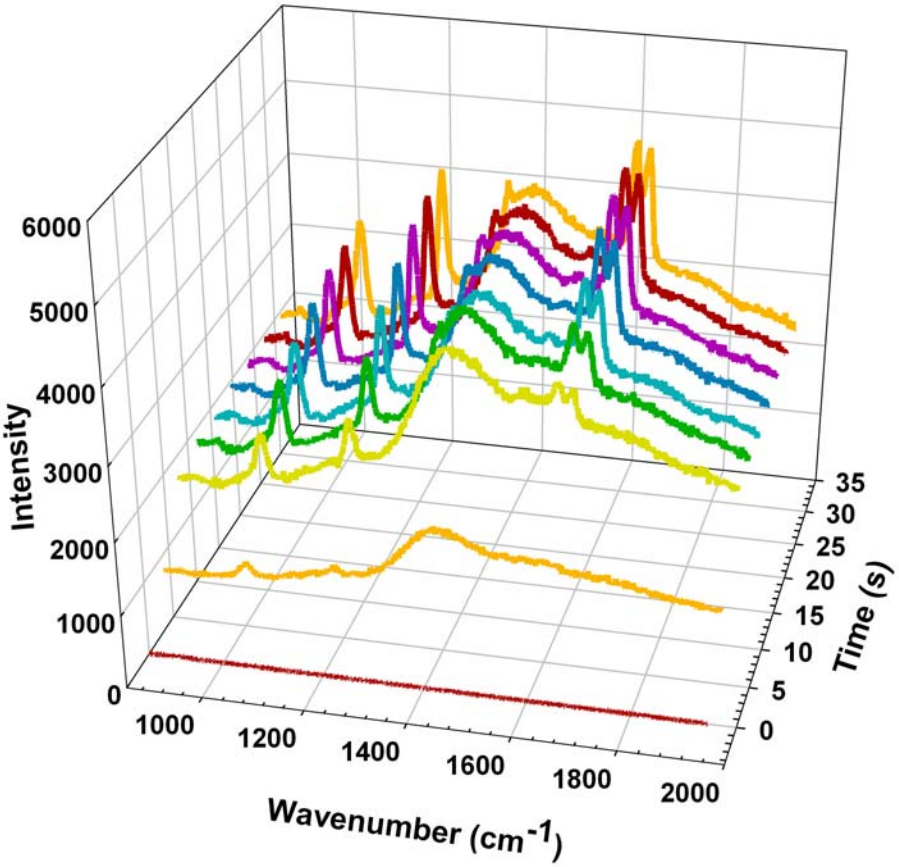

Figure 5.7 In-situ surface enhanced Raman spectra of BPE molecules using OET trapped 90 nm gold nanoparticles. The nine individual spectra were acquired 4 seconds apart from each other. The laser source is applied at a time between the first and second spectra. As soon as the laser is applied, the Raman signal grows over time as more particles are attracted to the illumination area.

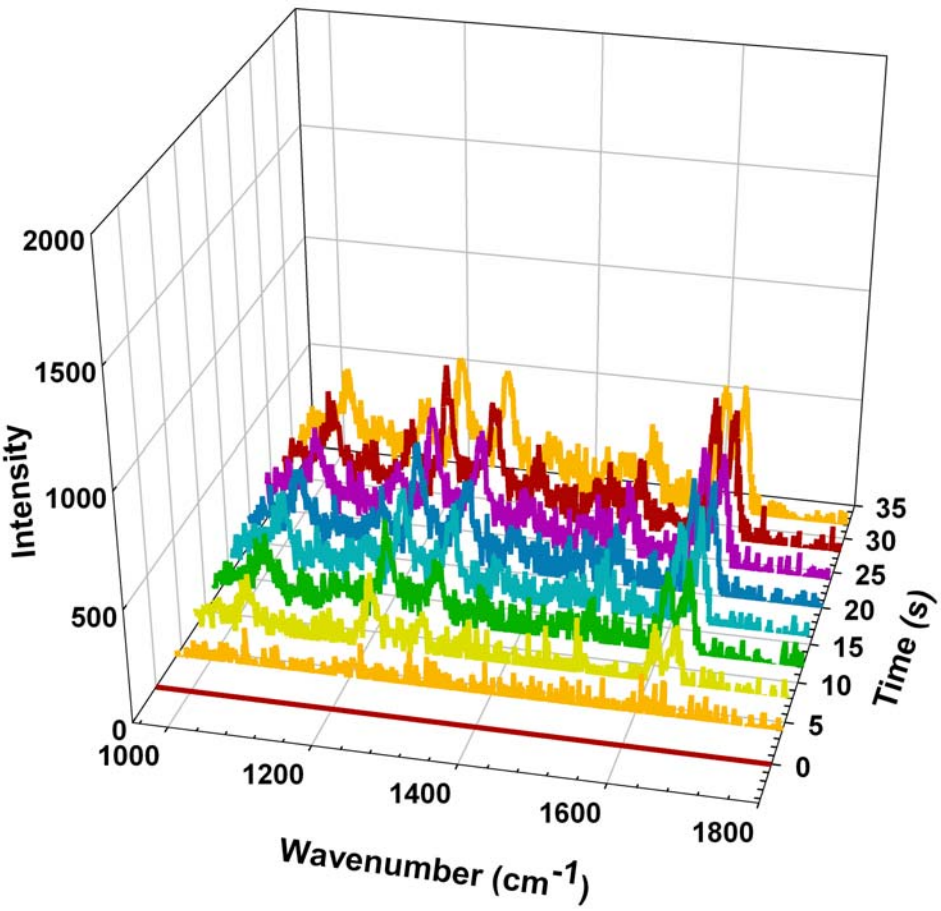

Figure 5.8 In-situ surface enhanced Raman spectra of BPE molecules using OET trapped 90 nm gold nanoparticles. The nine individual spectra were acquired 4 seconds apart from each other. The AC voltage source is applied at a time between the first and second spectra. As soon as the voltage is applied, the Raman signal grows over time as more particles are attracted to the illumination area. The background signal is subtracted from all spectra.

Other measurement techniques such as two-photon photoluminescence (TPPL) of metallic nanostructures have also been used for in-vivo and in-vitro imaging of biological objects [164, 165] and can be combined with OET manipulation platform to allow real-time dynamic imaging and manipulation of metallic particles. Moreover, OET can potentially be used to concentrate and position nanoparticles of interest near the surface of cells. This capability combined with cell surgery techniques [166, 167] could be used for targeted delivery of sensors inside the cells to study cellular processes such as phosphorylation [168].

5.4 Summary

In this chapter, we demonstrated the use of OET for trapping and concentration of single and multiple spherical gold nanoparticles with 60 to 250 nm diameters. Due to low optical intensities required for stable trapping we estimate the temperature increase in OET-trapped nanoparticles

due to absorption and joule heating to be only a few °C, which is at least one order of magnitude smaller than particles trapped with optical tweezers. The limited temperature increase makes OET a suitable technique for manipulation of metallic nanoparticles in biological environments. Moreover, through integration of OET trapping setup with Raman spectroscopy, it is possible to use OET-trapped nanoparticles as dynamic surface-enhanced Raman spectroscopy (SERS) sensors for a variety of in-situ chemical/biological sensing and imaging applications.

Chapter 6 NanoPen: Dynamic, Low-Power, and Light-Actuated Patterning of Nanoparticles

6.1 Motivation

The ability to pattern nanostructures has important applications in medical diagnosis [169, 170], sensing [171], nano- and optoelectronic device fabrication [172, 173], nanostructure synthesis [174], and photovoltaics [175]. Several techniques such as dip-pen nanolithography [49-54], nanofabrication [55], contact printing [41-44], self-assembly [176, 177], and Langmuir-Blodgett [178] have been used to pattern nanostructures. However, these techniques lack the capability to create real-time reconfigurable patterns without the use of complicated instrumentation or processing steps. Various optical patterning techniques [179-183] have tried to overcome this challenge. Optical patterning of nanoparticles has been achieved previously by actuating an indium-tin oxide (ITO) layer as a photoconductive material and generating local current densities to concentrate the nanoparticles. However, these methods suffer from a slow patterning process [179] (several minutes to hours) or they require very high optical intensities [180] ($\sim 10^5$ W/cm^2) to pattern the nanostructures. These limitations prevent the widespread application of such techniques. Alternatively, optical tweezers have been used to manipulate and permanently assemble nanostructures onto the substrate [181, 182]. Moreover, optical tweezers have been combined with local heating of nanoparticles to create convective flows for collection and patterning of particles [183]. However, optical tweezers are also limited to using very high optical intensities ($\sim 10^7$ W/cm^2) and high numerical aperture objectives, which limits the ease of operation, reduces the available working area, and potentially damages the nanoparticles [181].

[*] Reproduced in part with permission from [85] A. Jamshidi, S. L. Neale, K. Yu, P. J. Pauzauskie, P. J. Schuck, J. K. Valley, H. Y. Hsu, A. T. Ohta, and M. C. Wu, "NanoPen: Dynamic, Low-Power, and Light-Actuated Patterning of Nanoparticles," *Nano Lett.,* vol. 9, pp. 2921–2925, 2009. Copyright 2009 American Chemical Society.

As we discussed extensively in Chapter 2, in addition to optically induced dielectrophoresis [96], there are other major electrokinetic forces present in the OET device [68], including, light-actuated AC electroosmosis (LACE) [67, 184] and electrothermal (ET) [185] flow. In this chapter, we will demonstrate that the combination of these electrokinetic effects in OET optofluidic platform can be used to "directly write" patterns of nanoparticles. We call this novel technique *NanoPen*.

6.2 NanoPen Mechanism

NanoPen uses various electrokinetic forces (DEP, LACE, and ET) to collect and permanently immobilize nanoparticles on the OET surface. NanoPen can be operated to collect and immobilize single and multiple nanoparticles such as spherical metallic nanocrystals and one-dimensional nanostructures such as multi-wall carbon nanotubes. Please note that the name NanoPen refers to a method for patterning nanoparticles (a Nanoparticle Pen) and does not mean nanoscale positioning accuracy. Figure 6.1 shows the device structure for OET nanopatterning optofluidic platform. The nanoparticles of interest, such as metallic nanocrystals, carbon nanotubes, and nanowires are dispersed in a KCl/DI water solution with 1-10 mS/m conductivity and are introduced into the OET chamber. There is an AC voltage applied between the two ITO electrodes, with 10-20 peak-to-peak voltage and 10-100 kHz frequency. To actuate the OET device, an optical pattern is projected on the a-Si:H layer, either by using a laser source, a spatial light modulator, or a commercial projector.

Figure 6.1b depicts finite-element simulation (using COMSOL Multiphysics) of various electrokinetic forces in the OET chamber for an applied voltage of 20Vpp at 10 kHz, with 1 mS/m liquid conductivity. The NanoPen mechanism benefits from the combination of these electrokinetic forces generated in the OET optofluidic platform. In particular, there are two distinct forces that lead to light-actuated patterning of nanoparticles: a *collection force* responsible for collecting the particles from long range (over 100 μm distances) and concentrating them in the light spot and an *immobilization force* which strongly attracts the particles (with up to 0.1 pN forces) and immobilizes them on the OET surface. The collection force benefits from DEP force attraction of particles over the short range and LACE and ET flow-based collection of the particles over the longer range. The immobilization force which is responsible for attracting the particles to the surface is mainly dominated by the DEP force but is also affected by electrophoretic forces due to the particles surface charges.

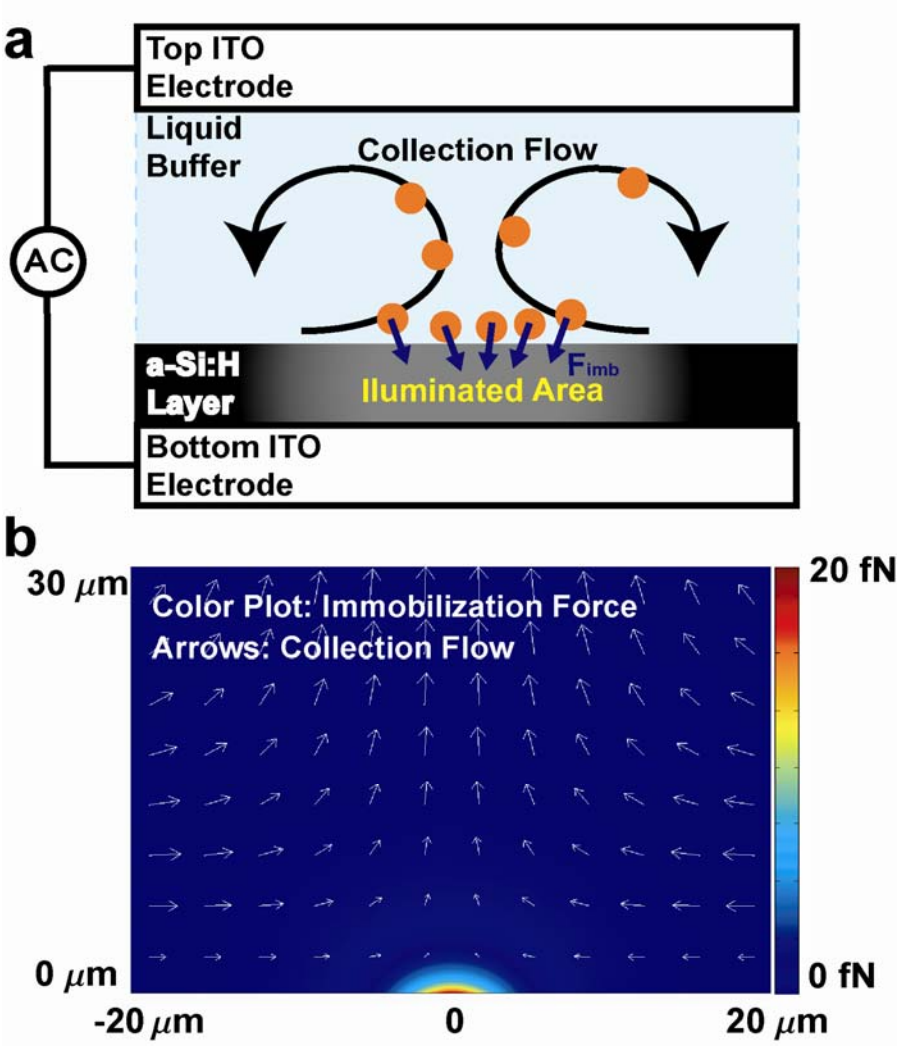

Figure 6.1 (a) Optoelectronic tweezers (OET) optofluidic platform used to realize the NanoPen process. The collection flow collects the particles towards the illuminated area and the immobilization force (F_{imb}) patterns the particles on the surface. (b) Finite-element simulation of the NanoPen process. The arrows indicate the collection flow which is a combination of the electrothermal (ET) flow and light-actuated AC electroosmosis (LACE) flow. The immobilization force consists mainly of the dielectrophoresis (DEP) force. (© American Chemical Society [85])

6.3 NanoPen Patterning of Nanoparticles

Figure 6.2a shows NanoPen immobilization and patterning of 90 nm diameter gold nanoparticles (purchased from Nanopartz Inc. [186]) dispersed in a 5 mS/m solution of KCl and DI water with ~ 10^{11} particles/ml concentration. In the beginning, there is no voltage applied to the device and the nanoparticles undergo Brownian motion. Once the voltage is applied (20Vpp at 50 kHz), the nanoparticles are collected in the center of the light spot (continuous-wave 633 nm diode laser, 100 μW) and are immobilized on the OET bottom surface. The stage is then manually transported leaving a trace of gold nanoparticles in the illuminated area on the OET

surface. Once the immobilization process is complete, the liquid solution can be removed without damaging the patterned structure. The patterned surface remains intact after multiple rinsing and drying steps.

The line-width and density of immobilized structures can be tuned by adjusting the AC voltage source parameters such as peak-to-peak voltage and frequency, light source parameters such as light intensity and spot size, and operational parameters such as the exposure time and light pattern scanning speed. An example of this area density tuning is shown in Figure 6.2b where the number of patterned nanoparticles within the illuminated area is increased by increasing the exposure time from 2 seconds to 120 seconds. After completion of the patterning process, the top ITO is removed and the remainder of the liquid is blow-dried leaving the patterned structures intact. The inset shows the SEM image of the patterned spots. Figure 6.3 shows expanded SEM images of each spot; the number of particles patterned ranges from ~250 particles for a 2 second exposure to ~6500 particles for a 120 second exposure (Figure 6.3b).

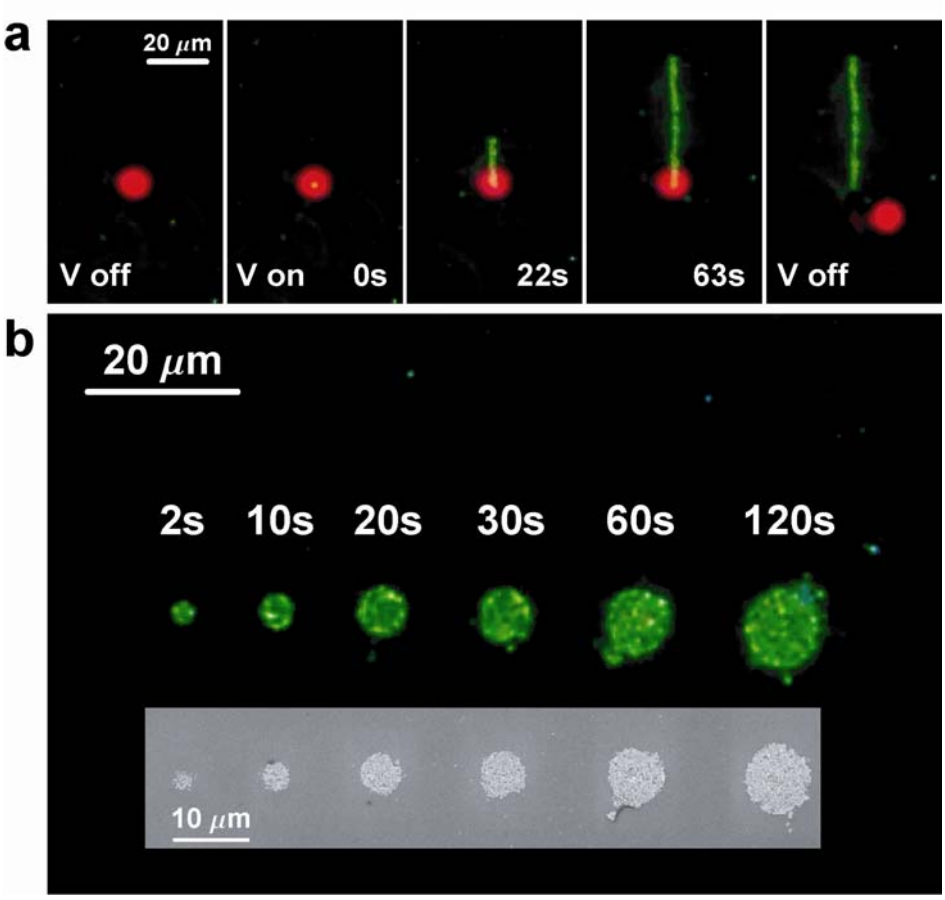

Figure 6.2 (a) Real-time patterning of 90 nm diameter gold nanoparticles by translating the stage while patterning the particles in the illuminated area. The red spot is the patterning beam and the green areas indicate the patterned nanoparticles. In the beginning the voltage is off and no particles are immobilized, once the voltage is turned on, the nanoparticles are collected and permanently patterned in the illuminated area. The stage is manually transported, leaving a trace of the nanoparticles behind. Once the patterning is complete, the voltage is turned off and the patterning process stops. (b) Increasing the exposure time expands the patterned area and density of particles within the illuminated region as indicated for 2-120s exposure times. The inset shows the SEM image of the patterned spots. (© American Chemical Society [85])

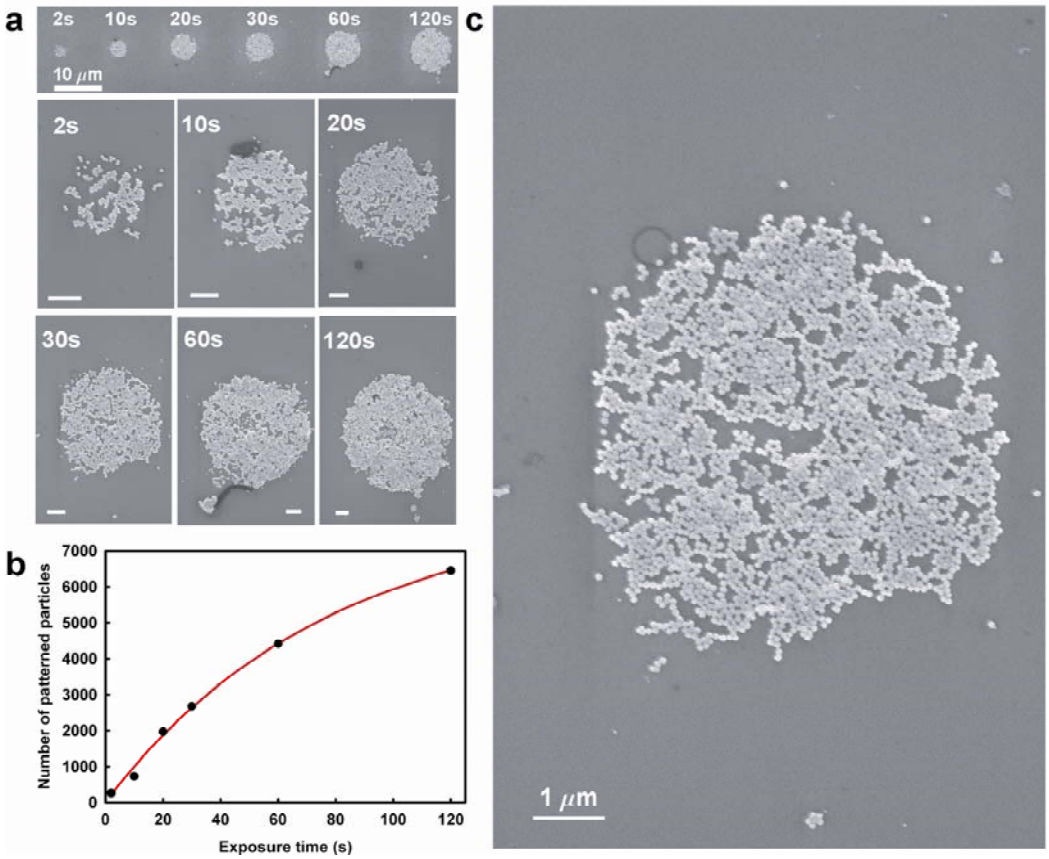

Figure 6.3 (a) SEM images of NanoPen patterned 90 nm Au nanoparticles with 2, 10, 20, 30, 60, 120 second exposure times. All scale bars are 1 μm unless otherwise noted. (b) Approximate number of particles as a function of the exposure time. (c) An expanded view of the 30 second exposure spot. (© American Chemical Society [85])

In addition, using a diluted nanoparticle solution, NanoPen is capable of patterning single nanoparticle as depicted in Figure 6.4 for patterning a single 90 nm-diameter spherical gold nanoparticle.

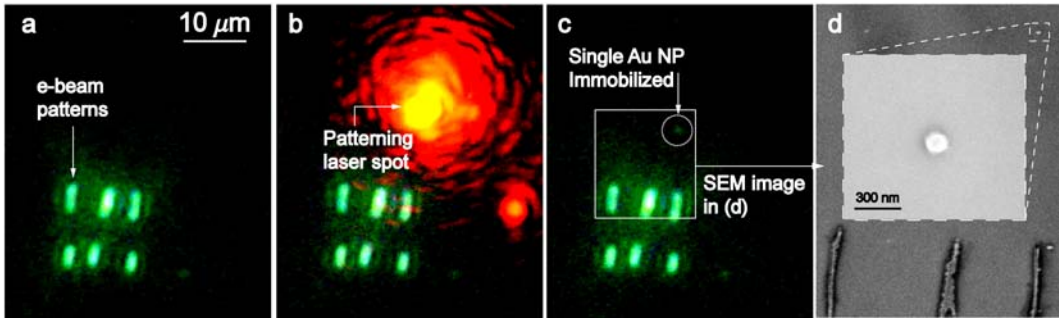

Figure 6.4 Immobilization of a single 90 nm diameter gold nanoparticle. (a) Pre-designated target patterns were fabricated on the OET device using e-beam lithography. (b,c) Once the laser spot is positioned, a nanoparticle is attracted and patterned on the surface, ~10 μm above the e-beam pattern. (d) SEM image of the area indicated in (c) by the white rectangle, showing the patterned nanoparticle near the e-beam structure. The inset is a zoom-in SEM image of the particle. (© American Chemical Society [85])

NanoPen is also capable of patterning one-dimensional nanostructures such as multi-wall carbon nanotubes (Figure 6.5) as well as semiconducting and metallic nanowires (Figure 6.6). It is important to note that during the patterning process, the CNTs are oriented vertically due to the torque experienced by 1-dimensional nanostructures in the electrical fields. However, after the patterning process is completed and the AC voltage is removed, the 1-dimensional structures fall on the surface with random orientations which increases the effective linewidth of the patterned structures. One potential way to achieve better orientation of these structures would be to use a lateral field optoelectronic tweezer (LOET) device [76, 77].

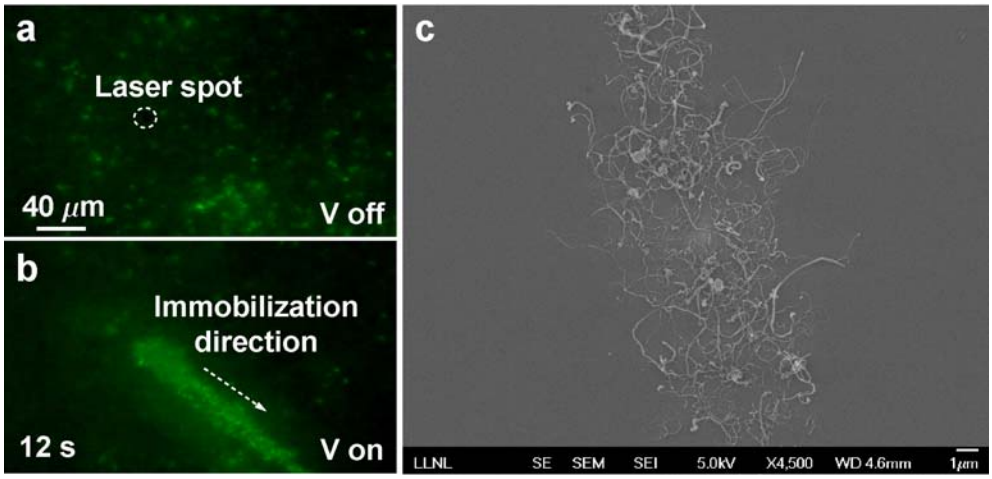

Figure 6.5 NanoPen immobilization of multi-wall carbon nanotubes (MWCNTs). (a) There is no voltage applied to the device and the nanotubes undergo Brownian motion. (b) Once the voltage is applied, the nanotubes are collected in the center of the laser trap and patterned on the substrate as the laser source is translated manually. (c) Scanning electron microscopy (SEM) image of a line of MWCNTs immobilized on the surface of the OET device using NanoPen. The linewidth is approximately 10 μm. Multi-wall carbon nanotube samples were purchased from SES and were dispersed in a 5:1 SDBS:mwCNT solution for solubilization followed by sonication and centrifugation. (© American Chemical Society [85])

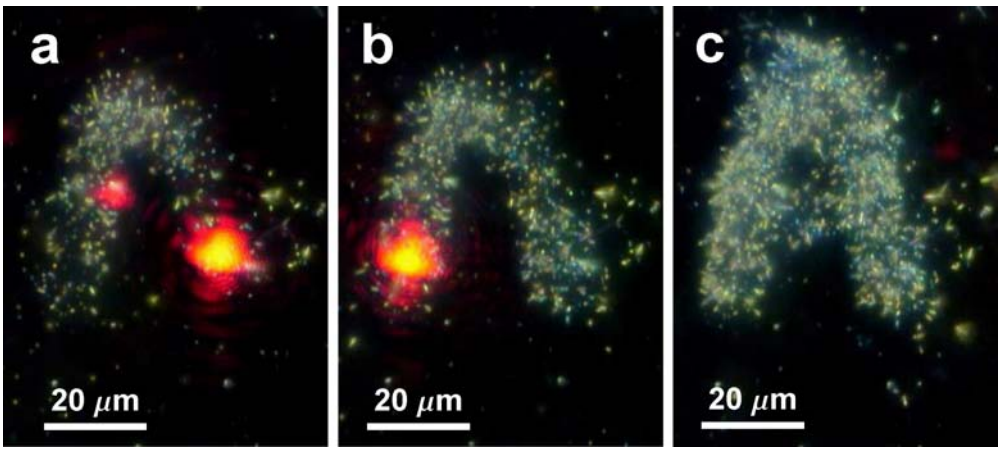

Figure 6.6 NanoPen patterning of semiconducting (silicon) nanowires. (a-c) The process of patterning silicon nanowires in the form of character ("A") using the NanoPen technique. (© American Chemical Society [85])

To further investigate the patterning process, we performed experiment with 90 nm diameter gold nanoparticles with different surface charges. We have observed similar patterning characteristics for gold nanoparticles with negative (-carboxyl conjugated), positive (-amine conjugated), and neutral (-methyl conjugated) surface charges. Figure 6.7 demonstrates the

NanoPen patterning process for neutral –methyl coated nanoparticles. These observations along with the fact that our patterning process does not require any DC bias applied to the device further suggest that the DEP force is the dominant immobilization force relative to electrophoretic effects.

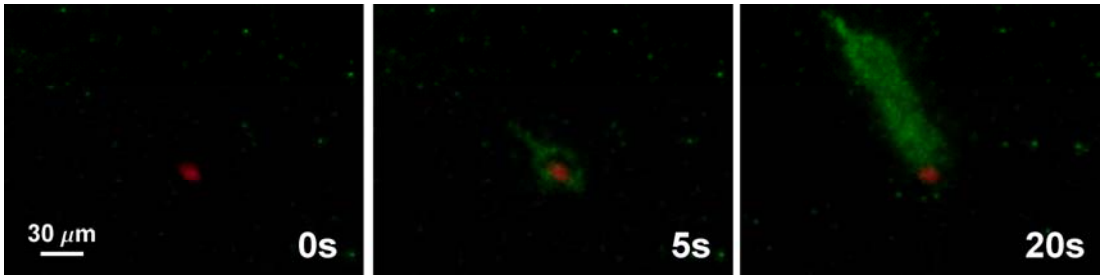

Figure 6.7 NanoPen patterning of neutral (methyl-coated) 90 nm diameter Au nanoparticles. The nanoparticles are patterned on the surface using the NanoPen process by keeping the trapping laser stationary and translating the stage manually relative to the patterning laser source. (© American Chemical Society [85])

6.4 Large-Scale and Low-Power Patterning of Nanoparticles

Since NanoPen is a light-induced patterning technique, it can be used for dynamic and flexible patterning of nanoparticles by adjusting the projected light pattern using a spatial light modulator. Moreover, the low required optical power intensity for actuation of NanoPen makes it possible to pattern the nanostructures using a commercial projector (Dell, 2400MP with 3000 ANSI Lumens, 1024x768 resolution) with <10 W/cm^2 optical intensity. To demonstrate this capability, we have patterned 90 nm diameter gold nanoparticles in the form of a 10×10 array over a 150×140 μm^2 area, the "NIH" logo over a 160×140 μm^2 area, and the "CAL" logo over a 140×110 μm^2 area, as shown in Figures 6.8a, 6.8b, and 6.8c, respectively. These arbitrary patterns were created through a Microsoft Powerpoint interface with the projector. The optical patterns were then focused onto the OET chip using a 20× objective. The exposure time for 10×10 spots array is 2 minutes. The slight non-uniformity in the patterns is due to the non-uniformity of the projected light patterns and could be improved through better optical alignment.

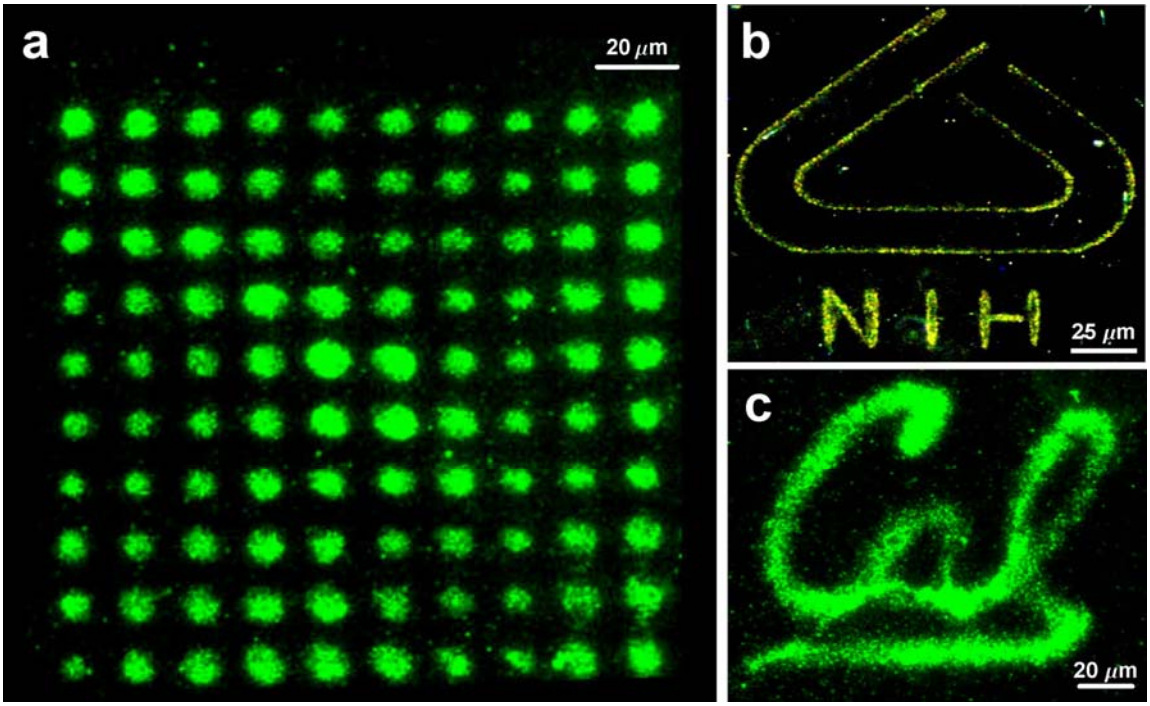

Figure 6.8 Large area patterning of nanoparticles using NanoPen. Patterning of 90 nm diameter gold nanoparticles in the form of (a) a 10×10 array, over 150×140 μm^2, (b) "NIH" logo over 160×140 μm^2,and (c) "CAL" logo over 140×110 μm^2, all using a commercial light projector (<10 W/cm^2 light intensity). (© American Chemical Society [85])

6.5 Surface-Enhanced Raman Spectroscopy (SERS) using NanoPen Patterned Gold Nanoparticles

Applications of patterned nanostructures range from fabrication of opto- and nanoelectronic devices in case of nanowires and carbon nanotubes[172, 173] to DNA microarrays [169, 170] depending on the type and characteristics of the patterned nanoparticles. In recent years, metallic nanocrystals have received much attention as local, sub-diffraction limited nanosensors [171] for medical and chemical diagnosis and imaging, due to their interesting plasmonic properties. Therefore, NanoPen patterned metallic nanoparticles present a method for flexible and dynamic patterning of SERS sensing structures. To explore this capability further, we tried a solution of Rhodamine 6G (R6G) dye on the surface of an arbitrary NanoPen patterned structure (Figure 6.9a). The NanoPen patterned SERS substrates were prepared by patterning a solution of 60-90 nm gold nanoparticles on the OET surface using the NanoPen process. Once the patterning is complete, the top ITO cover glass is removed and the remaining liquid is blow dried, leaving the patterned area intact. The two-dimensional Raman scan (at 1570 cm^{-1} Raman shift) of the structure indicates strong signal enhancement in the areas that nanoparticles are patterned. Moreover, we observe that positions with higher nanoparticle concentration (longer exposure time) show better enhancement relative to areas with lower particle density. A typical Raman signal achieved from R6G molecules (using a 3 mW, 532 nm laser excitation) is shown in Figure 6.9a inset.

To quantify the SERS enhancement factor for NanoPen patterned gold nanoparticles, we dried 1-10 μL droplets of a 100 nM solution of trans-1,2-bis(4-pyridyl)ethane [163] (BPE) molecules on a patterned area, followed by a two-minute rinse with methanol and water. Raman measurements were then performed using a Raman setup built around an inverted TE2000 Nikon microscope. 10×, 40×, or 60× objectives were used to focus the laser source (785 nm, 30 mW) onto the sample and collect the Raman signal. As shown in Figure 6.9b, the enhancement factor is calculated by comparing the Raman signal intensities acquired from the 100 nM BPE molecules dried on the SERS structures to the Raman intensities acquired from a benchmark solution of 10 mM BPE. At the 1200 cm^{-1} Raman shift peak, the Raman intensity for 100 nM solution for the SERS structures is 32,000 counts versus 250 counts for the 10 mM benchmark solution leading to an enhancement factor (*EF*) of,

$$EF = \frac{32{,}000}{250} \times \frac{10mM}{100nM} \approx 1.3 \times 10^7 \qquad (6.1)$$

Figure 6.9b inset shows a zoomed-in version of the Raman signal of the main plot in the range 1100-1350 cm^{-1}, with the 10 mM benchmark solution Raman signal multiplied by a factor of 25 to make it more visible. The BPE Raman signals were achieved for 4 second integration using a 30 mW, 785 nm laser source and all signal levels are measured relative to the background. In addition, we observed strong SERS signal with concentrations as small as pico-molars.

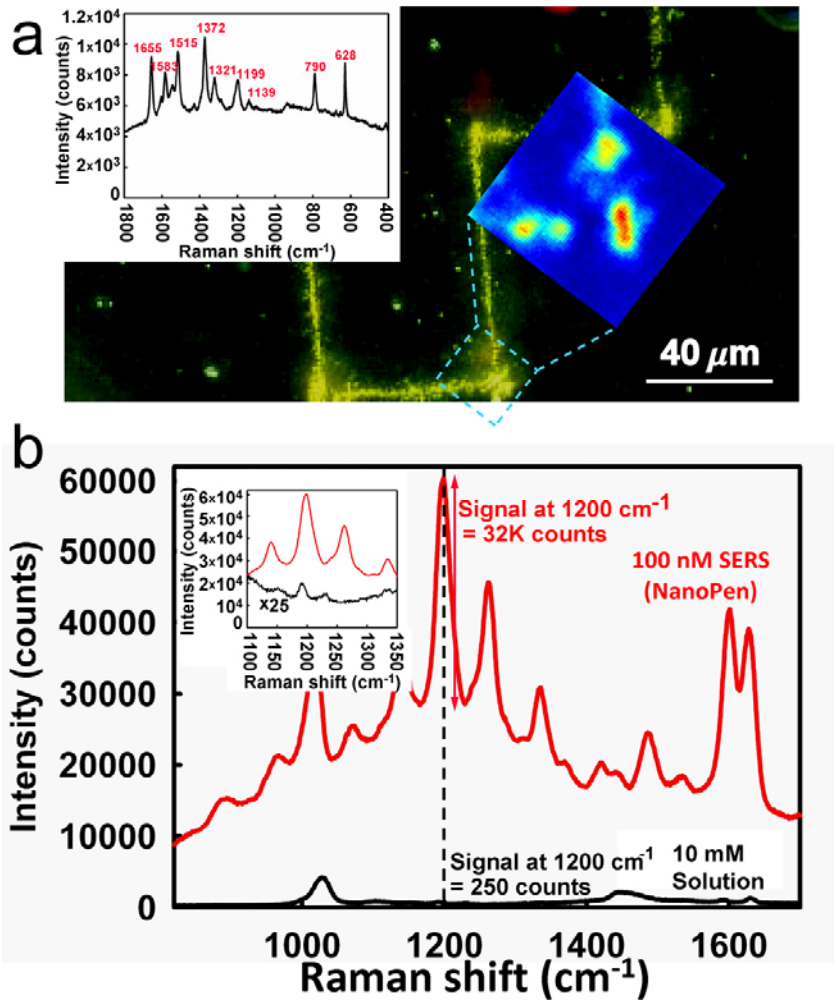

Figure 6.9 Surface-enhanced Raman spectroscopy (SERS) using NanoPen patterned metallic nanoparticles. (a) Measurement of Rhodamine 6G (R6G) spectrum using the NanoPen patterned gold nanoparticle (mixture of 60 and 90 nm sizes). The 2-dimensional scan of Raman signal at ~1570 cm^{-1} Raman shift indicated a large enhancement in the areas with higher density nanoparticles. The inset shows a typical Raman spectrum of R6G achieved. (b) Characterization of Raman enhancement factor for the BPE molecules. The Raman signal level is compared for 100 nM BPE solution on NanoPen SERS structures (red line) to the Raman signal from a benchmark 10 mM solution of BPE (black line). The inset shows a zoom-in of 1100-1350 cm^{-1} Raman shift range with the benchmark 10 mM solution signal multiplied by 25 to make it more visible. The calculated enhancement factor at the 1200 cm^{-1} Raman shift peak is ~10^7. (© American Chemical Society [85])

6.6 Summary

Currently, due to the small size of the patterned particles (<100 nm), the positioning accuracy is limited predominantly by Brownian motion and the diffraction-limited spot size. Moreover, NanoPen requires the use of a photoconductive thin-film substrate for the patterning process to work. However, after patterning the structures in the desired locations, the photoconductive film can potentially be removed [187] to allow further processing steps. Here, we have focused on patterning one kind of a particle at a time. However, this limitation can be overcome through integration of NanoPen with microfluidic channels to form a complete optofluidic [188] system. Such integration would help realize promising applications such as the creation of DNA microarrys. However, future investigations need to be done to study the operational conditions of NanoPen for patterning biomaterials such as DNA and various proteins. Furthermore, since the immobilization force is dominated by the dielectrophoresis force, it can potentially be tuned according to particle size and material properties. In addition, the well-understood surface chemistry [189] of gold nanocrystals makes them ideal carriers of other materials such as DNA, therefore, NanoPen patterning of gold nanoparticles can be used to pattern other materials conjugated to the gold surface. In its present form NanoPen introduces a flexible, real-time reconfigurable, large-scale, and low-power method for patterning various nanostructures with potential applications in chemical and biological sensing, opto- and nano-electronic device fabrication, nanostructure synthesis, and photovoltaics.

Chapter 7 Conclusion

Optoelectronic tweezers (OET) presents a powerful optofluidic platform for light-actuated manipulation of micro and nanoscale particles. Various operational regimes and electrokinetic forces have been observed and characterized in the OET device including: light-induced dielectrophoresis, light-actuated AC electroosmosis, and electrothermal flow. Through combining the benefits of optical and electrical actuation, OET is capable of manipulating particles with approximately 5 orders of magnitude less optical intensity than optical tweezers. Moreover, since the electrodes are optically defined, OET is capable of dynamic and real-time manipulation of particles in contrast to fixed electrode dielectrophoresis techniques.

Manipulation of various nanostructures has been investigated using the OET platform including: semiconducting and metallic nanowires, multi-wall and single-wall carbon nanotubes, and metallic spherical nanoparticles. According to the dielectrophoresis (DEP) theory, the magnitude of the DEP force is proportional to the volume of the particle, therefore, the DEP force decreases rapidly as the size of the particle reduces, making manipulation of nano-scale particles difficult. However, the anisotropic geometry of particles such as nanowires and nanotubes greatly enhances the polarizability of the objects and increases the DEP force, making their manipulation possible. In the case of metallic spherical nanoparticles, the increase in polarizability is not present, however, the particles are immersed in the high electric field intensity region close to the OET bottom surface and experience larger field intensity gradients which enhances the DEP force magnitude and leads to trapping of these particles near the OET surface.

The OET's ability to manipulate nanoparticles opens up many exciting possibilities in post-synthesis organization and heterogeneous integration of nanostructures. These new capabilities are enabled by dynamic and massively parallel nature of OET platform and include: real-time density tuning of nanoparticles, parallel assembly of nanowires and nanotubes for optoelectronic applications, in-situ and dynamic sensing of molecules for chemical and biological applications, and dynamic separation of nanostructures according to their polarizability (conductivity). In addition to trapping individual nanostructures, a novel patterning technique, called NanoPen, based on OET was demonstrated which is capable of large-scale patterning of various

nanostructures using a commercial projector (<10 W/cm^2) within seconds. NanoPen is capable of large-scale formation of surface-enhanced Raman spectroscopy "hot-spots" by patterning gold nanoparticles with enhancement factors exceeding 10^7 and pico-molar sensitivities.

In conclusion, optoelectronic tweezers presents a powerful platform for organization of nanostructures and enables many new capabilities essential in transforming nano-sciences into successful nano-technologies.

Appendix 1 OET Fabrication Process

In this section, we will review the fabrication process for optoelectronic tweezers devices. All processes have been completed at UC Berkeley microfabrication laboratory (Microlab). Figure A1.1 shows the steps involved in fabrication of the OET device. The process starts with 6-inch, 720 μm thick glass wafers coated with 300 nm layer of sputtered indium tin oxide (ITO), with 10 Ω/□ sheet resistance. The wafers were first cleaned in a pre-furnace metal clean bath followed by rinse and N_2 dry steps. Plasma enhanced chemical vapor deposition (PECVD) was used to deposit 1-2 μm of hydrogenated amorphous silicon. The process conditions for PECVD deposition of a-Si:H are: 400 sccm Ar, 100 sccm SiH_4, at 900mTorr pressure, 350°C temperature, and 100W RF bias.

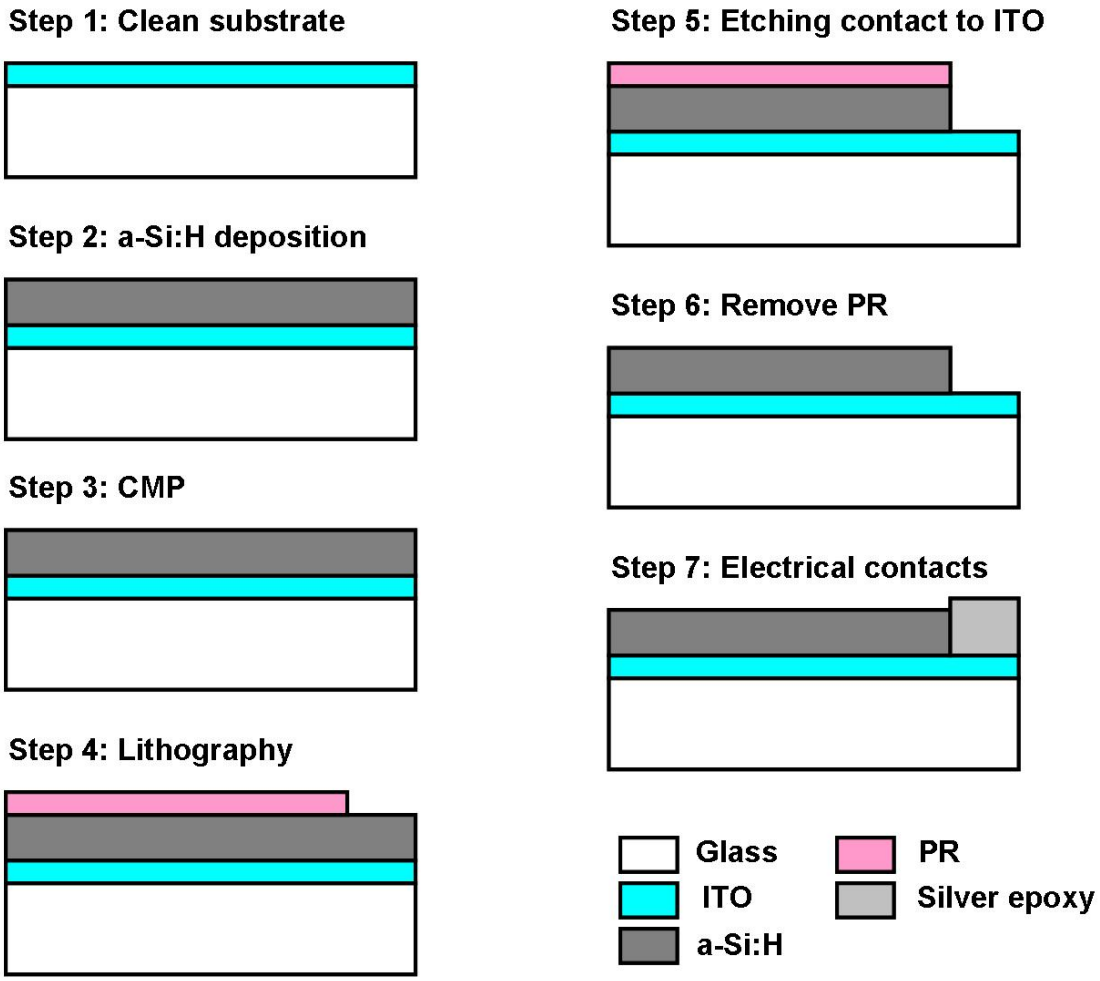

Figure A.1 Optoelectronic tweezers fabrication process.

After the a-Si:H deposition is completed, the surface of the wafers are polished to reduce the a-Si:H surface roughness. This step is critical to improve the dark-field observation quality. As shown in figure A.2a, the surface of the as-deposited a-Si:H strongly scatters light due to surface roughness which makes the observation of nanoparticles challenging under dark-field. The chemical mechanical polishing (CMP) of the a-Si:H layer results in a smoother surface with considerably reduced scattering under dark field observation (Figure A.2b).

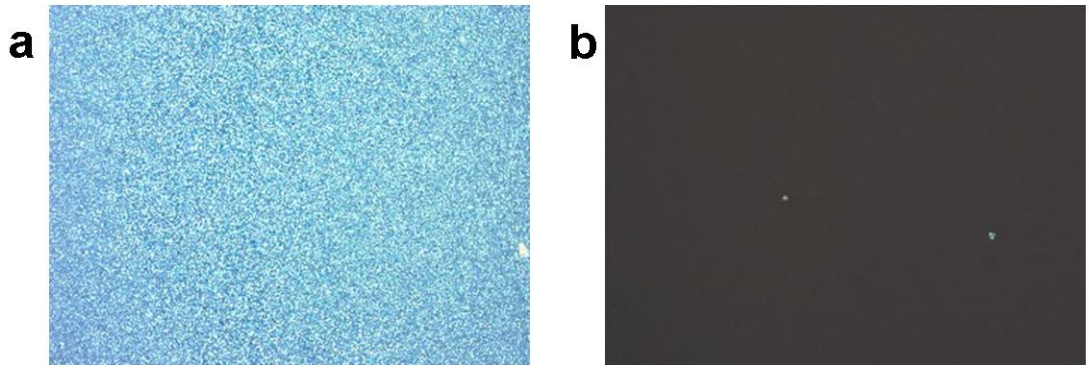

Figure A.2 Dark-field image of the OET surface (a) before the CMP step and (b) after the CMP step.

After the CMP step is completed, the glass wafers are diced to make OET chips with typical sizes of 2 cm×3 cm. The chips are coated with photoresist (PR) and lithography is used to remove the PR in the electrical contact area. RIE etching is used to remove a-Si:H to ITO layer and finally silver epoxy is applied to make contact to the ITO layer.

The top side of the OET device consists of ITO-coated glass slides which is fabricated by dicing the original 720 μm thick ITO-coated glass slides to make 2cm×3cm size chips. The gap spacing between the top and the bottom layer is typically defined using double sided tape with 80-100 μm thickness.

BIBLIOGRAPHY

[1] Y. Xia, P. Yang, Y. Sun, Y. Wu, B. Mayers, B. Gates, Y. Yin, F. Kim, and H. Yan, "One-dimensional nanostructures: Synthesis, characterization, and applications," *Advanced Materials (Weinheim, Germany),* vol. 15, pp. 353-389, 2003.

[2] A. P. Alivisatos, "Semiconductor Clusters, Nanocrystals, and Quantum Dots," *Science* vol. 271, pp. 933 - 937, 1996.

[3] H. Dai, "Carbon Nanotubes: Synthesis, Integration, and Properties," *Acc. Chem. Res.,* vol. 35, pp. 1035-1044, 2002.

[4] M. C. Daniel and D. Astruc, "Gold Nanoparticles: Assembly, Supramolecular Chemistry, Quantum-Size-Related Properties, and Applications toward Biology, Catalysis, and Nanotechnology," *Chem. Rev.,* vol. 104, pp. 293-346, 2004.

[5] M. S. Dresselhaus, G. Dresselhaus, and P. Avouris, *Carbon nanotubes: synthesis, structure, properties, and applications*: Springer, 2001.

[6] P. J. Pauzauskie and P. Yang, "Nanowire photonics," *Materials Today,* vol. 9, pp. 36-45, Oct 2006.

[7] A. Bachtold, P. Hadley, T. Nakanishi, and C. Dekker, "Logic Circuits with Carbon Nanotube Transistors," *Science,* vol. 294, pp. 1317-1320, 2001.

[8] A. Javey, J. Guo, Q. Wang, M. Lundstrom, and H. J. Dai, "Ballistic carbon nanotube field-effect transistors," *Nature,* vol. 424, pp. 654-657, Aug 2003.

[9] J. N. Anker, W. P. Hall, O. Lyandres, N. C. Shah, J. Zhao, and R. P. Van Duyne, "Biosensing with plasmonic nanosensors," *Nature Materials,* vol. 7, 2008.

[10] K. Kneipp, Y. Wang, H. Kneipp, L. T. Perelman, I. Itzkan, R. R. Dasari, and M. S. Feld, "Single molecule detection using surface-enhanced Raman scattering (SERS)," *Phys. Rev. Lett.,* vol. 78, pp. 1667 - 1670, 1997.

[11] S. Nie and S. R. Emory, "Probing single molecules and single nanoparticles by surface-enhanced Raman scattering," *Science,* vol. 275, pp. 1102 - 1106, 1997.

[12] A. I. Hochbaum, R. Chen, R. Diaz Delgado, W. Liang, E. C. Garnett, M. Najarian, A. Majumdar, and P. Yang, "Enhanced thermoelectric performance of rough silicon nanowires," *Nature,* vol. 451, pp. 163-167, 2008.

[13] M. Law, D. J. Sirbuly, J. C. Johnson, J. Goldberger, R. J. Saykally, and P. D. Yang, "Nanoribbon waveguides for subwavelength photonics integration," *Science,* vol. 305, pp. 1269-1273, Aug 27 2004.

[14] P. J. Pauzauskie, T. Kuykendall, Y. F. Zhang, J. Goldberger, D. Sirbuly, J. Denlinger, and P. D. Yang, "Crystallographic alignment of high-density gallium nitride nanowire arrays," *Nature Materials,* vol. 3, pp. 524-528, Aug 2004.

[15] R. He and P. Yang, "Giant piezoresistance effect in silicon nanowires," *Nat Nano,* vol. 1, p. 42, 2006.

[16] T. Martensson, C. P. T. Svensson, B. A. Wacaser, M. W. Larsson, W. Seifert, K. Deppert, A. Gustafsson, L. R. Wallenberg, and L. Samuelson, "Epitaxial III-V nanowires on silicon," *Nano Letters,* vol. 4, pp. 1987-1990, Oct 2004.

[17] D. G. Grier, "A revolution in optical manipulation," *Nature,* vol. 424, pp. 810-816, Aug 2003.

[18] A. Ashkin, "Acceleration and Trapping of Particles by Radiation Pressure " *Physical Review Letters,* vol. 24, p. 156, 1970.

[19] A. Ashkin, M. Dziedzic, and T. Yamane, "Optical trapping and manipulation of single cells using infrared-laser beams," *Nature,* vol. 330, pp. 769-771, 1987.

[20] P. J. Pauzauskie, A. Radenovic, E. Trepagnier, H. Shroff, P. D. Yang, and J. Liphardt, "Optical trapping and integration of semiconductor nanowire assemblies in water," *Nature Materials,* vol. 5, pp. 97-101, Feb 2006.

[21] J. Plewa, E. Tanner, D. M. Mueth, and D. G. Grier, "Processing carbon nanotubes with holographic optical tweezers," *Optics Express,* vol. 12, pp. 1978-1981, May 2004.

[22] K. Svoboda and S. M. Block, "Optical trapping of metallic Rayleigh particles," *Optics Letters,* vol. 19, pp. 930-932, 1994.

[23] P. C. Ke and M. Gu, "Characterization of trapping force on metallic Mie particles " *Applied Optics,* vol. 38, pp. 160-167, 1999.

[24] T. M. Nishizaka, H., H. Yoshikawa, S. Ishiwata, and K. Kinosita Jr, "Unbinding force of a single motor molecule of muscle measured using optical tweezers," *Nature,* vol. 377, pp. 251-254, 1995.

[25] R. Agarwal, K. Ladavac, Y. Roichman, G. H. Yu, C. M. Lieber, and D. G. Grier, "Manipulation and assembly of nanowires with holographic optical traps," *Optics Express,* vol. 13, pp. 8906-8912, Oct 31 2005.

[26] R. Krupke, F. Hennrich, H. von Lohneysen, and M. M. Kappes, "Separation of metallic from semiconducting single-walled carbon nanotubes," *Science,* vol. 301, pp. 344-347, Jul 18 2003.

[27] S. Y. Lee, T. H. Kim, D. I. Suh, J. E. Park, J. H. Kim, C. J. Youn, B. K. Ahn, and S. K. Lee, "An electrical characterization of a hetero-junction nanowire (NW) PN diode (n-

GaN NW/p-Si) formed by dielectrophoresis alignment," *Physica E-Low-Dimensional Systems & Nanostructures,* vol. 36, pp. 194-198, Feb 2007.

[28] P. A. Smith, C. D. Nordquist, T. N. Jackson, T. S. Mayer, B. R. Martin, J. Mbindyo, and T. E. Mallouk, "Electric-field assisted assembly and alignment of metallic nanowires," *Applied Physics Letters,* vol. 77, pp. 1399-1401, Aug 28 2000.

[29] S. J. Papadakis, Z. Gu, and D. H. Gracias, "Dielectrophoretic assembly of reversible and irreversible metal nanowire networks and vertically aligned arrays," *Applied Physics Letters,* vol. 88, 2006.

[30] C. R. Cabrera and P. Yager, "Continuous concentration of bacteria in a microfluidic flow cell using electrokinetic techniques," *Electrophoresis,* vol. 22, pp. 355-362, 2001.

[31] C. R. Barry, J. Gu, and H. O. Jacobs, "Charging Process and Coulomb-Force-Directed Printing of Nanoparticles with Sub-100-nm Lateral Resolution," *Nano Lett.,* vol. 5, pp. 2078-2084, 2005.

[32] N. G. Loucaides, A. Ramos, and G. E. Georghiou, "Trapping and manipulation of nanoparticles by using jointly Dielectrophoresis and AC electroosmosis," *Journal of Physics: Conference Series* vol. 100, 2008.

[33] P. Avouris, T. Hertel, R. Martel, T. Schmidt, H. R. Shea, and R. E. Walkup, "Carbon nanotubes: nanomechanics, manipulation, and electronic devices," *Applied Surface Science,* vol. 141, pp. 201-209, 1999.

[34] C. Thelander and L. Samuelson, "AFM manipulation of carbon nanotubes: realization of ultra-fine nanoelectrodes," *Nanotechnology,* vol. 13, pp. 108-113, 2002.

[35] H. Lee, A. M. Purdon, V. Chu, and R. M. Westervelt, "Controlled Assembly of Magnetic Nanoparticles from Magnetotactic Bacteria Using Microelectromagnets Arrays," *Nano Lett.,* vol. 4, pp. 995-998, 2004.

[36] M. Tanase, L. A. Bauer, A. Hultgren, D. M. Silevitch, L. Sun, D. H. Reich, P. C. Searson, and G. J. Meyer, "Magnetic Alignment of Fluorescent Nanowires," *Nano Lett.,* vol. 1, pp. 155-158, 2001.

[37] A. K. Bentley, J. S. Trethewey, A. B. Ellis, and W. C. Crone, "Magnetic manipulation of copper-tin nanowires capped with nickel ends," *Nano Lett.,* vol. 4, pp. 487-490, 2004.

[38] J. X. Huang, F. Kim, A. R. Tao, S. Connor, and P. D. Yang, "Spontaneous formation of nanoparticle stripe patterns through dewetting," *Nature Materials,* vol. 4, pp. 896-900, Dec 2005.

[39] B. Messer, J. H. Song, and P. D. Yang, "Microchannel networks for nanowire patterning," *Journal Of The American Chemical Society,* vol. 122, pp. 10232-10233, Oct 18 2000.

[40] S. G. Rao, L. Huang, W. Setyawan, and S. Hong, "Large-scale assembly of carbon nanotubes," *Nature,* vol. 425, pp. 36-37, 2003.

[41] J. H. Ahn, H. S. Kim, K. J. Lee, S. Jeon, S. J. Kang, Y. Sun, R. G. Nuzzo, and J. A. Rogers, "Heterogeneous Three-Dimensional Electronics by Use of Printed Semiconductor Nanomaterials " *Science,* vol. 314, pp. 1754 - 1757, 2006.

[42] Z. Fan, J. C. Ho, Z. A. Jacobson, R. Roie Yerushalmi, R. L. Alley, H. Razavi, and A. Ali Javey, "Wafer-Scale Assembly of Highly Ordered Semiconductor Nanowire Arrays by Contact Printing," *Nano Lett.,* vol. 8, pp. 20-25, 2008.

[43] H. X. He, Q. G. Li, Z. Y. Zhou, H. Zhang, W. Huang, S. F. Y. Li, and Z. F. Liu, "Fabrication of Microelectrode Arrays Using Microcontact Printing," *Langmuir* vol. 16, p. 9683, 2000.

[44] Y. Xia and G. M. Whitesides, "Soft lithography," *Annu. Rev. Mater. Sci.,* vol. 28, p. 153, 1998.

[45] J. H. Ahn, H. S. Kim, K. J. Lee, S. Jeon, S. J. Kang, Y. G. Sun, R. G. Nuzzo, and J. A. Rogers, "Heterogeneous three-dimensional electronics by use of printed semiconductor nanomaterials," *Science,* vol. 314, pp. 1754-1757, Dec 15 2006.

[46] P. Yang, "Nanotechnology: Wires on water," *Nature (London, United Kingdom),* vol. 425, pp. 243-244, 2003.

[47] A. Tao, F. Kim, C. Hess, J. Goldberger, R. He, Y. Sun, Y. Xia, and P. Yang, "Langmuir-Blodgett silver nanowire monolayers for molecular sensing using surface-enhanced Raman spectroscopy," *Nano Letters,* vol. 3, pp. 1229-1233, 2003.

[48] S. Jin, D. M. Whang, M. C. McAlpine, R. S. Friedman, Y. Wu, and C. M. Lieber, "Scalable interconnection and integration of nanowire devices without registration," *Nano Letters,* vol. 4, pp. 915-919, May 2004.

[49] R. D. Piner, J. Zhu, F. Xu, S. Hong, and C. A. Mirkin, ""Dip-pen" Nanolithography," *Science,* vol. 283, 1999.

[50] K. Salaita, Y. Wang, and C. A. Mirkin, "Applications of dip-pen nanolithography," *Nat. Nanotechnol.,* vol. 145, pp. 145-155, 2007.

[51] B. Basnar and I. Willner, "Dip-Pen-Nanolithographic Patterning of Metallic, Semiconductor, and Metal Oxide Nanostructures on Surfaces," *Small,* vol. 5, p. 28, 2009.

[52] D. S. Ginger, H. Zhang, and C. A. Mirkin, "The Evolution of Dip-Pen Nanolithography," *Angew. Chem. Int. Ed. Engl. ,* vol. 43, p. 30, 2004.

[53] B. Li, C. F. Goh, X. Zhou, G. Lu, H. Tantang, Y. Chen, C. Xue, F. Y. C. Boey, and H. Zhang, "Patterning colloidal metal nanoparticles for controlled growth of carbon nanotubes," *Adv. Mater. ,* vol. 20, pp. 4873-4878, 2008.

[54] H. T. Wang, O. A. Nafday, J. R. Haaheim, E. Tevaarwerk, N. A. Amro, R. G. Sanedrin, C. Y. Chang, F. Ren, and S. J. Pearton, "Toward conductive traces: Dip Pen Nanolithography of silver nanoparticle-based inks," *Appl. Phys. Lett. ,* vol. 93, p. 143105, 2008.

[55] J. C. Hulteen, D. A. Treichel, M. T. Smith, M. L. Duval, T. R. Jensen, and R. P. V. Duyne, "Nanosphere Lithography: Size-Tunable Silver Nanoparticle and Surface Cluster Arrays," *J. Phys. Chem. B,* vol. 103, pp. 3854-3863, 1999.

[56] A. Javey and H. Dai, "Regular Arrays of 2 nm Metal Nanoparticles for Deterministic Synthesis of Nanomaterials," *J. Am. Chem. Soc.,* vol. 127, pp. 11942-11943, 2005.

[57] P. Y. Chiou, A. T. Ohta, and M. C. Wu, "Massively parallel manipulation of single cells and microparticles using optical images," *Nature,* vol. 436, pp. 370-372, Jul 21 2005.

[58] A. Jamshidi, P. J. Pauzauskie, P. J. Schuck, A. T. Ohta, P. Y. Chiou, J. Chou, P. Yang, and M. C. Wu, "Dynamic manipulation and separation of individual semiconducting and metallic nanowires," *Nature Photonics,* vol. 2, pp. 85-89, Feb 2008.

[59] H. Y. Hsu, A. T. Ohta, P. Y. Chiou, A. Jamshidi, S. L. Neale, and M. C. Wu, "Phototransistor-based optoelectronic tweezers for dynamic cell manipulation in cell culture media," *Lab Chip,* vol. DOI 10.1039/b906593h, 2009.

[60] Y. Higuchi, T. Kusakabe, T. Tanemura, K. Sugano, T. Tsuchiya, and O. Tabata, "Manipulation system for nano/micro components integration via transportation and self-assembly," in *Conference on Micro Electro Mechanical Systems*, 2008.

[61] X. Miao and L. Y. Lin, "Trapping and manipulation of biological particles through a plasmonic platform," *IEEE Journal of Selected Topics in Quantum Electronics: Special Issue on Biophotonics,* vol. 13, pp. 1655-1662, 2007.

[62] X. Miao, B. K. Wilson, S. H. Pun, and L. Y. Lin, "Optical manipulation of micron/submicron sized particles and biomolecules through plasmonics," *Optics Express,* vol. 16, p. 13517, 2008.

[63] W. Wang, Y. H. Lin, T. F. Guo, and G. B. Lee, "Manipulation of Biosamples and Microparicles using Optical Images on Polymer Devices," in *IEEE 22nd International Conference on Micro Electro Mechanical Systems*, 2009.

[64] P. Y. Chiou, W. Wong, J. C. Liao, and M. C. Wu, "Cell addressing and trapping using novel optoelectronic tweezers," *IEEE International Conference on Micro Electro Mechanical Systems, Technical Digest, 17th, Maastricht, Netherlands, Jan. 25-29, 2004,* pp. 21-24, 2004.

[65] W. Choi, S. H. Kim, J. Jang, and J. K. Park, "Lab-on-a-display: a new microparticle manipulation platform using a liquid crystal display (LCD)," *Microfluidics and Nanofluidics,* vol. 3, pp. 217-225, 2007.

[66] H. Hwang, Y. J. Choi, W. Choi, S. H. Kim, J. Jang, and J. K. Park, "Interactive manipulation of blood cells using a lens-integrated liquid crystal display based optoelectronic tweezers system,," *Electrophoresis,* vol. 29, pp. 1203-1212, 2008.

[67] P. Y. Chiou, A. T. Ohta, A. Jamshidi, H. Y. Hsu, and M. C. Wu, "Light-Actuated AC Electroosmosis for Nanoparticle Manipulation," *Journal of Microelectromechanical Systems,* vol. 17, 2008.

[68] J. K. Valley, A. Jamshidi, A. T. Ohta, H. Y. Hsu, and M. C. Wu, "Operational Regimes and Physics Present in Optoelectronic Tweezers," *Journal of Microelectromechanical Systems,* vol. 17, 2008.

[69] S. L. Neale, M. Mazilu, J. I. B. Wilson, K. Dholakia, and T. F. Krauss, "The resolution of optical traps created by Light Induced Dielectrophoresis (LIDEP)," *Optics Express,* vol. 15, pp. 12619-12626 2007.

[70] A. T. Ohta, P. Y. Chiou, T. H. Han, J. C. Liao, U. Bhardwaj, E. R. B. McCabe, F. Q. Yu, R. Sun, and M. C. Wu, "Dynamic cell and microparticle control via optoelectronic tweezers," *Journal of Microelectromechanical Systems,* vol. 16, pp. 491-499, Jun 2007.

[71] A. T. Ohta, P. Y. Chiou, H. L. Phan, S. W. Sherwood, J. M. Yang, A. N. K. Lau, H. Y. Hsu, A. Jamshidi, and M. C. Wu, "Optically-controlled cell discrimination and trapping using optoelectronic tweezers," *IEEE J. Sel. Top. Quant.,* vol. 243, pp. 235-243, 2007.

[72] Y.-S. Lu, Y.-P. Huang, J. A. Yeh, C. Lee, and Y.-H. Chang, "Controllability of non-contact cell manipulation by image dielectrophoresis (iDEP)," *Optical and Quantum Electronics,* vol. 37, pp. 1385-95, 2005.

[73] H. Y. Hsu, A. T. Ohta, P. Y. Chiou, A. Jamshidi, and M. C. Wu, "Phototransistor-Based Optoelectronic Tweezers for Cell Manipulation in Highly Conductive Solution," in *Solid-State Sensors, Actuators and Microsystems Conference*, 2007.

[74] H. Y. Hsu, H. Lee, S. Pautot, K. Yu, S. Neale, A. T. Ohta, A. Jamshidi, J. Valley, E. Isocaff, and M. C. Wu, "Sorting of differentiated neurons using phototransistor based optoelectronic tweezers for cell replacement therapy of neurodegenerative diseases," in *The 15th International Conference on Solid-State Sensors, Actuators and Microsystems* Denver, Colorado, 2009.

[75] S. L. Neale, Z. Fan, A. T. Ohta, A. Jamshidi, J. K. Valley, H. Y. Hsu, A. Javey, and M. C. Wu, "Optofluidic Assembly of Red/Blue/Green Semiconductor Nanowires," in *Conference on Lasers and Electro-Optics* 2009.

[76] A. T. Ohta, A. Jamshidi, P. J. Pauzauskie, H. Y. Hsu, P. Yang, and M. C. Wu, "Trapping and transport of silicon nanowires using lateral-field optoelectronic tweezers," in *Conference on Lasers and Electro-Optics (CLEO)*, Baltimore, MD, 2007, pp. 828-829.

[77] A. T. Ohta, S. L. Neale, H. Y. Hsu, J. K. Valley, and M. C. Wu, "Parallel assembly of nanowires using lateral-field optoelectronic tweezers," in *2008 IEEE/LEOS International Conference on Optical MEMS and Nanopotonics*, 2008.

[78] P. J. Pauzauskie, A. Jamshidi, J. K. Valley, J. Satcher, J. H., and M. C. Wu, "Parallel trapping of multiwalled carbon nanotubes with optoelectronic tweezers," *Applied Physics Letters,* vol. 95, pp. 113104-1, 2009.

[79] A. Jamshidi, H. Y. Hsu, J. K. Valley, A. T. Ohta, S. Neale, and M. C. Wu, "Metallic Nanoparticle Manipulation using Optoelectronic Tweezers," in *IEEE 22nd International Conference on Micro Electro Mechanical Systems*, 2009.

[80] M. Hoeb, J. O. Radler, S. Klein, M. Stutzmann, and M. S. Brandt, "Light-induced dielectrophoretic manipulation of DNA," *Biophysical Journal,* vol. 93, pp. 1032-1038, 2007.

[81] Y.-H. Lin, C.-M. Chang, and G.-B. Lee, "Manipulation of single DNA molecules by using optically projected images," *Opt. Express,* vol. 17, pp. 15318-15329, 2009.

[82] J. K. Valley, S. Neale, H. Y. Hsu, A. T. Ohta, A. Jamshidi, and M. C. Wu, "Parallel single-cell light-induced electroporation and dielectrophoretic manipulation," *Lab Chip,* vol. 9, pp. 1714 - 1720, 2009.

[83] Y.-H. Lin and G. B. Lee, "An optically induced cell lysis device using dielectrophoresis," *Appl. Phys. Lett. ,* vol. 94, p. 033901, 2009.

[84] Y.-H. Lin and G.-B. Lee, "Optically induced flow cytometry for continuous microparticle counting and sorting," *Biosensors and Bioelectronics,* vol. 24, pp. 572–578, 2008.

[85] A. Jamshidi, S. L. Neale, K. Yu, P. J. Pauzauskie, P. J. Schuck, J. K. Valley, H. Y. Hsu, A. T. Ohta, and M. C. Wu, "NanoPen: Dynamic, Low-Power, and Light-Actuated Patterning of Nanoparticles," *Nano Lett.,* vol. 9, pp. 2921–2925, 2009.

[86] S. Park, C. Pan, T.-H. Wu, C. Kloss, S. Kalim, C. E. Callahan, M. Teitell, and E. P. Y. Chiou, "Floating electrode optoelectronic tweezers: light-driven dielectrophoretic droplet manipulation in electrically insulating oil medium," *Applied Physics Letters,* vol. 92, pp. 151101-1-3, 2008.

[87] H. Hwang, Y. Oh, J. J. Kim, W. Choi, J. K. Park, S. H. Kim, and J. Jang, "Reduction of nonspecific surface-particle interactions in optoelectronic tweezers," *Applied Physics Letters,* vol. 92, p. 3, 2008.

[88] G. J. Shah, A. T. Ohta, P. Y. Chiou, M. C. Wu, and C.-J. Kim, "EWOD-driven droplet microfluidic device integrated with optoelectronic tweezers as an automated platform for cellular isolation and analysis," *Lab Chip,* vol. 9, pp. 1732-1739, 2009.

[89] J. K. Valley, A. Jamshidi, A. T. Ohat, H.-Y. Hsu, and M. C. Wu, "Operational Regiems and Physics Present in Optoelectronic Tweezers," *Journal of Microelectromechanical Systems,* vol. DOI 10.1109, 2008.

[90] N. B. Colthup, L. H. Daly, and S. E. Wiberley, *Introduction to infrared and Raman spectroscopy* Academic Press 1975.

[91] E. Ewen Smith and G. Dent, *Modern Raman Spectroscopy: A Practical Approach* Wiley, 2005.

[92] R. L. McCreery, *Raman Spectroscopy for Chemical Analysis* Wiley-Interscience, 2000.

[93] S. Adachi, *Optical properties of crystalline and amorphous semiconductors: materials and fundamental principles*: Boston: Kluwer Academic Publishers, 1999.

[94] R. Schwarz, F. Wang, and M. Reissner, "Fermi level dependence of the ambipolar diffusion length in silicon thin film transistors," *Applied Physics Letters,* vol. 63, pp. 1083-5, 1993.

[95] G. R. Fowles, *Introduction to Modern Optics*: Dover, 1989.

[96] T. B. Jones, *Electromechanics of Particles*: Cambridge University Press, 1995.

[97] H. Morgan and N. Green, *AC Electrokinetics: colloids and nanoparticles* Research Studies Press Ltd., 2003.

[98] J. Lyklema, *Fundamentals of Interface and Colloid Science* vol. 2. London: Academic Press, 1991.

[99] P. Wang, Z. L. Chen, and H. C. Chang, "A new electro-osmotic pump based on silica monoliths," *Sensors and Actuators B-Chemical,* vol. 113, pp. 500-509, Jan 2006.

[100] H. Daiguji, P. D. Yang, and A. Majumdar, "Ion transport in nanofluidic channels," *Nano Letters,* vol. 4, pp. 137-142, 2004.

[101] R. B. M. Schasfoort, S. Schlautmann, L. Hendrikse, and A. van den Berg, "Field effect flow control for microfabricated fluidic networks," *Science,* vol. 286, pp. 942-945, 1999.

[102] J. P. Urbanski, T. Thorsen, J. A. Levitan, and M. Z. Bazant, "Fast AC electroosmotic micropumps with nonplanar electrodes," *Applied Physics Letters,* vol. 89, p. 3, 2006.

[103] P. Y. Chiou, A. T. Ohta, A. Jamshidi, H.-Y. Hsu, J. B. Chou, and M. C. Wu, "Light-Actuated AC Electroosmosis for Optical Manipulation of Nanoscale Particles," in *Proceedings fo Solid-State Sensor, Actuator, and Microsystems Workshop*, Hilton Head, 2006, pp. 56-59.

[104] P. Y. Chiou, "Massively Parallel Optical Manipulation of single Cells, Micro- and Nano-particles on Optoelectronic Devices." vol. PhD: University of California Berkeley, 2005.

[105] A. Castellanos, A. Ramos, A. Gonzalez, N. G. Green, and H. Morgan, "Electrohydrodynamics and dielectrophoresis in microsystems: scaling laws," *Journal of Physics D-Applied Physics,* vol. 36, pp. 2584-2597, Oct 2003.

[106] A. Ramos, H. Morgan, N. G. Green, and A. Castellanos, "AC Electrokinetics: a review of forces in microelectrode structures," *Journal of Physics D-Applied Physics,* vol. 31, pp. 2338-2353, Sep 1998.

[107] A. Einstein, *Investigations on the Theory of Brownian Movement*. New York: Dover, 1956.

[108] A. I. Hochbaum, R. Fan, R. He, and P. Yang, "Controlled growth of Si nanowire arrays for device integration," *Nano Letters,* vol. 5, pp. 457-460, 2005.

[109] K. Q. Peng, Y. J. Yan, S. P. Gao, and J. Zhu, "Synthesis of large-area silicon nanowire arrays via self-assembling nanoelectrochemistry," *Advanced Materials,* vol. 14, pp. 1164-1167, Aug 16 2002.

[110] Y. G. Sun, B. Gates, B. Mayers, and Y. N. Xia, "Crystalline silver nanowires by soft solution processing," *Nano Letters,* vol. 2, pp. 165-168, Feb 2002.

[111] J. C. Crocker and D. G. Grier, "Methods of digital video microscopy for colloidal studies," *Journal of Colloid and Interface Science,* vol. 179, pp. 298-310, Apr 1996.

[112] C. Decker, "Kinetic Study and New Applications of UV Radiation Curing," *Macromol. Rapid Commun.,* vol. 23, pp. 1067-1093, 2002.

[113] D. J. Beebe, J. S. Moore, J. M. Bauer, Q. Yu, R. H. Liu, C. Devadoss, and B. H. Jo, "Functional hydrogel structures for autonomous flow control inside microuidic channels," *Nature,* vol. 404, pp. 588-590, 2000.

[114] M. Law, L. Greene, J. C. Johnson, R. Saykally, and P. Yang, "Nanowire dye-sensitized solar cells," *Nature Materials,* vol. 4, pp. 455-459, 2005.

[115] M. S. Dresselhaus, G. Chen, M. Y. Tang, R. Yang, H. Lee, D. Wang, Z. Ren, J. P. Fleurial, and P. Gogna, "New Directions for Low-Dimensional Thermoelectric Materials," *Advanced Materials,* pp. 1043-1053, 2007.

[116] J. Goldberger, A. I. Hochbaum, R. Fan, and P. Yang, "Silicon Vertically Integrated Nanowire Field Effect Transistors " *Nano Letters,* vol. 6, pp. 973-977, 2006.

[117] S. R. Nicewarner-Pena, R. G. Freeman, B. D. Reiss, L. He, D. J. Pena, I. D. I. D. Walton, R. Cromer, C. D. Keating, and M. J. Natan, "Submicrometer Metallic Barcodes " *Science,* vol. 294, p. 137, 2001.

[118] J. B.-H. Tok, F. Y. S. Chuang, M. C. Kao, K. A. Rose, S. S. Pannu, M. Y. Sha, G. Chakarova, S. G. Penn, and G. M. Dougherty, "Metallic Striped Nanowires as

Multiplexed Immunoassay Platforms for Pathogen Detection," *Angew. Chem. Int. Ed.,* vol. 45, p. 6900, 2006.

[119] A. Tao, F. Kim, C. Hess, J. Goldberger, R. He, Y. Sun, Y. Xia, and P. Yang, "Langmuir−Blodgett Silver Nanowire Monolayers for Molecular Sensing Using Surface-Enhanced Raman Spectroscopy," *Nano Lett.,* vol. 3, p. 1229, 2003.

[120] A. V. Akimov, A. Mukherjee, C. L. Yu, D. E. Chang, A. S. Zibrov, P. R. Hemmer, H. Park, and M. D. Lukin, "Generation of single optical plasmons in metallic nanowires coupled to quantum dots," *Nature,* vol. 450, pp. 402-406, 2007.

[121] H. Ditlbacher, A. Hohenau, D. Wagner, U. Kreibig, M. Rogers, F. Hofer, F. R. Aussenegg, and J. R. Krenn, "Silver Nanowires as Surface Plasmon Resonators," *Phys. Rev. Lett.,* vol. 95, pp. 257403-1, 2005.

[122] X. Hu and C. T. Chan, "Photonic crystals with silver nanowires as a near-infrared superlens," *Applied Physics Letters,* vol. 85, p. 1520, 2004.

[123] L. A. Bauer, N. S. Birenbaum, and G. J. Meyer, "Biological applications of high aspect ratio nanoparticles," *J. Mater. Chem.,* vol. 14, pp. 517-526, 2004.

[124] M. Z. Bazant and T. M. Squires, "Induced-charge electrokinetic phenomena: theory and microfluidic applications," *Phys. Rev. Lett.,* vol. 02, p. 066101, 2004.

[125] N. I. Gamayunov, G. I. Mantrov, and V. A. Murtsovkin, "Study of flows induced in the vicinity of conducting particles by an extenal electric field," *J. Colloid Interface Sci.,* vol. 54, p. 20, 1992.

[126] J. A. Levitan, S. Devasenathipathy, V. Studer, Y. Ben, T. Thorsen, T. M. Squires, and M. Z. Bazant, "Experimental observation of induced-charge electro-osmosis around a metal wire in a microchannel " *Colloids Surf., A,* vol. 267, p. 122, 2005.

[127] K. A. Rose, B. Hoffman, D. Saintillan, E. S. G. Shaqfeh, and J. G. Santiago, "Hydrodynamic interactions in metal rodlike-particle suspensions due to induced charge electroosmosis," *Physical Review E,* vol. 79, 2009.

[128] T. M. Squires and M. Z. Bazant, "Induced-charge electro-osmosis," *J. Fluid Mech.,* vol. 509, p. 217, 2004.

[129] L. Dong, J. Bush, V. Chirayos, R. Solanki, J. Jiao, Y. Ono, J. Conley, J. F., and B. D. Ulrich, "Dielectrophoretically Controlled Fabrication of Single-Crystal Nickel Silicide Nanowire Interconnects " *Nano Letters,* vol. 5, pp. 2112-2115, 2005.

[130] D. L. Fan, F. Q. Zhu, R. C. Cammarata, and C. L. Chien, "Manipulation of nanowires in suspension by ac electric fields," *Applied Physics Letters* vol. 85, pp. 4175-4177, 2004.

[131] R. Kretschmer and W. Fritzsche, "Pearl chain formation of nanoparticles in microelectrode gaps by dielectrophoresis," *Langmuir,* vol. 20, pp. 11797-11801, 2004.

[132] R. Pething, Y. Huang, X. Wang, and J. P. H. Burt, "Positive and negative dielectrophoretic collection of colloidal particles using interdigitated castellated microelectrodes," *J. Phys. D: Appl. Phys.,* vol. 24, pp. 881-888, 1992.

[133] A. Jamshidi, P. J. Pauzauskie, P. J. Schuck, A. T. Ohta, P. Y. Chiou, J. Chou, P. Yang, and M. C. Wu, "Dynamic Manipulation and Separation of Semiconducting and Metallic Nanowires " *Nature Photonics,* vol. 2, pp. 85-89, 2008.

[134] R. Yerushalmi, J. C. Ho, Z. A. Jacobson, and A. Javey, "Generic Nanomaterial Positioning by Carrier and Stationary Phase Design," *Nano Letters,* vol. 7, pp. 2764-2768, 2007.

[135] B. J. Hinds, N. Chopra, T. Rantell, R. Andrews, V. Gavalas, and L. G. Bachas, "Aligned multiwalled carbon nanotube membranes," *Science,* vol. 303, pp. 62-65, Jan 2004.

[136] C. Y. Lee, R. Sharma, A. D. Radadia, R. I. Masel, and M. S. Strano, "On-chip micro gas chromatograph enabled by a noncovalently functionalized single-walled carbon nanotube sensor array," *Angewandte Chemie-International Edition,* vol. 47, pp. 5018-5021, 2008.

[137] L. Ci, J. Suhr, V. Pushparaj, X. Zhang, and P. M. Ajayan, "Continuous carbon nanotube reinforced composites," *Nano Letters,* vol. 8, pp. 2762-2766, Sep 2008.

[138] S. T. Purcell, P. Vincent, C. Journet, and V. T. Binh, "Hot nanotubes: Stable heating of individual multiwall carbon nanotubes to 2000 K induced by the field-emission current," *Physical Review Letters,* vol. 88, Mar 2002.

[139] B. Q. Wei, R. Vajtai, and P. M. Ajayan, "Reliability and current carrying capacity of carbon nanotubes," *Applied Physics Letters,* vol. 79, pp. 1172-1174, Aug 2001.

[140] N. Halonen, K. Kordas, G. Toth, T. Mustonen, J. Maklin, J. Vahakangas, P. M. Ajayan, and R. Vajtai, "Controlled CCVD synthesis of robust multiwalled carbon nanotube films," *Journal of Physical Chemistry C,* vol. 112, pp. 6723-6728, May 2008.

[141] M. F. Islam, E. Rojas, D. M. Bergey, A. T. Johnson, and A. G. Yodh, "High Weight Fraction Surfactant Solubilization of Single-Wall Carbon Nanotubes in Water," *3,* pp. 269-273, 2003.

[142] K. Balasubramanian and M. Burghard, "Chemically functionalized carbon nanotubes," *Small,* vol. 1, pp. 180-192, Feb 2005.

[143] R. Duggal and M. Pasquali, "Dynamics of individual single-walled carbon nanotubes in water by real-time visualization," *Physical Review Letters,* vol. 96, Jun 2006.

[144] D. A. Tsyboulski, S. M. Bachilo, A. B. Kolomeisky, and R. B. Weisman, "Translational and rotational dynamics of individual single-walled carbon nanotubes in aqueous suspension," *ACS Nano,* vol. 2, pp. 1770-1776, Sep 2008.

[145] Z. H. Yu and L. Brus, "Rayleigh and Raman scattering from individual carbon nanotube bundles," *Journal of Physical Chemistry B,* vol. 105, pp. 1123-1134, Feb 2001.

[146] S. Broersma, "Viscous Force and Torque Constants for a Cylinder," *Journal of Chemical Physics,* vol. 74, pp. 6989-6990, 1981.

[147] M. C. LeMieux, M. Roberts, S. Barman, Y. W. Jin, J. M. Kim, and Z. N. Bao, "Self-sorted, aligned nanotube networks for thin-film transistors," *Science,* vol. 321, pp. 101-104, Jul 2008.

[148] K. Kordas, T. Mustonen, G. Toth, H. Jantunen, M. Lajunen, C. Soldano, S. Talapatra, S. Kar, R. Vajtai, and P. M. Ajayan, "Inkjet printing of electrically conductive patterns of carbon nanotubes," *Small,* vol. 2, pp. 1021-1025, Aug 2006.

[149] Q. Cao, H. S. Kim, N. Pimparkar, J. P. Kulkarni, C. J. Wang, M. Shim, K. Roy, M. A. Alam, and J. A. Rogers, "Medium-scale carbon nanotube thin-film integrated circuits on flexible plastic substrates," *Nature,* vol. 454, pp. 495-U4, Jul 2008.

[150] S. D. Tan, H. A. Lopez, C. W. Cai, and Y. G. Zhang, "Optical trapping of single-walled carbon nanotubes," *Nano Letters,* vol. 4, pp. 1415-1419, Aug 2004.

[151] O. M. Marago, P. H. Jones, F. Bonaccorso, V. Scardaci, P. G. Gucciardi, A. G. Rozhin, and A. C. Ferrari, "Femtonewton Force Sensing with Optically Trapped Nanotubes," *Nano Letters,* vol. 8, pp. 3211-3216, Oct 2008.

[152] T. Rodgers, S. Shoji, Z. Sekkat, and S. Kawata, "Selective aggregation of single-walled carbon nanotubes using the large optical field gradient of a focused laser beam," *Physical Review Letters,* vol. 101, p. 127402, Sep 2008.

[153] R. D. Saito, G; Dresselhaus, M.S.;, *Physical Properties of Carbon Nanotubes*. London: Imperial College Press, 1998.

[154] L. J. Carlson and T. D. Krauss, "Photophysics of individual single-walled carbon nanotubes," *Accounts of Chemical Research,* vol. 41, pp. 235-243, 2008.

[155] J. Appenzeller, "Carbon nanotubes for high-performance electronics - Progress and prospect," *Proceedings of the IEEE,* vol. 96, pp. 201-211, 2008.

[156] M. S. Arnold, A. A. Green, J. F. Hulvat, S. I. Stupp, and M. C. Hersam, "Sorting carbon nanotubes by electronic structure using density differentiation," *Nature Nanotechnology,* vol. 1, pp. 60-65, Oct 2006.

[157] L. Zhang, S. Zaric, X. M. Tu, X. R. Wang, W. Zhao, and H. J. Dai, "Assessment of chemically separated carbon nanotubes for nanoelectronics," *Journal of the American Chemical Society,* vol. 130, pp. 2686-2691, Feb 2008.

[158] K. Svoboda and S. M. Block, "Optical trapping of metallic Rayleigh particles," *Optics Letters* vol. 19, 1994.

[159] P. M. Hansen, V. K. Bhatia, N. Harrit, and L. Oddershede, "Expanding the Optical Trapping Range of Gold Nanoparticles," *Nano Letters,* vol. 5, pp. 1937-1942, 2005.

[160] Y. Seol, A. E. Carpenter, and T. T. Perkins, "Gold nanoparticles: enhanced optical trapping and sensitivity coupled with significant heating," *Optics Letters,* vol. 31, 2006

[161] L. Zheng, S. Li, J. P. Brody, and P. J. Burke, "Manipulating Nanoparticles in Solution with Electrically Contacted Nanotubes Using Dielectrophoresis," *Langmuir,* vol. 20, pp. 8612-8619, 2004.

[162] A. Ramos, H. Morgan, N. G. Green, and A. Castellanos, "AC electrokinetics: A review of forces in microelectrode structures," *J. Phys. D. Appl. Phys.,* vol. 31, pp. 2338–2353, 1998.

[163] W. Yang, J. Hulteen, G. C. Schatz, and R. P. V. Duyne, "A surface-enhanced hyper-Raman and surface-enhanced Raman scattering study of trans-1,2-bis(4-pyridyl)ethylene adsorbed onto silver film over nanosphere electrodes. Vibrational assignments: Experiment and theory," *J. Chem. Phys.,* vol. 104, pp. 4313-4323, 1996.

[164] N. J. Durr, T. Larson, D. K. Smith, B. A. Korgel, K. Sokolov, and A. Ben-Yakar, "Two-Photon Luminescence Imaging of Cancer Cells Using Molecularly Targeted Gold Nanorods," *Nano Lett.,* vol. 7, pp. 941-945, 2007.

[165] H. Wang, T. B. Huff, D. A. Zweifel, W. He, P. S. Low, A. Wei, and J.-X. Cheng, "In vitro and in vivo two-photon luminescence imaging of single gold nanorods " *PNAS,* vol. 102, pp. 15752-6, 2005.

[166] N. Shen, D. Datta, C. B. Schaffer, P. LeDuc, D. E. Ingber, and E. Mazur, "Ablation of cytoskeletal filaments and mitochondria in live cells using a femtosecond laser nanoscissor," *MCB,* vol. 2, pp. 17-25, 2005.

[167] A. Vogel, J. Noack, G. Hüttman, and G. Paltauf, "Mechanisms of femtosecond laser nanosurgery of cells and tissues " *Applied Physics B: Lasers and Optics,* vol. 81, pp. 1015-1047.

[168] S. A. Johnson and T. Hunter, "Kinomics: Methods for Deciphering the Kinome " *Nature Methods,* vol. 2, pp. 17-25, 2005.

[169] P. O. Brown and D. Botstein, "Exploring the new world of the genome with DNA microarrays," *Nat. Genet.,* vol. 21, pp. 33-37, 1999.

[170] M. Schena, D. Shalon, R. W. Davis, and P. O. Brown, "Quantitative Monitoring of Gene Expression Patterns with a Complementary DNA Microarray," *Science,* vol. 270, pp. 467 - 470, 1995.

[171] J. N. Anker, W. P. Hall, O. Lyandres, N. C. Shah, J. Zhao, and R. P. Van Duyne, "Biosensing with plasmonic nanosensors," *Nat. Mater.,* vol. 7, pp. 442 - 453, 2008.

[172] M. H. Huang, S. Mao, H. Feick, H. Yan, Y. Wu, H. Kind, E. Weber, R. Russo, and P. Yang, "Room-Temperature Ultraviolet Nanowire Nanolasers " *Science,* vol. 292, pp. 1897 - 1899, 2001.

[173] A. Javey, J. Guo, Q. Wang, M. Lundstrom, and H. Dai, "Ballistic carbon nanotube field-effect transistors," *Nature,* vol. 424, pp. 654-657, 2003.

[174] P. D. Yang, "The Chemistry and Physics of Semiconductor Nanowires," *MRS Bull.,* vol. 30, pp. 85-91, 2005.

[175] B. Sun, A. T. Findikoglu, M. Sykora, D. J. Werder, and V. I. Klimov, "Hybrid Photovoltaics Based on Semiconductor Nanocrystals and Amorphous Silicon," *Nano Lett.,* 2009.

[176] R. Yerushalmi, J. C. Ho, Z. A. Jacobson, and A. Javey, "Generic Nanomaterial Positioning by Carrier and Stationary Phase Design," *Nano Lett.,* vol. 7, pp. 2764-2768, 2007.

[177] E. Rabani, D. R. Reichman, P. L. Geissler, and L. E. Brus, "Drying-mediated self-assembly of nanoparticles," *Nature,* vol. 426, pp. 271-274, 2003.

[178] C. P. Collier, R. J. Saykally, J. J. Shiang, S. E. Henrichs, and J. R. Heath, "Reversible Tuning of Silver Quantum Dot Monolayers Through the Metal-Insulator Transition," *Science,* vol. 277, pp. 1978-1981, September 26, 1997 1997.

[179] R. C. Hayward, D. A. Saville, and I. A. Aksay, "Electrophoretic assembly of colloidal crystals with optically tunable micropatterns," *Nature,* vol. 404, pp. 56-59, 2000.

[180] S. J. Williams, A. Kumar, and S. T. Wereley, "Electrokinetic patterning of colloidal particles with optical landscapes," *Lab Chip,* vol. 8, pp. 1879-1882, 2008.

[181] P. J. Pauzauskie, A. Radenovic, E. Trepagnier, H. Shroff, P. D. Yang, and J. Liphardt, "Optical trapping and integration of semiconductor nanowire assemblies in water," *Nat. Mater.,* vol. 5, pp. 97-101, Feb 2006.

[182] S. Ito, H. Yoshikawa, and H. Masuharaa, "Optical patterning and photochemical fixation of polymer nanoparticles on glass substrates," *Appl. Phys. Lett.,* vol. 78, pp. 2566-2568, 2001.

[183] B. K. Wilson, M. Hegg, X. Miao, G. Cao, and L. Y. Lin, "Scalable nano-particle assembly by efficient light-induced concentration and fusion," *Opt. Express,* vol. 16, pp. 17276-17281, 2008.

[184] A. Ramos, H. Morgan, N. G. Green, and A. Castellanos, "AC electricfield-induced fluid flow in microelectrodes," *J. Colloid Interf. Sci.,* vol. 217, pp. 420-422, 1999.

[185] A. Castellanos, A. Ramos, A. Gonzalez, N. G. Green, and H. Morgan, "Electrohydrodynamics and dielectrophoresis in microsystems: Scaling laws," *J. Phys. D. Appl. Phys.,* vol. 36, pp. 2584–2597, 2003.

[186] Nanopartz, "Nanopartz Accurate Spherical Gold Nanoparticles," 2008.

[187] M. C. Tien, A. T. Ohta, K. Yu, S. L. Neale, and M. C. Wu, "Heterogeneous integration of InGaAsP microdisk laser on a silicon platform using optofluidic assembly," *Appl. Phys. A,* vol. 95, p. 967, 2009.

[188] D. Psaltis, S. R. Quake, and C. Yang, "Developing optofluidic technology through the fusion of microfluidics and optics," *Nature,* vol. 442, pp. 381-386, 2006.

[189] M. C. Daniel and D. Astruc, "Gold Nanoparticles: Assembly, Supramolecular Chemistry, Quantum-Size-Related Properties, and Applications toward Biology, Catalysis, and Nanotechnology," *Chem. Rev.,* vol. 104, pp. 293-346, 2004.